The Dissertation Committee for Charles Joseph Abolt certifies that this is the approved version of the following dissertation:

Trajectories of land surface evolution in polygonal tundra

Committee:

Michael H. Young, Supervisor

Todd G. Caldwell

Meinhard Bayani Cardenas

Daniella M. Rempe

Marc A. Hesse

Trajectories of land surface evolution in polygonal tundra

by

Charles Joseph Abolt

Dissertation

Presented to the Faculty of the Graduate School of

The University of Texas at Austin

in Partial Fulfillment

of the Requirements

for the Degree of

Doctor of Philosophy

The University of Texas at Austin

May 2019

Dedication

To my partner and truest friend, Randolph Wilhelm.

Acknowledgements

I am indebted to my advisor, Michael Young. When I first met Michael, I had a Spanish degree and a job at the grocery store. Luckily, he was willing to take a risk by hiring me as a temporary employee, then advising me as a student. In the past seven years, the opportunities he has created for me have been quite literally life changing (even though that's normally just a phrase). I am sincerely thankful for the time and energy he has invested in me and the course he has put me on professionally.

Likewise, I am grateful to Adam Atchley, who mentored me over the last two summers at Los Alamos National Laboratory. His consistently positive attitude made struggles with convergence errors fun, and his insights into numerical modeling and manuscript writing have been extremely valuable as I've put together this dissertation. I'm grateful as well to Dylan Harp and Ethan Coon for guidance working with Amanzi-ATS, and Cathy Wilson for creating the opportunity for me to intern at the lab.

I wish to thank each member of my dissertation committee for genuinely engaging me in this research and for having the patience to read this dissertation, especially Todd Caldwell—who took a dunk with me in the lake at Toolik and invited me on a bunch of cool field campaigns in Texas—and Bayani Cardenas—whose classes on physical hydrology and field methods gave me a solid foundation to start this research. I am grateful as well to too many other people I've met in grad school to list here, but especially Kristine Uhlman, for introducing me to numerical modeling, and Philip Guerrero, for introducing me to Enchiladas y Más.

I acknowledge the financial support to complete this research, which included a NASA Earth and Space Science Fellowship, scholarships and travel grants from the Jackson School of Geosciences, and the Next Generation Ecosystem Experiments-Arctic project funded by Office of Biological and Environmental Research in the Department of Energy Office of Science.

Finally, thank you to my family for love and support throughout my life and education, especially to my late mother, my father, and Randolph. I sure am lucky to have you on my team.

Abstract

Trajectories of land surface evolution in polygonal tundra

Charles Joseph Abolt, Ph.D.
The University of Texas at Austin, 2019

Supervisor: Michael H. Young

In the past three decades, an abrupt acceleration in the thaw of ice wedges has spurred rapid surface deformation (*i.e.*, thermokarst) in polygonal tundra landscapes spanning the Arctic. The ensuing conversion of low-centered polygons (LCPs) and flat terrain into high-centered polygons (HCPs) has profound impacts on regional hydrology and carbon fluxes between the soil and atmosphere. However, pathways of ice wedge degradation and the stability of the deformed terrain are uncertain, complicating efforts to project feedbacks on global climate change. In this dissertation, I explore trajectories of surface deformation in ice wedge polygons, using a combination of calibration-constrained numerical experiments, remote sensing, and machine learning. In the first two chapters, numerical simulations of the soil hydrologic and thermal regimes reveal that, relative to terrain unaffected by thermokarst, the permafrost beneath HCPs tends to be well-buffered against climate extremes, promoting landscape stability. Ice wedges at HCP boundaries are less vulnerable to thaw during warm summers, reinforcing prior field-based observations that thermokarst is typically a self-arresting process. Simultaneously, the cooling of thermokarst-affected ice wedges in winter tends to be inhibited by snow accumulation in degraded troughs, reducing the likelihood of renewed ice wedge cracking and restoration of LCP microtopography. Overall, these results indicate that the microtopography of polygons already affected by thermokarst will likely remain stable over the next century. In the second half of this dissertation, a novel machine-learning-based tool is introduced for delineating and measuring the microtopography associated with ice wedge polygons in high-resolution digital elevation models. The tool is used to map polygonal geomorphology across ~1,000 km^2 of tundra south of Prudhoe Bay, Alaska, visualizing in unprecedented detail the heterogeneous extent to which thermokarst has affected a modern polygonal landscape. This map of polygonal geomorphology provides useful context for upscaling point- to plot-scale observations of gas exchange in ice wedge polygons to landscape-scale estimates of carbon fluxes. It also provides an extensive baseline dataset for quantifying contemporary rates of land surface deformation, through future surveys at the site.

Table of Contents

Chapter 1: Introduction

The motivation behind this dissertation is to better understand the geomorphic evolution of ice wedge polygons in tundra landscapes. Segmenting the ground like the desiccation polygons of a drying clay-rich soil, but measuring some tens of meters across, ice wedge polygons are some of the most conspicuous landforms of the continuous permafrost zone. In low-gradient settings such as the coastal plain of the Arctic Ocean, microtopographic features of ice wedge polygons—such as rims of soil several decimeters in height at the edges of low-centered polygons (LCPs), or troughs up to a meter deep demarcating the boundaries of high-centered polygons (HCPs)—often represent the most prominent relief amid otherwise flat terrain (Leffingwell, 1919). This microtopography exerts strong controls on hydrologic processes such as evaporation and runoff generation (Liljedahl et al., 2012; 2016), which in turn influence soil ecology and carbon exchange between the subsurface and the atmosphere (Zona et al., 2011; Olivas et al., 2011; Wainwright et al., 2015; Lara et al., 2015). Arctic soils presently store more carbon than the global atmosphere (Schuur et al., 2008; Tarnocai et al., 2009); therefore, quantitative understanding of the relationships between microtopography, hydrology, and soil ecology is important for predicting changes to the global carbon cycle over the next century (Schuur et al., 2015). Conceptualizing these relationships at large spatial and temporal scales is challenging, however, as microtopographic relief tends to vary over spatial scales of meters and evolve dynamically in response to a warming environment (Jorgenson et al., 2006; 2015).

Fundamentally, the geomorphology of ice wedge polygons is linked to climate, as polygonal terrain originates due to thermal contraction cracking at the land surface in winter, when ground temperatures drop below a threshold near -13° C (Mackay, 1984; Morse and Burn, 2013; Lachenbruch, 1962). The fissures opened by this process may approach several centimeters in width, and extend to depths of 4-5 m. During the first year in which a surface, such as a newly drained lake bed, experiences cracking, a vein of ice tends to develop within each fissure, either through direct deposition of hoarfrost, or the freezing of infiltrating meltwater in spring. Because the tensile strength of ice is less than that of frozen soil, the same cracks tend to open cyclically; over timescales of centuries, repeated deposition of ice veins produces a vertically-laminated wedge of ice, up to several meters across at the upper face (Figure 1.1). In many cases, stresses associated with the slow growth of ice wedges drive upward warping in the adjacent sediments, creating ramparts at the edges of basin-like LCPs (Mackay, 2000). In other instances, a polygonal network of ice wedges may exist at the top of the permafrost with no reflection in surface topography (Mackay, 1990; 1995; Liljedahl et al., 2016).

Whether LCP relief is present or not, any terrain underlain by ice wedges is vulnerable to rapid surface deformation when thaw penetrates the upper faces of the ice wedges. During the last three decades in particular, studies throughout the Arctic have documented an abrupt acceleration in the development of mound-like HCPs, which has been attributed to climate change (Jorgenson et al., 2006; Raynolds et al., 2014; Liljedahl et al., 2016). This process begins when thaw eliminates the upper several decimeters of the ice wedges, driving preferential subsidence of the overlying soil, which accentuates a network of troughs at the polygon boundaries (Figure 1.2). These changes often destabilize the soil in the rims of an LCP, which erodes outward into the troughs, producing the characteristic form of an HCP (Abolt et al., 2017). Simultaneously, impoundment of water in the degraded troughs often results in the formation of shallow ponds, which may accelerate ice wedge degradation by increasing shortwave energy absorption (Jorgenson et al., 2015). This transformation of the land surface, frequently referred to as *thermokarst*, is generally thought to terminate as the accumulation of organic material at the bottom of troughs—sourced either from the growth of aquatic vegetation, or colluvium from eroding rims—re-stabilizes the ice wedges by providing insulation from warmer air temperatures (Jorgenson et al., 2006; 2015; Kanevskiy et al., 2017). Nonetheless, decade- to century-scale trajectories of landscape evolution on the tundra are uncertain, as the progression of thermokarst is influenced by a complex set of feedbacks between topography, surface water, and ground temperatures, which determine the thermal stability of the permafrost (Raynolds et al., 2014; Kanevskiy et al., 2017).

Reducing this uncertainty is important for a variety of applications, which include constraining the impact of thermokarst on carbon cycling. Recent work indicate that changes to carbon fluxes associated microtopogaphic deformation may be sufficient to exert feedback on global climate processes (Schuur et al., 2015). This influence arises from the dynamics of myriad biophysical processes, which vary in activity over spatial scales of meters. HCP formation, for example, tends to improve the drainage of soils in the polygon center, which stimulates aerobic respiration of soil organic carbon, accelerating emissions of CO_2 (Lara et al., 2015; Wainwright et al., 2015). Simultaneously, microbial activity in flooded troughs, or *thermokarst pools*, may increase CH_4 emissions more than an order of magnitude, relative to drained soil (Martin et al., 2018). Understanding of factors such as the relative stability of HCP microtopography and the expansion of thermokarst pools is consequently an important aspect of predicting the role of tundra soils as a global source or sink of carbon over the next century.

In this dissertation, pathways of land surface evolution in polygonal terrain are explored through a combination of numerical modeling experiments, machine learning, and remote sensing. The guiding questions are:

1. How does microtopographic deformation during thermokarst exert feedbacks on the ground thermal regime?
2. How stable is land surface after thermokarst?
3. What will the land surface look like decades to centuries from now?

In Chapter 2, a numerical model of the hydrologic and thermal regime is applied in tundra soils to explore how microtopographic deformation influences ground temperatures in winter, thereby determining the potential for ice wedge cracking and restoration of polygonal rims adjacent to thermokarst-affected troughs. In Chapter 3, the same model is used to explore hydrologic and topographic feedbacks on ice wedge degradation, comparing the vulnerability of ice wedges beneath LCPs, HCPs, and flat terrain. In Chapter 4, a novel machine-learning based tool is introduced for outlining and measuring the microtopographic attributes of ice wedge polygons in high-resolution digital elevation models. Finally, in Chapter 5, the tool is applied across ~1,000 km^2 of terrain captured through an airborne lidar survey, measuring the microtopography associated with ~10^6 ice wedge polygons. The resulting landcover map offers a sharp visualization of the spatially heterogeneous influence of thermokarst on a modern tundra landscape and provides a baseline dataset for quantifying contemporary landscape evolution through future surveys.

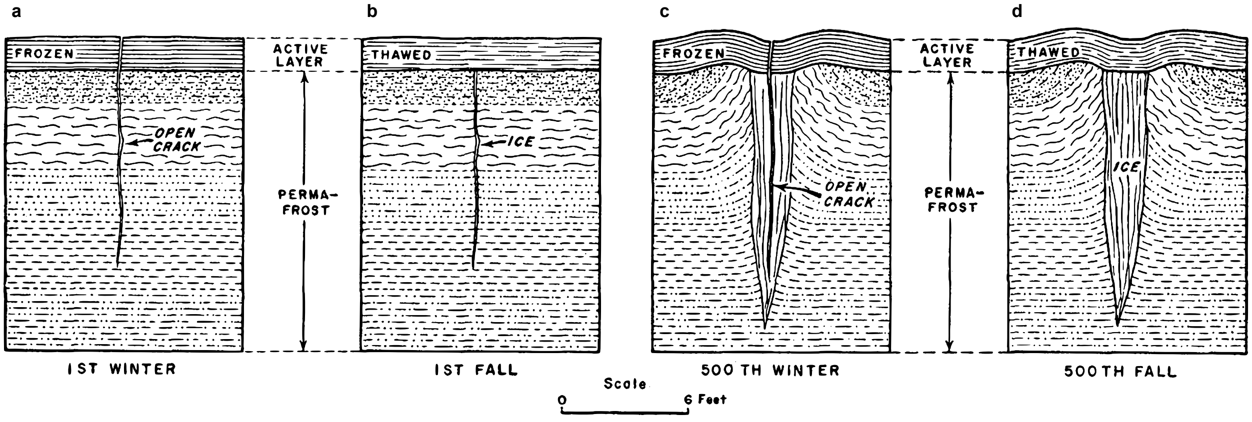

Figure 1.1

Schematic of ice wedge formation by thermal contraction cracking and ice deposition, from Lachenbruch (1962) with permission of publisher. Ice wedge formation is feasible when near-surface cracks that open to relieve thermal contraction stresses in winter extend into the permafrost (**a**), causing infiltrating snow melt in spring to be preserved as a semi-permanent vein of ice (**b**). Because ice possesses a weaker tensile strength than frozen soil, the same cracks tend to reopen cyclically (**c**). Incremental ice deposition at each cracking event drives subsurface expansion of the wedge, which warps the adjacent sediments, creating the rims of low-centered polygons (**d**).

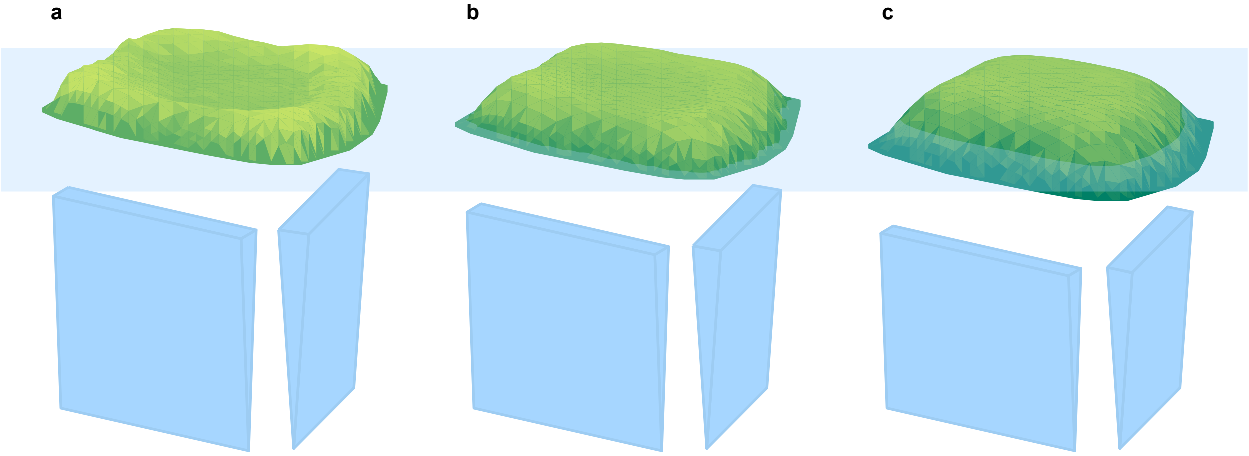

Figure 1.2

Schematic of surface deformation in an initially low-centered polygon during thermokarst. Deformation begins in the LCP (**a**) as ablation at the tops of the ice wedges causes the boundaries of the polygon to subside downward (toward the water table), spurring outward-oriented soil erosion which reduces relief in the rims (**b**). As the boundaries continue to subside, rims are eliminated and troughs may become occupied by perennial standing water, or thermokarst pools (**c**).

REFERENCES

Abolt CJ, Young MH, Caldwell TG. 2017. Numerical modelling of ice-wedge polygon geomorphic transition. *Permafrost and Periglacial Processes* **28**: 347-355.

Jorgenson MT, Shur Y, Pullman ER. 2006. Abrupt increase in permafrost degradation in Arctic Alaska. *Geophysical Research Letters* **25**: L02503.

Jorgenson MT, Kanevskiy M, Shur Y, et al. 2015. Role of ground ice dynamics and ecological feedbacks in recent ice wedge degradation and stabilization. *Journal of Geophysical Research: Earth Surface* **120**, 2280-2297.

Kanevskiy M, Shur Y, Jorgenson MT, et al. 2017. Degradation and stabilization of ice wedges: Implication for assessing risk of thermokarst in northern Alaska. *Geomorphology* **297**: 20-42.

Lachenbruch AH. 1962. Mechanics of thermal contraction cracks and ice-wedge polygons in permafrost. Geological Society of America Special Paper 70.

Lara MJ, McGuire DA, Euskirchen ES, et al. 2015. Polygonal tundra geomorphological change in response to warming alters future CO_2 and CH_4 flux on the Barrow Peninsula. *Global Change Biology* **21**: 1634-1651.

Leffingwell EK. 1915. Ground-ice wedges, the dominant form of ground-ice on the north coast of Alaska. *Journal of Geology* **23**: 635-654.

Liljedahl AK, Hinzman LD, Schulla J. 2012. Ice-wedge polygon type controls low-gradient watershed-scale hydrology. *Tenth International Congerence on Permafrost*: Salekhard, Russia. June 25-29.

Liljedahl AK, Boike J, Daanen RP, et al. 2016. Pan-Arctic ice wedge degradation in warming permafrost and its influence on tundra hydrology. *Nature Geoscience* **9**, 312-318.

Mackay JR. 1984. The direction of ice-wedge cracking in permafrost: Downward or upward? *Canadian Journal of Earth Sciences* **21**: 516-524.

Mackay JR. 1990. Some observations on the growth and deformation of epigenetic, syngenetic, and anti-syngenetic ice wedges. *Permafrost and Periglacial Processes* **1**: 15-29.

Mackay JR. 1995. Ice wedges on hillslopes and landform evolution in the late Quaternary, western Arctic coast, Canada. *Canadian Journal of Earth Science* **32**: 1093-1105.

Mackay JR. 2000. Thermally induced movements in ice-wedge polygons, western Arctic coast: A long-term study. *Géographie Physique et Quarternaire* **54**: 41-68.

Martin AF, Lantz TC, Humphreys ER. 2018. Ice wedge degradation and CO_2 and CH_4 emissions in the Tuktoyaktuk Coastlands, Northwest Territories. *Arctic Science* **4**, 130-145.

Morse PD, Burn CR. 2013. Field observations of syngenetic ice wedge polygons, outer Mackenzie Delta, western Arctic coast, Canada. *Journal of Geophysical Research: Earth Surface* **118**: 1320-1332.

Olivas PC, Oberbauer SF, Tweedie C, Oechel WC, Lin D, Kuchy A. 2011. Effects of fine-scale topography on CO_2 flux components of Alaskan coastal plain tundra: Response to contrasting growing seasons. *Arctic Antarctic and Alpine Research* **43**: 256-266.

Raynolds MK, Walker DA, et al. 2014. Cumulative geoecological effects of 62 years of infrastructure and climate change in ice-rich permafrost landscapes, Prudhoe Bay Oilfield, Canada. *Global Change Biology* **20**: 1211-1224.

Schuur EAG, Vogel JG, et al. 2009. The effect of permafrost thaw on old carbon release and net carbon exchange from tundra. *Nature* **459**: 556-559.

Schuur EAG, McGuire AD, et al. 2015. Climate change and the permafrost carbon feedback. *Nature* **520**: 171-179.

Tarnocai C, Canadell JG, et al. Soil organic carbon pools in the northern circumpolar permafrost region. *Global Biogeochemical Cycles* **23**: GB2023.

Wainwright HM, Dafflon B, Smith LJ, et al. 2015. Identifying multiscale zonation and assessing the relative importance of polygon geomorphology on carbon fluxes in an Arctic tundra ecosystem. *Journal of Geophysical Research: Biogeosciences* **120**, 788-808.

Zona D, Lipson DA, Zulueta RC, Oberbauer SF, Oechel WC. 2011. Microtopographic controls on ecosystem functioning in the Arctic Coastal Plain. *Journal of Geophysical Research* **116**: G001241.

Chapter 2: Microtopographic control on the ground thermal regime in ice wedge polygons[1]

Abstract

The goal of this research is to constrain the influence of ice wedge polygon microtopography on near-surface ground temperatures. Ice wedge polygon microtopography is prone to rapid deformation in a changing climate, and cracking in the ice wedge depends on thermal conditions at the top of the permafrost; therefore, feedbacks between microtopography and ground temperature can shed light on the potential for future ice wedge cracking in the Arctic. We first report on a year of sub-daily ground temperature observations at 5 depths and 9 locations throughout a cluster of low-centered polygons near Prudhoe Bay, Alaska, and demonstrate that the rims become the coldest zone of the polygon during winter, due to thinner snowpack. We then calibrate a polygon-scale numerical model of coupled thermal and hydrologic processes against this dataset, achieving an RMSE of less than 1.1°C between observed and simulated ground temperature. Finally, we conduct a sensitivity analysis of the model by systematically manipulating the height of the rims and the depth of the troughs and tracking the effects on ice wedge temperature. The results indicate that winter temperatures in the ice wedge are sensitive to both rim height and trough depth, but more sensitive to rim height. Rims act as preferential outlets of subsurface heat; increasing rim size decreases winter temperatures

---

[1] published as: Abolt CJ, Young MH, Atchley AL, Harp DR. 2018. Microtopographic control on the ground thermal regime in ice wedge polygons. *The Cryosphere* 12: 1957-1968. CJA conceived the study, conducted the simulations, and wrote the manuscript.

in the ice wedge. Deeper troughs lead to increased snow entrapment, promoting insulation of the ice wedge. The potential for ice wedge cracking is therefore reduced if rims are destroyed or if troughs subside, due to warmer conditions in the ice wedge. These findings can help explain the origins of secondary ice wedges in modern and ancient polygons. The findings also imply that the potential for re-establishing rims in modern thermokarst-affected terrain will be limited by reduced cracking activity in the ice wedges, even if regional air temperatures stabilize.

2.1 Introduction

It has long been understood that the formation of ice wedge polygons is intimately linked with thermal contraction ground stresses (Leffingwell, 1915; Lachenbruch, 1962; Mackay, 2000). However, changes to the near surface thermal regime as polygon microtopography develops are poorly constrained. Across the continuous permafrost zone, winter ground temperatures below -10°C commonly drive the opening of a network of cracks, ~4-5 m deep, that bound polygonal regions of soil, 10-30 m in diameter. Over timescales of centuries to millennia, repeated cracking and infilling with ice in the same locations produces wedge-shaped bodies of ice at the top of the permafrost, up to 5 m wide (Kanevskiy et al., 2013). Particularly in coastal regions of the Arctic, the slow growth of ice wedges results in subtle but distinctive surface topography, as pressure between the wedge and the adjacent ground creates rims of raised soil at the perimeters of the polygons. Although only on the scale of decimeters, this microtopography profoundly influences tundra hydrology (Liljedahl et al., 2012; 2016), and may exert equally strong controls on microbial conversion of soil organic carbon into carbon dioxide and methane (Zona et al., 2011; Wainwright et al., 2015). Polygon microtopography also controls depth variation in the winter snowpack, which accumulates preferentially in low zones, such as the trough space between polygons (Mackay, 1993; Mackay, 2000; Morse and Burn, 2014; Wainwright et al., 2017). It is well known that snow accumulation in periglacial terrain strongly controls winter ground temperatures, by providing insulation from the atmosphere (e.g., Mackay and MacKay, 1974; Goodrich, 1982). Moreover, it has been widely observed that changes to polygon microtopography have accelerated in the past three decades, as rising air temperatures have increasingly driven the subsidence of troughs and the destruction of rims (Jorgenson et al., 2006; Raynolds et al., 2014; Liljedahl et al., 2016). However, feedbacks between microtopographic change and the thermal regime of the ice wedge, which control the likelihood of sustained ice wedge cracking in the future, are incompletely understood.

In this paper, we quantify the relationship between the microtopography of ice wedge polygons and subsurface temperatures, using a combination of field observations and numerical modeling. We first analyze a high-resolution record of ground temperature in key locations beneath a low-centered polygon near Prudhoe Bay, Alaska, and use the observational data to calibrate a numerical model of coupled thermal and hydrologic processes at the polygon scale. We then conduct a sensitivity analysis to determine the influence of two topographic attributes, rim height and trough depth, on winter temperatures in the ice wedges. To our knowledge, our analysis is the first to quantitatively estimate influences on ground temperature associated with these two variables, which are difficult to control in field experiments and prone to rapid variation as polygons develop and respond to a changing climate (Jorgenson et al., 2006; Raynolds et al., 2014; Liljedahl et al., 2016). The results shed light on feedbacks that will determine the sustainability of ice wedge cracking in the near future, as warming air temperatures drive rapid surface deformation in polygonal terrain. The results are also relevant to understanding of processes associated with historical development of ice wedge polygons, including the formation of "secondary" ice wedges, or comparatively young wedges that subdivide older polygons, observed in modern and ancient systems (Burn and O'Neill, 2015).

2.2 Background

A substantial amount of research has explored interactions between ground temperatures and ice wedge cracking. The earliest, and still most rigorous, mechanical analysis was conducted by Lachenbruch (1962, 1966), who concluded that the probability of a cracking event is determined by two criteria: whether the ground temperature cools below a variable threshold near -10°C, and whether the rate of cooling is sufficient. These conditions are most crucial at the top of the permafrost, where most ice wedge cracks originate (Mackay, 1984). Recently, a number of investigations have used electronic temperature sensors to more tightly constrain thermal conditions at the time of cracking at field sites across the Arctic (e.g., Mackay, 1993; Allard and Kasper, 1998; Christiansen, 2005; Fortier and Allard, 2005; Kokelj et al., 2007, O'Neill and Christiansen, 2018). Although heterogeneity exists between sites, it has been generalized that ice wedge cracking is most favorable when ground temperature at the top of the permafrost drops below -13°C, and the rate of cooling exceeds 0.1°C d^{-1} for two days or more (Morse and Burn, 2013; Kokelj et al., 2014).

In contrast to research on ice wedge cracking, relatively few investigations have explored systematic variation in ground temperatures associated with polygon microtopography. In particular, few datasets have been published that monitor ground temperature beneath distinct zones of a polygon in the same season. Nonetheless, one consistently observed trend is that the rims of a low-centered polygon tend to become several degrees colder in winter than the center or troughs (Mackay, 1993; Christiansen, 2005; Morse and Burn, 2014; Atchley et al., 2015). This effect is attributed to the thinner snowpack on top of the rims, as wind-driven redistribution of snow enhances accumulation in microtopographic lows. Consistent with these observations, previous conceptual models of the thermal regime of the active layer in ice wedge polygons have incorporated the idea that cooling is enhanced in raised zones, such as rims (Christiansen, 2005; Morse and Burn, 2014) and impeded in low ones (Gamon et al., 2012). However, the strength of these effects, and interactions between them at the polygon scale, remain unclear. For example, if the influence of enhanced cooling in the rims of a low-centered polygon extends to adjacent regions of the subsurface, it seems likely that the gradual development of rims would promote colder temperatures in the ice wedge. This effect would represent a positive feedback on development of low-centered polygons, because colder temperatures favor cracking and the expansion of the ice wedge. On the other hand, it has also been suggested that development of relief in the rims drives precisely the opposite effect, by increasing snow entrapment in the troughs, thereby enhancing insulation of the ice wedges (Lachenbruch, 1966).

Improved understanding of interactions between microtopography, snow depth, and ground temperature is needed to resolve this uncertainty, because feedbacks between these variables may have important ramifications for ice wedge cracking at various stages of microtopographic development. For example, it was argued recently that the presence of secondary ice wedges, or young wedges that subdivide older polygons, results from deactivation of the older primary network due to increased snow entrapment in the troughs, either as the rims grow or the trough itself subsides (Morse and Burn, 2013; Burn and O'Neill, 2015). This conceptual model has important implications for interpretation of both modern wedges and Pleistocene-aged ice wedge casts, and is supported by observations that secondary ice wedges are rare in erosive environments (such as hillslopes) or depositional settings (such as river deltas), where polygon microtopography tends to be muted or non-existent (Mackay, 1990, 1995). However, it competes with a second hypothesis, that secondary wedges are instead reflections of infrequent severe winter conditions, during which cracking in the primary network alone is insufficient to relieve thermal contraction stresses (Dostovalov and Popov, 1966). This latter hypothesis was supported by a numerical model of ground cracking under an imposed tensile stress (Plug and Werner, 2002), but the model was criticized for failing to represent heterogeneity in the subsurface stress field associated with microtopography (Burn, 2004).

Feedbacks between microtopography and subsurface temperatures are likewise relevant to conceptualizing modern thermokarst in the Arctic, as the changing form of polygons may influence the probability of sustained cracking in degraded ice wedges. As permafrost degradation has accelerated in recent decades (Walker et al., 1987; Osterkamp and Romanovsky, 1996; Jorgenson et al. 2006; Raynolds et al., 2014), thaw in the upper portions of ice wedges has increasingly triggered trough subsidence and the destruction of low-centered polygon rims, creating high-centered polygons. Raynolds et al. (2014) condensed years of field observations into a conceptual model of the process, suggesting that, while the degradation of low-centered polygon rims has historically been a reversible process, much recent thermokarst has proceeded to irreversible extents, due to the destruction of an ice-rich “intermediate” or “transition layer” at the top of the permafrost, which normally buffers deeper zones from thaw. Presumably, the permanence (or reversibility) of modern thermokarst will also be determined by the potential for future ice wedge cracking, which will be necessary to re-establish polygon rims. Understanding of the potential for ice wedges in degraded troughs to cool to temperatures suitable for cracking is therefore important for predicting the duration of changes to landscape-scale processes associated with high-centered polygon development, such as increased runoff, decreased evapotranspiration (Liljedahl et al., 2012; 2016), and increased emissions of carbon dioxide (Wainwright et al., 2015).

2.3 Methods

2.3.1 Study area and data acquisition

The study site is within a low-centered polygon network approximately 40 km south of Prudhoe Bay and 1 km west of the Dalton Highway in Alaska’s North Slope Borough (Fig. 2.1a). The surficial geology of the region is dominated by fluvial and marine-fluvial silty sands, associated with streams flowing north from the Brooks Range (Jorgenson and Shur, 2007; Raynolds et al., 2014). These deposits are capped with approximately 2 m of Pleistocene-aged aeolian silt, which grades upward into a surface mantle of peat (Everett, 1980). Active layer thickness varies from 70-90 cm, extending into the aeolian silt layer. Vegetation at the site is typical of the region, and consists almost exclusively of low-lying sedges and grasses. Mean annual air temperature from 2000-2015 was -8.9°C, as estimated by Noah Land Surface Model output from NASA’s Global Land Data Assimilation System (GLDAS), which provides estimates of global weather conditions from year 2000 to the present at a spatial resolution of 0.25° and a temporal resolution of 3 hrs (Rodell et al., 2004).

The microtopography of the studied polygon (outlined in green) is represented in a 50 cm resolution lidar digital elevation model (DEM) (Fig. 2.1b). Like many low-centered polygons south of Prudhoe Bay, the polygon has modest relief compared with polygons elsewhere in the Arctic, with surface elevations ranging from ~78.8-79.2 m above sea level. The relatively low rims and the presence of standing water at the eastern vertex of the polygon suggest that some ice wedge degradation has occurred in recent decades, as documented at nearby sites (Raynolds et al. 2014).

Field work was conducted in late July, 2014 and early September, 2015. During the first visit, temperature “sensor rods” (Alpha Mach, Sainte-Julie, Quebec) were installed across the polygon (locations shown as blue dots in Fig. 2.1b). Each rod was equipped with thermistors embedded in a water-proof plastic pipe, and driven into the active layer to observe temperature at depths of 10, 20, 30, 40, and 50 cm. Each rod contained an onboard power source and data logger programmed to record temperature every three hours. The temperature resolution of the sensors was 0.125°C, and their accuracy was estimated by the manufacturer at ±0.5°C. Sensor rods were installed into a mix of higher-elevation rim sites, and lower-elevation sites from the polygon interiors. Rods were removed and data were downloaded in September, 2015. An example of the data from rod cen1 (Fig. 2.2) displays temperature data from September 2014 through August 2015. Data from all rods are included in the supplement (Fig. 2.1S).

In addition to sensor rod installation, soil cores were collected in 2014 and subsequently analyzed for hydraulic and thermal properties. Soil cores were collected in both the center and the rims, at depths varying from ground surface to 19 cm. Soil cores below 19 cm could not be collected due to a high water table. Laboratory analyses of the soil cores, described in the supplement (Text 3.1S, Table 3.1S), informed the parameterization of our numerical model.

2.3.2 Statistical analysis of observational data

Prior to constructing a numerical model, data from the sensor rods were analyzed to understand differences in the subsurface thermal regime between the rims and other areas of the polygon. The seasonality of these differences was also evaluated to determine the potential relationship with snow cover. A set of one-tailed rank sum tests was used to evaluate the hypothesis that minimum winter temperatures in the rims (n=3) are lower than in the polygon centers (n=6) at all observed depths, and to determine whether the autumn freezing curtain is shorter in the rims than elsewhere. Freezing curtain duration was defined at each sensor as the length of time that ground temperature remained between -0.5°C and 0.5°C, or approximately zero (within the accuracy of the sensors), due to the release of latent heat as soil water freezes. We expected that rims would experience shorter freezing curtains, due to enhanced cooling and decreased soil water content. Finally, to analyze seasonality, the rank sum test was used to determine whether mean monthly temperatures are coldest in the rims, each month from September 2014 through August 2015. We expected that rims would only be colder than the centers during months with significant snow cover.

2.3.3 Overview of the Advanced Terrestrial Simulator

Our numerical model used the Advanced Terrestrial Simulator (ATS, version 0.86), a code developed by the United States Department of Energy within the Amanzi framework (Moulton et al., 2011) to simulate surface and near-surface thermal hydrology in variably saturated media (https://github.com/amanzi/ats). ATS uses a multi-physics process management tool called Arcos (Coon et al., 2015) to allow for flexibility in coupling self-contained models for each component of the physical system (e.g., the subsurface mass balance and the surface energy balance). ATS was chosen for its record of successful application to permafrost terrain (Atchley et al., 2015; 2016; Harp et al., 2016; Sjoberg et al., 2016; Schuh et al., 2017; Jan et al., 2018), and for its rich collection of features tailored to simulating hydrologic processes in cold environments. One component of ATS that is particularly useful for our study is a unique module that emulates wind-blown redistribution of snow across topography using a diffusion-wave equation, taking the same mathematical form as the Mannings equation. This causes snow accumulation to vary inversely with elevation, by leveling the top of the snowpack into a flat surface. In the present implementation, we coupled the subsurface conservation of mass and energy with a surface energy balance model, which was driven by meteorological data and allowed for accumulation of liquid water, ice, and snow at the surface. An overview of the partial differential equations governing surface and subsurface processes is presented in Painter et al. (2016) and in the appendix to this dissertation. A detailed explanation of the surface energy balance, including description of a snowpack aging model used to estimate changing snow thermal conductivity and albedo throughout winter, is presented in Atchley et al. (2015).

2.3.4 Model construction, calibration, and sensitivity analysis

Construction and calibration of the numerical model followed the workflow described by Atchley et al. (2015), with each model run comprising three computer simulations. In the first simulation, a water table was established near the surface in isothermal conditions by defining a constant-pressure (Dirichlet) boundary condition at the bottom of the domain. In the second simulation, permafrost conditions were established by adding a constant-temperature boundary condition at the bottom (50 m depth), allowing the soil column to freeze from below. In the third simulation, the surface energy balance was introduced, employing meteorological data to define transient thermal and hydraulic boundary conditions at the top of the domain.

Due to the availability of field samples used to estimate soil physical properties, and in an effort to avoid over-fitting the model, calibration focused solely on snow pack parameters. As described in the supplement (Text 2.2S), the calibrated parameters included the thermal conductivity of fresh snow, the snow redistribution coefficient used to transport snowpack across variable topography, and a snowfall multiplier used to correct for under-reporting in our meteorological data. For calibration, a 2D domain was developed using topography from the lidar DEM, which included four ground materials (Fig. 2.3). The domain extended laterally from approximately 1 m NW of rod cen3 to 2 m SE of rod cen4, intersecting five sensor rods in different microtopographic positions. The bottom boundary temperature was set at -6°C, characteristic of nearby borehole observations (Romanovsky et al., 2009). To approximate the gradation of surficial peat into mineral soil at our site, the upper 2.5 cm of the soil column was defined as unconsolidated peat, and the next 30 cm as more tightly compacted peat. Soil hydraulic and thermal parameters for these upper layers were assigned using laboratory estimates from the core samples (See supplemental Information for methods (Text 2.2S) and results (Table 2.1S)). The lower soil layers were modeled as mineral soils, to which the ATS default parameters, characteristic of a silty sand, were applied. Ice wedges were included beneath the troughs at a depth of 80 cm, consistent with an active layer survey conducted in September, 2015. Physical parameters for all ground materials used in the model are summarized in Table 2.1.

Meteorological variables used to drive simulations included air temperature, wind speed, incident shortwave radiation, longwave radiation, relative humidity, rainfall, and snowfall. Time series of each variable were derived from the output of the Noah Land Surface Model as distributed by GLDAS (Rodell et al., 2004). Meteorological data were extracted from the pixel centered at 148.875°W, 69.875°N (approximately 5 km from our field site) for the time period from September 1, 2010-August 31, 2015, and each variable was averaged into daily means. The first four years of this period were used as spin-up, and the fifth year was used to compare simulated against observed temperatures.

After obtaining a suitable calibration using field site microtopography, a sensitivity analysis was conducted by repeating simulations with hydraulic and thermal parameters held constant, but with the height of the rims and the depth of the troughs being systematically altered. Following each simulation, winter temperatures were extracted from 2014-2015 from the uppermost cell at the center of the SE (right) ice wedge, and compared to the criteria identified by Morse and Burn (2013) that favor ice wedge cracking. Simulations scanned through 6 different rim heights, varying from -10 cm to +15 cm in increments of 5 cm; and 5 different trough depths, varying from unchanged to 40 cm deeper, in increments of 10 cm. These ranges were chosen to recreate the variability observed near our field site and to match recent documentation of troughs impacted to various degrees by ice wedge degradation (Jorgenson et al., 2006).

The ensemble of topographies for our analysis (Fig. 2.4) was created by altering the original mesh representing field site topography. When either trough depth or rim height was increased, elevation at every rim or trough node was directly reassigned. Abolt et al. (2017) showed that the progression of polygonal topography from low-centered to high-centered form is closely approximated by the linear hillslope diffusion equation; therefore, when relief was reduced in the rims, a linear diffusion operator was applied to all non-trough nodes until the elevation of the southeast rim decreased by the desired amount. This procedure reproduced the smooth, convex-up topography of a high-centered polygon.

2.4 Results

2.4.1 Statistical analysis of observational data

Minimum winter temperatures (Table 2.2) and freezing curtain durations (Table 2.3) observed among all sensor rods showed considerable variability, with temperatures in the rims becoming colder and falling below 0°C sooner than those in the centers. The results of the rank sum tests (Table 2.4) confirm that the difference between minimum winter temperature in the rims and in the centers is significant at all depths ($p < 0.025$, indicating a low probability that variations could be explained by random processes), with median differences varying from 3.2°C at 10 cm to 2.3°C at 50 cm depth. Similarly, freezing curtains are shorter in the rims than the centers at all observed depths ($p < 0.025$), the median difference being approximately 10 days.

The results of the rank sum tests, evaluating the hypothesis that rims experience mean monthly temperatures colder than the centers, reveal a stark seasonal pattern in which rims are significantly colder than the center ($p < 0.1$) only during the winter (Fig 5). The difference first becomes significant at a depth of 10 cm in October, but requires an additional two months to become significant at a depth of 50 cm. Rims remain significantly colder than centers through the month of March, after which there is no significant difference through the period of observation.

2.4.2 Model calibration

Results from the model calibration indicate that the best-performing snowfall multiplier was 1.7. Using this value, maximum snow depth in the center of the polygon during the winter of 2014-2015 was approximately 45 cm, comparing well with ground observations from SNOTEL stations at Deadhorse and Sagwon (approximately 40 km north and 40 km south of the study site, with maximum depths of 53 cm and 58 cm, respectively; data available at https://www.wcc.nrcs.usda.gov/snow/). The optimal thermal conductivity for freshly fallen snow was 0.021 W m-1 K-1, which is within the range of recently published field measurements (Riche and Scheebeli, 2013; Domine et al., 2016). Additionally, the snow redistribution coefficient was reduced 60% from the ATS default value, effectively increasing the speed with which the snowpack developed a level surface in winter. Using these parameters, RMSE between simulated and observed daily temperature from the year of observation, incorporating all 25 sensors embedded in the 2D transect (5 thermistors in each of 5 sensor rods), was approximately 1.0°C. RMSE at individual rods varied from ~1.4°C at rod cen4 to ~0.7°C at rod cen3. Plots comparing simulated and observed ground temperature at rods cen1 and rim1 demonstrate a close visual match (Fig. 2.6). A snapshot of simulated ground temperature and snowpack on December 24, 2014 (Fig. 2.7) clearly illustrates zonation in the ground thermal regime, whereby the rims become the coldest zone of the polygon.

Although model calibration focused on thermal properties of the snowpack, we found that accurately specifying soil physical properties, including unsaturated hydraulic parameters, was essential to reproducing observed ground temperatures. We note that, in simulations initially constructed using the default soil hydraulic parameters employed by ATS (calibrated at the Barrow Environmental Observatory site near Utqiaġvik, Alaska), high rates of evaporation at the soil surface caused the active layer to be nearly dry by the end of the summer. Thermal conductivity was hence reduced within the well-drained soil, resulting in an inaccurate simulation of ground temperature. In contrast, when soil hydraulic parameters derived from laboratory analysis of soil cores at our field site were used, the water table remained within ~15 cm of the surface elevation at the polygon center throughout the summer, as it was during the field campaigns in July 2014 and August 2015 (Fig. 2.8). This improved representation of the ground hydrologic regime complemented the close match between observed and simulated ground temperatures (Fig. 2.6).

2.4.3 Sensitivity analysis

The criteria we used to determine favorable conditions for ice wedge cracking were whether winter 2014-2015 temperatures at the top of the southeast ice wedge cooled below -13°C, and whether the rate of cooling surpassed 0.1°C d^{-1} for two days or more (Morse and Burn, 2013). The range of topographies simulated in our sensitivity analysis straddled these conditions (Table 2.5), with minimum temperatures at the top of the ice wedge varying from -15.16°C in a polygon with rims 15 cm higher and a trough the same depth as our field site, to -12.87°C in a polygon with rims 10 cm lower and a trough 40 cm deeper. In all cases in which temperature cooled below -13°C, the rate of cooling was sufficient to favor cracking. Minimum winter temperature in the ice wedge increased with trough depth in almost all cases, and always decreased with rim height. Cracking was determined to be favorable in most simulations, as the ice wedge failed to cool below -13°C only when rim height was less than our field site and trough depth was greater.

2.5 Discussion

2.5.1 Zonation in the subsurface thermal regime at our field site

Data from our field site demonstrated a clear pattern in which low-centered polygon rims become the coldest region of the subsurface in winter, even in a polygon with relatively modest relief. The stark seasonality of this pattern, whereby rims become colder than the centers only after snow has accumulated on the ground, is consistent with the hypothesis that most of the variation in subsurface temperatures can be explained by snow depth variation associated with microtopography. Although this finding was expected, our 2D model using field site topography is, to our knowledge, the first physical simulation at the polygon scale to demonstrate that depth variation induced by leveling of the snowpack surface is sufficient to explain observed zonation in the subsurface thermal regime. Our confidence in the model is reinforced by the low RMSE between observed and simulated temperatures, obtained using soil physical parameters derived from core samples and a calibrated estimate of snow thermal conductivity that fits recent field measurements (Riche and Scheebeli, 2013; Domine et al., 2016).

The findings from our rank sum tests, that even relatively small rims become colder than the polygon centers in winter, and that rims fully freeze before the rest of the polygon, support the hypothesis that rims are sites of enhanced cooling in low-centered polygons, as suggested by Christiansen (2005). These findings are also consistent with data and a conceptual model presented by Morse and Burn (2014), who argued that the early completion of freeze up in the rims creates a closed hydrologic system in low-centered polygons, which drives the formation of frost blisters when the active layer is saturated. Our simulation results imply that the effects of enhanced cooling in the rims extend to adjacent regions of the subsurface, as temperature gradients throughout the active layer in early winter favor the transfer of heat from the center and the troughs toward the rims (Fig. 2.7). Complementing this trend, a number of physical factors underscore the potential for rims to act as preferential outlets of subsurface energy. Because the rims are the first region of the polygon to experience sub-freezing temperatures, laterally-oriented thermal gradients are established early in winter, just as large quantities of latent heat are released by phase change of soil water (from liquid to solid) in the centers and troughs. At precisely the same time, the thermal conductivity of soil in the rims also increases abruptly due to freezing. Working in unison, these factors can deliver a considerable boost to freezing and cooling processes in subsurface regions adjacent to the rim, including the ice wedge.

2.5.2 Sensitivity of ice wedge temperatures to topography

The key insight delivered by our sensitivity analysis is that both trough depth and rim height have substantial influence on wintertime temperatures in the ice wedge. Unsurprisingly, deeper troughs are associated with warmer ice wedge temperatures, due to increased insulation of the active layer directly above the wedge. Perhaps less intuitively, however, rim height appears to hold even greater influence on the thermal regime of the ice wedge: leaving other factors constant, varying rim height across a 25 cm range produced up to a 2.1 ° C change in minimum ice wedge temperature, compared with 1.1 ° C of variation associated with a 40 cm range of trough depth (Table 2.5). Rims in our simulations consistently acted as preferential outlets of energy from the subsurface in winter, because in all cases, increased rim heights were associated with colder ice wedge temperatures, due to lateral heat conduction from the troughs. The relatively high sensitivity of ice wedge temperature to rim height implies that most of the cooling experienced by the ice wedge in winter occurs through the rims, rather than through the active layer of the troughs. Moreover, the proportion of cooling attributable to the rim increases with rim size, because larger rims decrease the sensitivity of ice wedge temperature to trough depth (Table 2.5).

Compared with the criteria determined by Morse and Burn (2013), our results suggest that this variability in ice wedge temperature may determine whether or not a crack occurs in a given winter. This conclusion is supported by prior field studies. In Svalbard, for example, Christiansen (2005) suggested that most of the cooling experienced by an ice wedge occurs through the rims, and Watanabe et al. (2017) observed that ice wedge cracking is most active in polygons with well-developed rims hosting minimal snow cover. Along the Beaufort Sea coast in north-western Canada, it has been observed that ice wedges beneath well-developed troughs crack infrequently, presumably due to the insulation provided by increased snow cover (Mackay, 2000; Burn, 2004). These observations affirm that the effects of rim and trough morphology on the ground thermal regime at the periphery of the polygon are sufficient to change the frequency of cracking events.

One practical implication of our results is that the effects of a deep trough on cracking behavior are minimized if large rims are maintained, but become more significant as rims are destroyed. For example, in the final year of our simulations, ice wedge temperatures do not reach -13 ° C in a polygon with rims smaller than our field site and a trough 40 cm lower, representing an advanced stage of thermokarst development. On the other hand, ice wedge temperatures drop considerably below -13 ° C in a polygon that has equally degraded troughs, but has rims 15 cm higher than the field site, a form resembling the enigmatic "fortress polygons" described by Root (1978) and Mackay (2000). This finding implies that ice wedge cracking is far more favorable, and therefore more frequent, in fortress polygons as compared with high-centered polygons, despite that both forms represent thermokarst trajectories (Mackay, 2000). Moreover, this mechanism could help explain the persistence of low-centered form in fortress polygons, which would be reinforced by sustained ice wedge growth.

The role of rims as preferential outlets of subsurface heat is consistent with the idea that topographic highs in ice wedge polygons cool more efficiently than depressed areas (Christiansen, 2005; Gamon et al., 2012; Watanabe et al., 2017), but conflicts with the idea previously suggested by Lachenbruch (1966), that rim development gradually suppresses ice wedge cracking by increasing snow entrapment in the troughs. It is important to acknowledge that our model does not fully negate Lachenbruch's hypothesis, as conditions not incorporated into the sensitivity analysis, such as vegetation differences between the rims and center, can also influence snow accumulation patterns and energy exchange between the ground and atmosphere (Gamon et al., 2012). Nonetheless, our results strongly suggest that, considered as an independent variable, increased rim height enhances wintertime cooling in the ice wedge.

Overall, our analysis strongly affirms the idea that the microtopography of ice wedge polygons drives considerable and systematic spatial variation in the subsurface thermal regime, which must be considered in any conceptualization of ground thermal contraction stresses (Lachenbruch, 1962; 1966; Burn, 2004; Morse and Burn, 2013; Burn and O'Neill, 2015). Regarding historical polygon development, our results support the hypothesis of Morse and Burn (2013) and Burn and O'Neill (2015) that feedbacks associated with microtopographic change are sufficient to explain the presence of secondary wedges in modern and ancient polygons, as rim destruction and trough deepening are common events across much of the tundra, and both suppress the potential for cracking. This conclusion is important for interpretation of relict ice wedge casts, because it implies that the absence of secondary ice wedges, rather than reflecting a climatic signal, may indicate that wedges grew syngenetically (i.e., in an aggrading landscape) or anti-sygenetically (in an erosive landscape). Modern wedges found in such systems are associated with only modest, or altogether absent, microtopography (Mackay, 1990; 1995; Burn and O'Neill, 2015), and surveys using ground penetrating radar in these settings confirm that secondary wedges are rare, even in polygons old enough to have been exposed to many extreme winters (Morse and Burn, 2013). In contrast, both the development of microtopography and deformation through thermokarst processes tend to be more pronounced above epigenetic ice wedges (i.e., those forming below stable ground surfaces, such as our field site). If the primary ice wedges in such settings are deactivated through a combination of rim destruction and trough deepening, a secondary wedge may form so long as thermal conditions in the center of the polygon remain favorable for cracking. The new wedge would be initiated by contraction stresses which had been relieved in previous winters through activity in the primary network. Cracking in the new wedge would become increasingly frequent if rims begin to develop adjacent to it, or if the troughs above the primary network continue to subside.

This same concept, that low rims and deep troughs suppress ice wedge cracking, also has important implications regarding the permanence of recent thermokarst development across the Arctic (e.g., Jorgenson et al., 2006; Liljedahl et al., 2016). It has already been emphasized that the destruction of an ice-rich transition layer at the top of the permafrost may render irreversible much of the regional-scale thermokarst observed in the past three decades (Raynolds et al., 2014). Our model indicates that changes to topography associated with ice wedge thaw compound this effect, as the development of high-centered polygon mictrotopography impedes the ability of the ice wedge to cool to temperatures favorable for cracking, even relative to scenarios with minimal microtopography (Table 2.5). Because of this topographic disadvantage, the ice wedges surrounding high-centered polygons should crack infrequently, and might only return to normal levels of activity if the winter climate becomes colder (or less snowy) than the conditions in which the wedges first formed. Therefore, the re-establishment of rims in thermokarst terrain is unlikely should future air temperatures remain on a warming trajectory, or even if the climate stabilizes. This implies that regional scale changes to tundra hydrology (Liljedahl et al., 2012; 2016) and microbial processing of soil organic carbon (Zona et al., 2011;

Wainwright et al., 2015) associated with high centered polygon development are likely to persist, once initiated, for timescales mirroring regional climate fluctuations.

2.6 Conclusions

Our analysis of observational data confirms that the microtopography of ice wedge polygons drives considerable, systematic variation in near surface ground temperatures, even in a set of polygons with relatively modest relief. This variation is most notable in winter, as subsurface cooling is most efficient beneath microtopographic highs and impeded beneath microtopographic lows. Our numerical model reveals that rims act as preferential outlets of subsurface heat in low-centered polygons, because lateral temperature gradients drive energy transfer from adjacent regions of the subsurface toward the rims in winter. Therefore, increased rim size drives colder temperatures in the ice wedge. Rim size and trough depth represent critical factors influencing whether an ice wedge becomes cold enough to crack during winter. Therefore, feedbacks between microtopographic change and subsurface temperatures can explain deactivation of the primary network and development of secondary ice wedges in modern and ancient polygons. The absence of secondary ice wedges in relict cast systems may reflect syngenetic or anti-syngenetic growth, which tends to result in muted microtopography, rather than a climatic signal. Because decreased rim size and increased trough depth both suppress ice wedge cracking, development of modern thermokarst topography is likely to reduce rates of ice wedge growth, precluding the re-establishment of rims around degraded troughs.

ACKNOWLEDGEMENTS

We are grateful for the support provided for this research, which included: NASA's Jet Propulsion Laboratory under contract #C021199 (Erika Podest is our Project Manager); the NASA Earth and Space Science Fellowship program, for an award to CJA (80NSSC17K0376); the Next Generation Ecosystem Experiments Arctic (NGEE-Arctic) project (DOE ERKP757) funded by the Office of Biological and Environmental Research in the US Department of Energy Office of Science; and Todd Caldwell and Toti Larson (Bureau of Economic Geology, The University of Texas at Austin) for lively conversation and contributions to field work. We thank the editor and two anonymous reviewers for detailed and constructive suggestions for revisions to the manuscript.

Table 2.1

Ground physical (hydraulic and thermal) properties used in model.

Ground material	Porosity ϕ $m^3\ m^{-3}$	Residual water content ϑ_r $m^3\ m^{-3}$	van Genuchten parameter α cm^{-1}	van Genuchten parameter m *unitless*	Intrinsic permeability k m^2	Saturated (thawed) thermal conductivity λ_s $W\ m^{-1}\ K^{-1}$	Saturated (frozen) thermal conductivity λ_{sf} $W\ m^{-1}\ K^{-1}$	Dry thermal conductivity λ_u $W\ m^{-1}\ K^{-1}$
Upper peat	0.80	0.08	0.02	0.30	$5 \cdot 10^{-11}$	0.6	1.8	0.10
Lower peat	0.70	0.07	0.02	0.40	$2 \cdot 10^{-12}$	0.75	1.9	0.12
Mineral soil	0.50	0.10	$5.4 \cdot 10^{-4}$	0.19	$2 \cdot 10^{-13}$	1.0	2.0	0.29
Ice wedge	0.99	0.00	$5.4 \cdot 10^{-4}$	0.19	0.0	0.59	2.2	N/A

Table 2.2

Minimum observed temperature (°C) at each sensor rod and depth (cm).

Depth	cen1	cen2	cen3	cen4	cen5	cen6	rim1	rim2	rim3	Center Median	Rim Median
10	-19.0	-17.7	-16.1	-16.0	-18.0	-19.9	-21.1	-19.8	-22.5	-17.8	-21.1
20	-18.3	-19.1	-15.7	-15.1	-17.2	-19.2	-19.9	-18.4	-20.8	-17.1	-19.7
30	-17.7	-16.4	-15.3	-14.6	-16.5	-18.3	-19.0	-18.0	-19.7	-16.4	-19.0
40	-16.8	-15.6	-14.3	-14.0	-15.7	-17.6	-18.0	-17.2	-18.7	-15.7	-18.0
50	-16.1	-15.1	-13.8	-13.5	-15.0	-16.4	-17.3	-16.5	-18.0	-15.0	-17.3

Table 2.3

Freezing curtain duration (days) at each sensor rod and depth (cm).

Depth	cen1	cen2	cen3	cen4	cen5	cen6	rim1	rim2	rim3	Center Median	Rim Median
10	37.5	41.6	42.9	38.5	38.5	37.6	29.5	29.6	28.3	38.5	29.5
20	54.3	57.1	58.0	34.6	49.8	52.8	38.8	41.9	39.5	54.4	39.5
30	59.8	64.1	65.0	62.1	57.1	59.4	52.5	57.0	50.8	60.9	52.5
40	68.6	72.0	74.1	71.5	61.5	64.9	58.4	67.9	58.1	68.6	58.4
50	77.1	77.4	80.8	81.8	68.5	75.6	65.0	68.0	64.1	77.3	65.0

Table 2.4

Rank sum test results (p-values) for two hypotheses.

Hypothesis	Depth (cm)				
	10	20	30	40	50
Rims have colder minimum temperatures than centers.	0.024	0.024	0.024	0.024	0.012
Rims have shorter freezing curtains than centers.	0.012	0.012	0.012	0.024	0.012

Table 2.5

Sensitivity analysis: minimum simulated temperature at top of ice wedge (°C).

Trough manipulation (cm)	Rim manipulation (cm)					
	-10	-5	0	+5	+10	+15
0	-13.94	-14.08	-14.37	-14.56	-14.92	-15.16
-10	-13.18	-13.42	-14.07	-14.39	-14.87	-14.98
-20	-12.88	-13.33	-13.85	-14.13	-14.57	-15.00
-30	-12.99	-13.11	-13.52	-13.99	-14.34	-14.71
-40	-12.87	-12.98	-13.38	-13.89	-14.28	-14.57

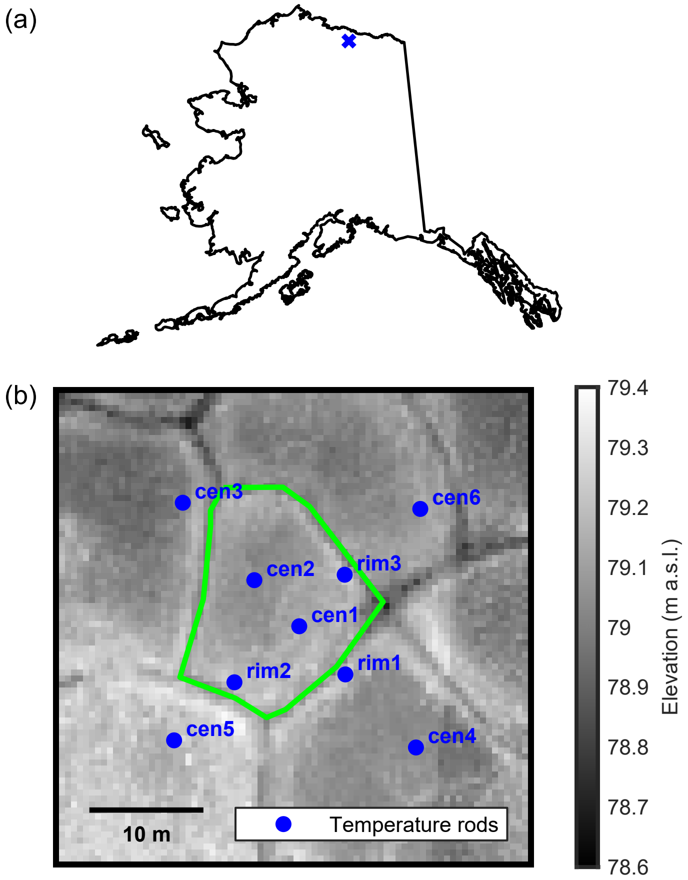

Figure 2.1

Location of field site **(a)** and 50 cm resolution lidar DEM with ice wedge polygon extent and temperature sensor rod locations indicated **(b)**.

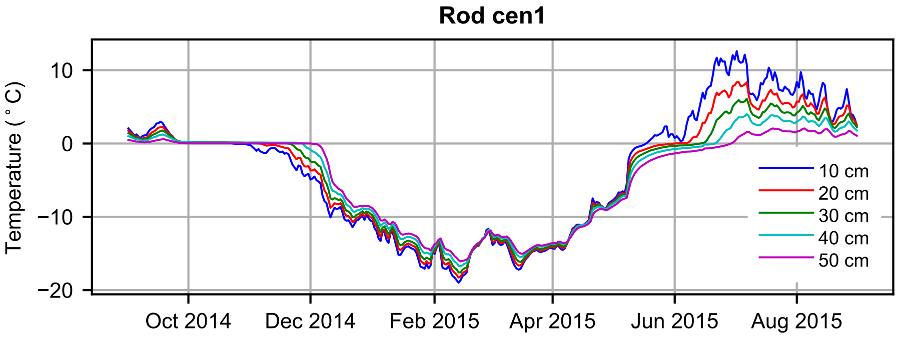

Figure 2.2

Sample of observed temperature data from sensor rod cen1.

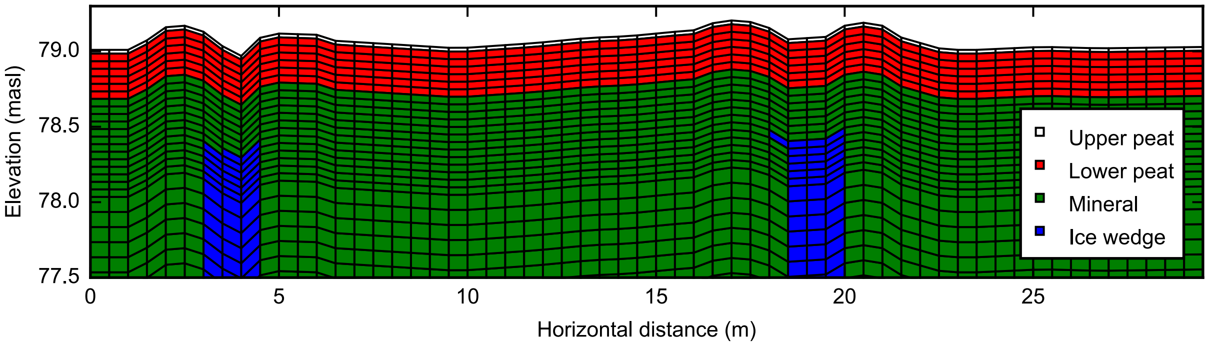

Figure 2.3

Schematic of the near-surface portion of the 2D mesh of the field site (vertical exaggeration=4). Mesh extends to 50 m below the ground surface.

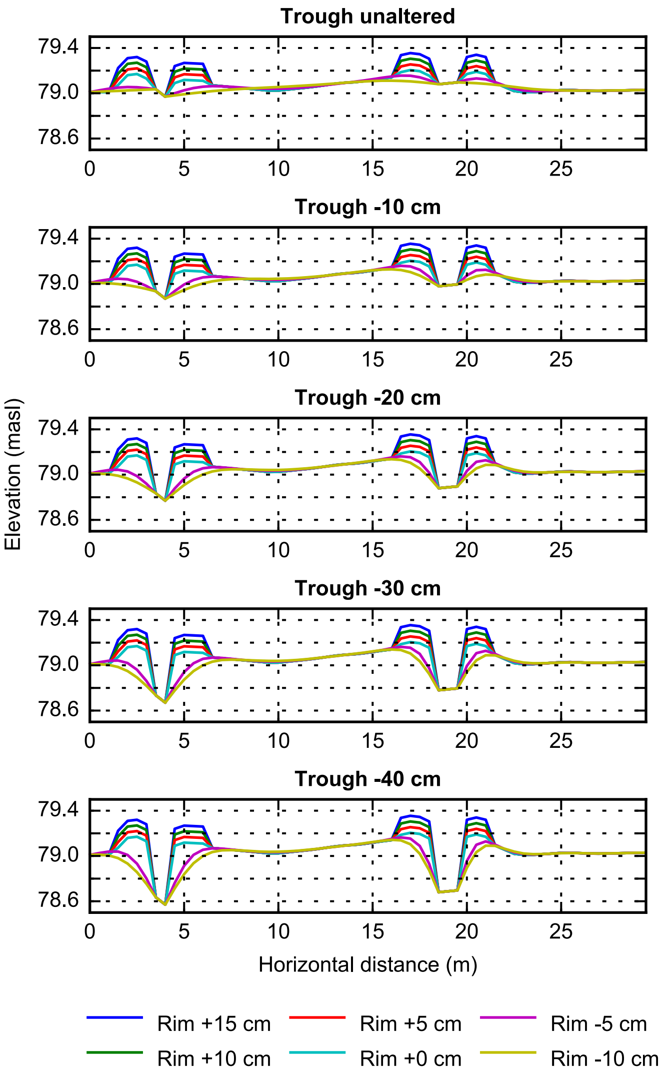

Figure 2.4

Schematic illustrating the range of topographic conditions explored in the sensitivity analysis (vertical exaggeration=6).

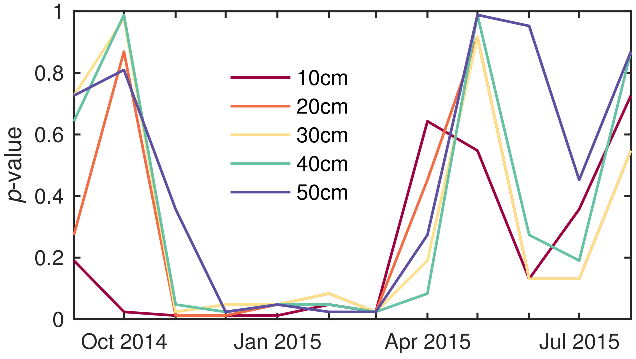

Figure 2.5

Results of the rank sum test, evaluating whether mean monthly temperatures are colder in the rims than in the centers.

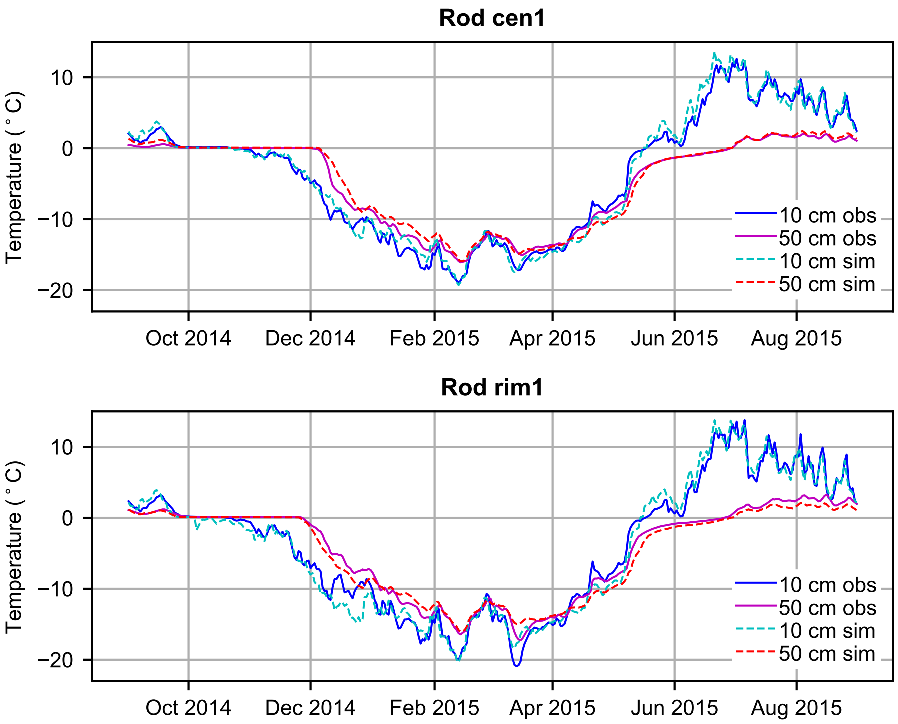

Figure 2.6

Observed and simulated ground temperature from calibrated 2D simulation, at temperature sensor rods cen1 and rim1.

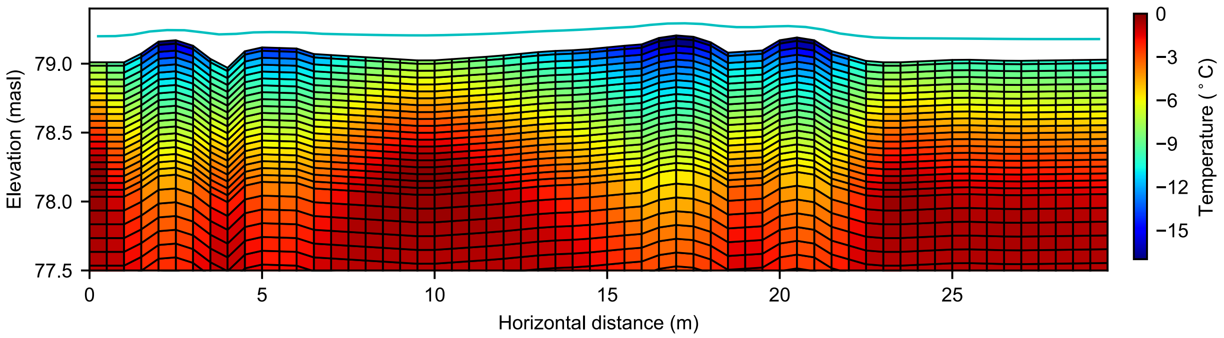

Figure 2.7

Snapshot of simulated snowpack surface (cyan line) and ground temperature on December 24, 2014 (vertical exaggeration=4). Only near-surface is shown; spatial domain of simulation extends to 50 m below the ground surface.

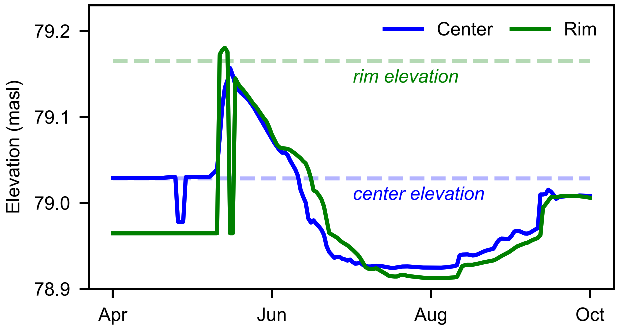

Figure 2.8

Simulated water table elevation at the center and at the northwest rim of the main polygon during the summer of 2015. The water table remains relatively close to the ground surface at the polygon center throughout the season, as observed during field work in August 2015.

References

Abolt CJ, Young MH, Caldwell TG. 2017. Numerical modelling of ice-wedge polygon geomorphic transition. *Permafrost and Periglacial Processes* **28**: 347–355.

Allard M, Kasper JN. 1998. Temperature conditions for ice-wedge cracking: Field measurements from Salluit, northern Quebec. In: Proceedings of the Seventh International Conference on Permafrost, pp. 5–12, National Research Council of Canada.

Atchley AL, Painter SL, et al. 2015. Using field observations to inform thermal hydrology models of permafrost dynamics with ATS (v0.83). *Geoscientific Model Development* **8**: 2701–2722.

Atchley AL, Coon ET, et al. 2016. Influences and interactions of inundation, peat, and snow on active layer thickness. *Geophysical Research Letters* 43: GL068550.

Burn CR. 2004. A field perspective on modelling 'single-ridge' ice-wedge polygons. *Permafrost and Periglacial Processes* **15**: 59–65.

Burn CR, O'Neill HB. 2015. Subdivision of ice-wedge polygons, western Arctic coast. Canadian Geotechnical Society. Quebec, QC.

Christiansen HH. 2005. Thermal regime of ice-wedge cracking in Adventdalen, Svalbard. *Permafrost and Periglacial Processes* **16:** 87-98.

Coon ET, Moulton D, Painter SL. 2016. Managing complexity in simulations of land surface and near-surface processes. *Environmental Modelling & Software* **78**: 134–149.

Domine F, Barrere M, Sarrazin D. 2016. Seasonal evolution of the effective thermal conductivity of the snow and the soil in high Arctic herb tundra at Bylot Island, Canada. *The Cryosphere* **10**: 2573–2588.

Dostovalov BN, Popov AI. 1966. Polygonal systems of ice-wedges and conditions of their development. In: Proceedings of the International Conference on Permafrost, pp. 71–76, National Academy of Sciences-National Research Council.

Fortier D, Allard M. 2005. Frost-cracking conditions, Bylot Island, eastern Canadian Arctic archipelago. *Permafrost and Periglacial Processes* **16**: 145–161.

Gamon JA, Kershaw GP, et al. 2012. Microtopographic patterns in an arctic baydjarakh field: do fine-grain patterns enforce landscape stability? *Environmental Research Letters* **7**: 015502.

Goodrich LE. 1982. The influence of snow cover on the ground thermal regime. *Canadian geotechnical journal* **19**: 421–432.

Harp DR, Atchley AL, et al. 2016. Effect of soil property uncertainties on permafrost thaw projections: a calibration-constrained analysis. *The Cryosphere* **10**: 341–358.

Isarin RFB. 1997. Permafrost distribution and temperatures in Europe during the Younger

Dryas. *Permafrost and Periglacial Processes* **8**: 313–333.

Jan A, Coon ET, et al. 2018. An intermediate-scale model for thermal hydrology in low-relief permafrost-affected landscapes. *Computational Geosciences* **22**: 163-177.

Johnson WH. 1990. Ice-wedge casts and relict patterned ground in central Illinois and their environmental significance. *Quaternary Research* **33**: 51–72.

Jorgenson MT, Shur YL, Pullman ER. 2006. Abrupt increase in permafrost degradation in Arctic Alaska. *Geophysical Research Letters* **33**: GL024960.

Jorgenson MT, Shur Y. 2007. Evolution of lakes and basins in northern Alaska and discussion of the thaw lake cycle. *Journal of Geophysical Research* **112**: JF000531.

Jorgenson MT, Kanevskiy M, et al. 2015. Role of ground ice dynamics and ecological feedbacks in recent ice wedge degradation and stabilization. *Journal of Geophysical Research: Earth Surface* **120**: 2280–2297.

Kanevskiy M, Shur Y, et al. 2013. Ground ice in the upper permafrost of the Beaufort Sea coast of Alaska. *Cold Regions Science and Technology* **85**: 56-70.

Kokelj SV, Pisaric MFJ, Burn CR. 2007. Cessation of ice wedge development during the 20th century in spruce forests of eastern Mackenzie Delta, Northwest Territories, Canada. *Canadian Journal of Earth Sciences* **44**: 1503–1515.

Kokelj SV, Lantz TC, et al. 2014. Distribution and activity of ice wedges across the forest-tundra transition, western Arctic Canada. *Journal of Geophysical Research: Earth Surface* **119**: 2032-2047.

Lachenbruch AH. 1962. Mechanics of thermal contraction cracks and ice-wedge polygons in permafrost. Geological Society of America Special Paper 70.

Lachenbruch AH. 1966. Contraction theory of ice-wedge polygons: A qualitative discussion. In: Proceedings of the International Conference on Permafrost, pp. 63–70, National Academy of Sciences-National Research Council.

Leffingwell EK. 1915. Ground-ice wedges, the dominant form of ground-ice on the north coast of Alaska. *Journal of Geology* **23**: 635-654.

Liljedahl AK, Hinzman LD, Schulla J. 2012. Ice-wedge polygon type controls low-gradient watershed-scale hydrology. *Tenth International Conference on Permafrost*: Salekhard, Russia. June 25-29.

Liljedahl AK, Boike J, Daanen RP, et al. 2016. Pan-Arctic ice wedge degradation in warming permafrost and its influence on tundra hydrology. *Nature Geoscience* **9**, 312-318.

Mackay JR. 1984. The direction of ice-wedge cracking in permafrost: Downward or upward? *Canadian Journal of Earth Sciences* **21**: 516-524.

Mackay JR. 1990. Some observations on the growth and deformation of epigenetic, syngenetic, and anti-syngenetic ice wedges. *Permafrost and Periglacial Processes* **1**: 15-29.

Mackay JR. 1993. Air temperature, snow cover, creep of frozen ground, and the time of ice-wedge cracking, western Arctic coast. *Canadian Journal of Earth Sciences* **30**: 1720–1729.

Mackay JR. 1995. Ice wedges on hillslopes and landform evolution in the late Quaternary, western Arctic coast, Canada. *Canadian Journal of Earth Science* **32**: 1093-1105.

Mackay JR. 2000. Thermally induced movements in ice-wedge polygons, western Arctic coast: A long-term study. *Géographie Physique et Quarternaire* **54**: 41-68.

Mackay JR, MacKay DK. 1974. Snow cover and ground temperatures, Garry Island, NWT. *Arctic*: 287–296, 1974.

Morse PD, Burn CR. 2013. Field observations of syngenetic ice wedge polygons, outer Mackenzie Delta, western Arctic coast, Canada. *Journal of Geophysical Research: Earth Surface* **118**: 1320-1332.

Morse PD, Burn CR. 2014. Perennial frost blisters of the outer Mackenzie Delta, western Arctic coast, Canada. *Earth Surface Processes and Landforms* **39**: 200-213.

Moulton D, Buksas M, et al. 2011. High-level design of Amanzi, the multi-process high performance computing simulator. United States Department of Energy.

O'Neill HB, Christiansen HH. 2018. Detection of ice wedge cracking in permafrost using miniature accelerometers. *Journal of Geophysical Research: Earth Surface* **123**: JF004343.

Osterkamp TE, Romanovsky VE. 1996. Characteristics of changing permafrost temperatures in the Alaskan Arctic, U.S.A. *Arctic and Alpine Research* **28**: 267.

Painter SL, Coon ET. 2016. Integrated surface/subsurface permafrost thermal hydrology: Model formulation and proof-of-concept simulations. *Water Resources Research* **52**: 6062-6077.

Plug L, Werner B. 2002. Nonlinear dynamics of ice-wedge networks and resulting sensitivity to severe cooling events. *Nature* **417**: 929–933.

Raynolds MK, Walker DA, et al. 2014. Cumulative geoecological effects of 62 years of infrastructure and climate change in ice-rich permafrost landscapes, Prudhoe Bay Oilfield, Canada. *Global Change Biology* **20**: 1211-1224.

Riche F, Schneebeli M. 2013. Thermal conductivity of snow measured by three independent methods and anisotropy considerations. *The Cryosphere* **7**: 217–227.

Rodell M, Houser PR, et al. 2004. The Global Land Data Assimilation System. *Bulletin of the American Meteorological Society* **85**: 381–394.

Romanovsky V, Kholodov A, et al. 2009. Network of Permafrost Observatories in North America: Temperature in deep boreholes. Arctic Data Center.

Root JD. 1975. Ice-wedge polygons, Tuktoyaktuk area, N.W.T. Geological Survey of Canada.

Schuh C, Frampton A, Christiansen HH. 2017. Soil moisture redistribution and its effect on inter-annual active layer temperature and thickness variations in a dry loess terrace in Adventdalen, Svalbard. *The Cryosphere* **11**: 635-651.

Sjoberg Y, Coon ET, et al. 2016. Thermal effects of groundwater flow through subarctic fens: A case study based on field observations and numerical modeling. *Water Resources Research* **52**: 1591-1606.

Wainwright HM, Dafflon B, Smith LJ, et al. 2015. Identifying multiscale zonation and assessing the relative importance of polygon geomorphology on carbon fluxes in an Arctic tundra ecosystem. *Journal of Geophysical Research: Biogeosciences* **120**, 788-808.

Wainwright HM, Liljedahl AK, et al. 2017. Mapping snow depth within a tundra ecosystem using multiscale observations and Bayesian methods. *The Cryosphere* **11**: 857–875.

Walker DA, Webber PJ, et al. 1987. Cumulative impacts of oil fields on northern Alaskan landscapes. *Science* **238**: 757–761.

Walters JC. 1994. Ice-wedge casts and relict patterned-ground in northeast Iowa, USA. *Permafrost and Periglacial Processes* **5**: 269–281.

Watanabe T, Matsuoka N, et al. 2017. Soil physical and environmental conditions controlling patterned ground variability at a continuous permafrost site, Svalbard. *Permafrost and Periglacial Processes* **28**: 433-445.

Wind GP. 1969. Capillary conductivity data estimated by a simple method. In: Water in the unsaturated zone: Proceedings of the Wageningen Symposium, vol. 1, pp. 181–191, International Association of Scientific Hydrology.

Yang D, Goodison BE, et al. 1998. Adjustment of daily precipitation data at 10 climate stations in Alaska: Application of World Meteorological Organization intercomparison results. Water Resources Research **34**: 241–256.

Zona D, Lipson DA, Zulueta RC, Oberbauer SF, Oechel WC. 2011. Microtopographic controls on ecosystem functioning in the Arctic Coastal Plain. *Journal of Geophysical Research* **116**: G001241.

Text 2.1S Description of model calibration

In the first iteration of model construction and calibration, we conducted simulations using a one-dimensional domain, to speed up computational times while coarse tuning the model. The 1D domain preserved the same layering as the 2D mesh but did not include ice wedge cells. The domain was 50 m deep, and the same boundary conditions were applied as in the 2D simulations.

The sole parameter tuned during 1D simulations was a snowfall multiplication factor. It is well-known that records of snowfall frequently underestimate the real precipitation rate. A study of 10 National Weather Service stations in Alaska, for example, found snowfall estimates were systematically underestimated by as much as 140% (Yang et al., 1998), and Atchley et al. (2015) found it necessary to augment snowfall rates observed at a weather station near Barrow, AK ~40% to reproduce the active layer thermal regime in 1D thermal hydrology simulations. To compensate for potential underestimation of snowfall in our meteorological data, we ran a set of simulations in which GLDAS snowfall was increased by factors of 0-100% in increments of 10%. Following each simulation, we extracted temperatures at depths of 10, 20, 30, 40, and 50 cm for comparison with observational data from rod a101, which was intermediate in elevation among the sensor rods. The best performing multiplication factor was 1.8, which we interpreted as providing a rough estimate of the true snowfall rate.

In the second stage of model calibration we expanded into 2D simulations. During this stage, two additional snowpack parameters were tuned heuristically. The first, snow thermal conductivity, is represented in ATS as an empirical function of snow density (which increases with age) (Goodrich, 1982). By default, ATS assigns fresh snow a density of 100 kg m^{-3} and a thermal conductivity of 0.029 W m^{-1} K^{-1}. We explored values between half and double the default thermal conductivity, in accordance with recent measurements by Domine et al. (2016) and Riche and Scheebeli (2013). The second parameter we tuned was the diffusion-like coefficient used by ATS to redistribute snow across topography. We explored values within an order of magnitude in either direction of its default, effectively altering the speed with which the snowpack develops a level surface during the course of winter. In addition to these two parameters, we explored values of the snowfall augmentation factor within ±20% of the coarse-tuned estimate from the 1D simulations. Following every 2D run, we extracted simulated temperature from 2014-2015 for comparison with observations at the five rods intersecting the transect, then made a decision in which direction to tune each parameter.

Text 2.2S Estimation of soil physical parameters from core samples

The water retention curve in ATS is parameterized using the van Genuchten model. Necessary parameters include saturated volumetric water content (ϑ_s, m^3 m^{-3}), residual water content (ϑ_r, m^3 m^{-3}), inverse air entry potential (α, cm^{-1}), and the shape parameter, m (unitless). We estimated the van Genuchten parameters for each soil core using a HYPROP system (METER Group, Pullman, Washington, USA), which employs the Wind evaporation method (Wind, 1968) to estimate unsaturated hydraulic properties while an initially saturated soil sample is left to dry. Soil cores had been collected in steel rings, five centimeters tall and eight centimeters in diameter. The HYPROP system includes two tensiometers, inserted at depths of 1.25cm and 3.75cm, which record water potential as the core is allowed to evaporate through its top face. The mass flux of water leaving the core is monitored by conducting the experiment on top of a balance. After the tensiometers cavitate, software provided by the manufacturer fits an inverse model based on the Richards Equation to the time series data of tension and evaporative flux. To provide additional data points for the parameter estimation algorithm, we also estimated soil water potential in air-dry subsamples from each core using a WP4 Dewpoint Potentiometer (METER Group), which infers soil water potential by measuring the relative humidity of air in equilibrium with a sample.

Soil thermal properties used as input by ATS include thermal conductivity of saturated, thawed soil (λ_s, W m^{-1} K^{-1}), and thermal conductivity of dry soil material (λ_u, W m^{-1} K^{-1}). The thermal conductivity of soil at intermediate states of liquid or ice saturation is derived from these values and from the water retention curve, using equations described in Atchley et al. (2015). We estimated soil thermal conductivity using a KD2 Pro dual-needle heat pulse probe (METER Group), which was inserted into the top of the soil core during the evaporation experiments described in the previous paragraph. The KD2 estimates soil thermal properties at a depth of 1.25 cm below the surface, the same depth as the upper tensiometer of the HYPROP. We programmed the KD2 to estimate thermal properties every thirty minutes while the core evaporated, and used the record of tension from the upper tensiometer to match the time series of thermal conductivity estimates with volumetric wetness values. Following cavitation, we extrapolated these data points to 0% volumetric water content, to estimate the thermal conductivity of dry soil material.

Hydraulic and thermal properties from each core, estimated through these procedures, are presented in Table 2.1S.

Table 2.1S Estimated soil hydraulic and thermal properties from field samples.

Location	Depth (cm)	ϑ_s (m^3 m^{-3})	ϑ_r (m^3 m^{-3})	α (cm^{-1})	m (unitless)	λ_s (W m^{-1} K^{-1})	λ_u (W m^{-1} K^{-1})
Center	0	0.75	0.08	0.02	0.41	0.68	0.1
Center	12	0.62	0.06	0.02	0.49	1.34	0.2
Rim	0	0.74	0.00	0.04	0.26	0.68	0.12
Rim	8	0.68	0.02	0.02	0.33	0.84	0.15
Rim	19	0.76	0.03	0.02	0.32	0.79	0.15
Rim-Center boundary	0	0.66	0.00	0.09	0.32	0.52	0.15
Rim-Center boundary	12	0.65	0.04	0.02	0.41	0.64	0.12
Rim-Center boundary	19	0.66	0.07	0.02	0.46	0.94	0.2

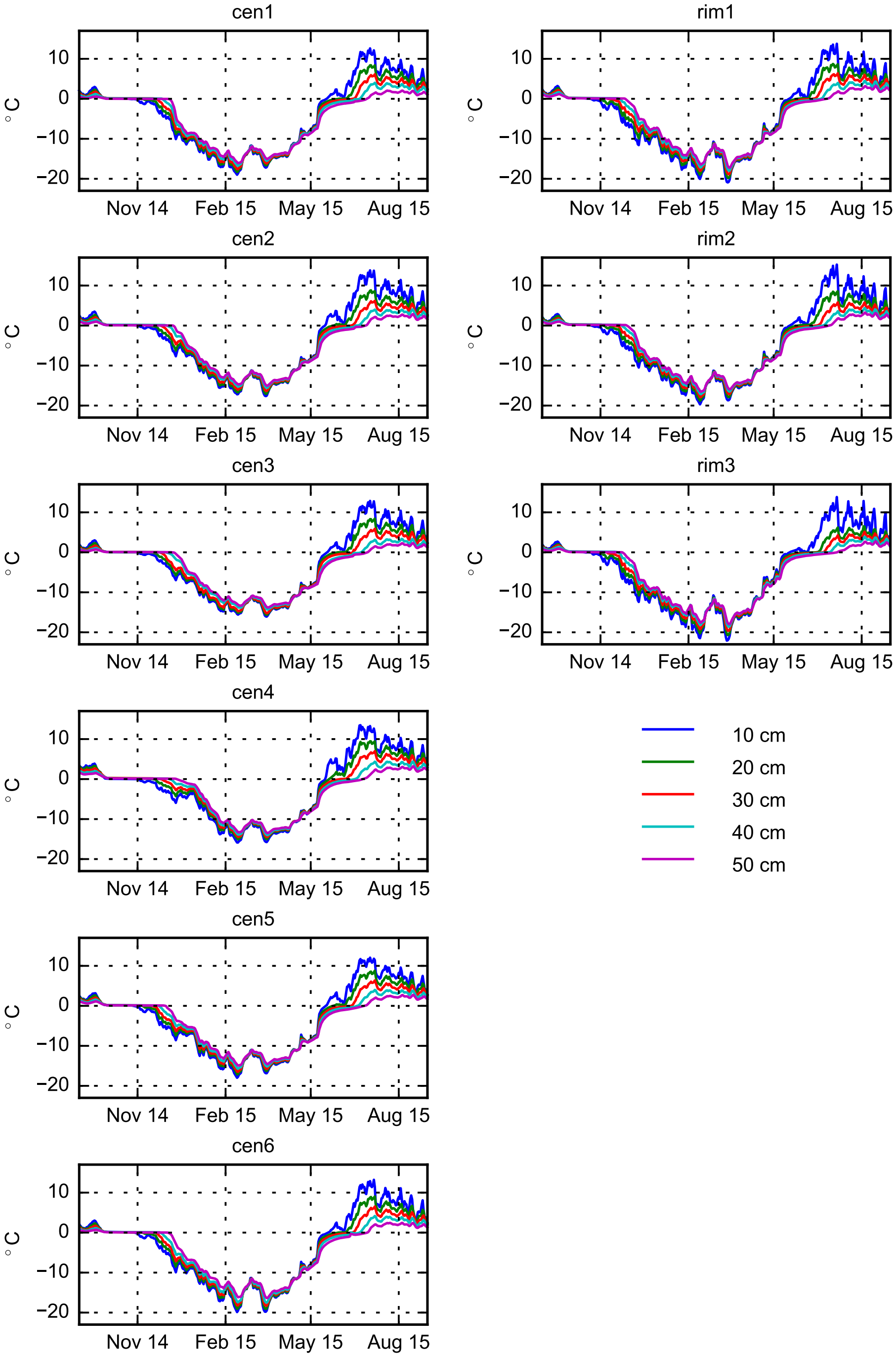

Figure 2.1S

Observed temperature at each sensor rod.

Chapter 3: Feedbacks between surface deformation and permafrost degradation in ice wedge polygons

ABSTRACT

In the past three decades, an abrupt, pan-Arctic acceleration of ice wedge thaw has transformed tundra landscapes, spurring the formation of hummock-like features known as high-centered polygons (HCPs). This rapid geomorphic transition profoundly alters regional hydrology and surface emissions of CO_2 and CH_4. However, pathways of ice wedge degradation and the geomorphic stability of HCPs are incompletely understood, complicating efforts to project future landscape function. Here we use a modeling-based approach to quantify the influence of hydrologic and geomorphic feedbacks on ice wedge thaw, building on observations from prior field studies. We find that in most cases, re-stabilized ice wedges beneath HCPs are less vulnerable to climate extremes than non-degraded ice wedges, promoting landscape stability. However, ice wedges may fail to re-stabilize when overlying thaw-subsidence depressions approach several meters in width. In the latter scenario, ice wedge degradation is accelerated both by warm summers and mild, snowy winters.

3.1 Introduction

Permafrost-affected soils in the Arctic are thought to store more than 1,000 Pg of carbon, considerably more than the global atmosphere (Schuur et al., 2008; Hugelius et al., 2014). Projecting what portion of this stock will become mobilized as air temperatures increase is a major source of uncertainty in global climate models (Schuur et al*.,* 2015). On the tundra, a key factor that will influence carbon export from the subsurface is the thawing of ground ice bodies known as ice wedges, which reshapes microtopography in a way that improves soil aeration (Liljedahl et al., 2016), thereby altering rates of aerobic and anaerobic microbial respiration (Grosse et al., 2011; Lipson et al., 2012; Lara et al., 2014; Wainwright et al., 2015). The goal of this study is to assess the strength of hydrologic and geomorphic processes that influence ice wedge thaw, to improve projections of how this process will continue to shape land surface dynamics.

Occupying to 30% of the upper permafrost by volume (Kanevskiy et al., 2013), ice wedges resemble inverted triangles in cross section, measuring up to several meters wide at the upper face, and penetrating four to five meters below the active layer, or seasonally thawed zone. Their formation occurs over centuries through ice deposition into a network of near-surface cracks that open to relieve thermal contraction stresses in winter (Leffingwell, 1919; Lachenbruch, 1962). These cracks segment landscapes into discrete units, similar in shape to the centimeter-scale desiccation polygons of a dried lake bed, but measuring 5-30 m across. In many landscapes, historic ice wedge activity is reflected in low-centered polygon (LCP) microtopography, characterized by rims of soil up to half a meter in height at the polygon edges, displaced upward by stresses between growing ice wedges and the adjacent sediments (Mackay, 2000). In other settings, the presence of ice wedges may not be apparent at the surface (Mackay, 1990; 1995; Liljedahl et al., 2016). Both types of landscape are vulnerable to high-centered polygon (HCP) development when thaw penetrates the upper boundaries of the ice wedges, spurring localized subsidence (*i.e.*, thermokarst) in a network of inter-polygon troughs while soil in the polygon interiors erodes outward. HCP development tends to drive landscape-scale enhancement of soil drainage (Liljedahl et al., 2016), which is associated with several-fold increases in surface emissions of CO_2 and decreases in fluxes of CH_4 (Lipson et al., 2012; Lara et al., 2015; Wainwright et al., 2015).

In the past 30 years, increased air temperatures associated with climate change have spurred a marked acceleration in HCP development throughout the Arctic (Jorgenson et al., 2006; 2015; Raynolds et al., 2014; Liljedahl et al., 2016). Conceptual models indicate that, once the process is initiated, a key factor controlling its pace is water impoundment in subsiding troughs, which accelerates thaw in the underlying ice wedges by lowering albedo relative to bare tundra (Murton, 2009; Jorgenson et al., 2010). However, the magnitude of this positive feedback is controversial. On one hand, observations from North America suggest that changes to the surface energy balance in flooded troughs enhance thaw for ~10-15 years following the onset of subsidence; afterward, the ice wedge tends to be protected by fresh additions to an insulating mat of organic soil at the bottom of the trough, sourced either from the growth of aquatic vegetation (Jorgenson et al., 2006; 2015; Koch et al., 2018) or colluvium from eroding rims (Abolt et al., 2017). Supporting this model, field surveys indicate that recent thickening of the soil column in many thermokarst-affected troughs on the Alaska North Slope has augmented an "intermediate layer" of perennially frozen soil above the ice wedges by several decimeters—implying that some partially-thawed ice wedges have not only re-stabilized, but may be better buffered against future climate extremes than non-degraded ice wedges (Jorgenson et al., 2015; Kanevskiy et al., 2017). Nonetheless, it has long been speculated that, in other cases, positive feedbacks related to trough inundation might overpower this vegetative feedback, culminating in the submergence of polygonal terrain beneath kilometer-scale thaw lakes, as the growth and coalescence of trough ponds renders relatively deep deposits of ground ice vulnerable to thaw

(Cabot, 1947; Carson, 1968; Everett, 1980; Raynolds et al., 2014). These divergent trajectories introduce major uncertainty into projections of Arctic influence in global climate change, as variability in the spatial distribution of lakes, saturated soil, and relatively drained soil at the surface exerts a primary control on landscape-scale exchanges of heat and carbon between the ground and atmosphere.

In this study, we develop a framework for quantitatively estimating the strength of geomorphic and hydrologic feedbacks on ice wedge degradation, to improve projections of landscape evolution on the tundra. Our experimental design is to estimate a variable we term potential active layer thickness in the trough ($\mathrm{pALT_{tro}}$), or the thickness of trough-bottom soil necessary to prevent ice wedge degradation, in a diverse set of ice wedge polygons subject to identical meteorological forcing. By comparing $\mathrm{pALT_{tro}}$ among polygons representing early and late stages of thermokarst, we estimate the scale of soil accumulation necessary to offset positive feedbacks on thaw, then compare the results with rates of observed soil accumulation derived from contemporary field surveys. Subsequently, to estimate the severity of summer air temperatures necessary to eliminate intermediate layers of variable thickness, we calculate increases to $\mathrm{pALT_{tro}}$ as the polygons are subjected to meteorological forcing representing a historically warm summer and a still warmer future. Interpreting the results of our simulations in the context of existing field data, we offer an assessment of the potential for positive or negative feedbacks to govern ice wedge degradation, and an appraisal of the durability of re-stabilized ice wedges in an increasingly warm climate.

3.2 Methods

3.2.1 Model description

Our simulations were constructed in version 0.86 of Amanzi-ATS (https://github.com/amanzi/ats), an ecohydrology code developed specifically for application to permafrost environments. At its core, Amanzi-ATS uses a flexible multiphysics framework to solve for conservation of energy and water mass at the surface, in the subsurface, and in the snowpack (Coon et al., 2016). At the surface, meteorological data is used to force an implicit solution to the surface energy balance (Atchley et al., 2015), as the code accounts for overland water flow and redistribution of snow across microtopography (Painter et al., 2016). The albedos of water, snow, and bare tundra are treated as adjustable constants, and snow albedo decreases as the snowpack ages. When only shallow depths of water (<10 cm) or snow (<2 cm) are present at the surface, albedo is assigned an intermediate value between the tundra and the overlying material. In the subsurface, the code solves a variant of the Richards Equation, simulating variably saturated flow while accounting for cryosuction and density variations between liquid water and ice. At the spatial scale of centimeters, Amanzi-ATS has been shown to accurately reproduce laboratory observations of soil moisture redistribution and phase change in freezing, variably saturated soils (Karra et al., 2014). At the field scale, Amanzi-ATS has been extensively applied and validated in diverse permafrost settings (Harp et al., 2016; Atchley et al., 2016; Sjoberg et al., 2016; Schuh et al., 2017; Jafarov et al., 2018), including polygonal terrain (Atchley et al., 2015; Abolt et al., 2018; Jan et al., 2018). Overviews of the partial differential equations solved by the code are available in Atchley et al. (2015) and Painter et al.

(2016), and in the appendix to this dissertation.

3.2.2 Mesh design, boundary conditions, and initial condition

To accurately represent energy fluxes, our meshes were designed using a pie-wedge shape, representative of an idealized, radially symmetric polygon (Figure 3.1S). In each mesh, mineral soil extending to a bottom boundary at 50 m depth was overlain by a 30 cm mantle of peat-rich soil. Soil hydraulic and thermal parameters were identical to those used by Abolt et al. (2018), which were estimated through laboratory analysis of core samples from an LCP near Prudhoe Bay, Alaska (Table 2.1S). Notably, no mesh cells were assigned as ice wedges; through this omission, we aimed to avoid the physical complexities of simulating ice wedge thaw and ground subsidence. Instead, during summer months we extracted from each simulation the maximum depth of the 0°C isotherm in the center of the trough, and interpreted this number as potential active layer thickness ($\mathrm{pALT}_{\mathrm{tro}}$), or the approximate depth of trough-bottom soil necessary to prevent ice wedge degradation. Hydrologic boundary conditions imposed on each mesh were Neumann zero-flux at all lateral boundaries, except in the trough, where either a zero-flux or a seepage face boundary condition was applied to control water accumulation (Figure 3.1S). The bottom boundary in each simulation was set at a constant -6°C, characteristic of regional borehole observations (Romanovsky et al., 2009), and the initial condition in every simulation was an isothermal column of frozen soil, saturated with ice to within 5 cm of the surface. Prior to executing our sensitivity analysis, this configuration was validated in a simulation designed to reproduce the ground thermal regime at the field site of Abolt et al. (2018) (Text 3.1S, Figure 3.2S). Discussion of restrictive assumptions associated with our use of pie-wedge-shaped meshes and omission of ice wedge cells is included in the supplemental information (Text 3.2S).

3.2.3 Experimental design

Each of our simulations was forced with meteorological data representing 20 summers and 19 winters, using a single pie-wedge mesh subject to a unique combination of microtopographic and hydrologic conditions. By symmetry, each pie-wedge mesh was interpreted as representing a landscape of similarly shaped polygons (Figure 3.3S). In the first 19 years, to isolate the effects of microtopography and trough drainage on $\mathrm{pALT_{tro}}$, simulations were brought asymptotically near cyclical-steady state through repeated forcing with a “baseline” year representing mean weather conditions at a site on the Alaska North Slope from 2000-2015 (Text 3.3S). The thaw degree-day (TDD) index (*i.e.*, the time integral of temperatures above 0°C) of this baseline year was 873 °C d. Subsequently, to determine how microtopography and hydrology influence the potential for active layer deepening in warm years, each cyclically forced simulation was restarted on January 1st four separate times, each instance using nine months of data (January through the end of September) representing either an historically warm year or a still warmer future. Weather data from 1989 (TDD = 1188°C d) were used to represent a historically warm and wet year, known to have triggered extensive ice wedge degradation throughout Arctic North America, while synthetic weather data was used to represent hypothetical summers in which TDD was equal to 1300, 1400, or 1500 °C d (Text 3.2S).

Our sensitivity analysis comprised two subsets of simulations, designed to explore the influence on $\mathrm{pALT_{tro}}$ of rim height, trough depth, trough width, and trough drainage. In the first subset of simulations, we applied Neumann zero-flux boundary conditions in the trough, systematically scanning through trough depths (relative to the center) of 5, 25, 45, 65, and 85 cm; trough widths (at the bottom of the trough) of 1 m and 3 m; and rim morphologies that were 30 or 10 cm taller than the center of the polygon, or nearly absent, representing HCP conditions. In simulations with sufficiently deep troughs, the lack of lateral surface drainage in this treatment favored the development of thermokarst pools. In a second subset of simulations, we imposed a seepage face boundary condition that limited surface water accumulation in the trough to 5 cm, re-using all meshes with a trough depth of 65-85 cm. This treatment was designed to represent landscapes in late stages of thermokarst, which sometimes experience an abrupt enhancement of drainage due to increased trough connectivity as the polygon boundaries subside (*e.g.*, Liljedahl et al., 2016; Kanevskiy et al., 2017).

Aside from estimates of $\mathrm{pALT_{tro}}$, variables extracted from each simulation included time series of subsurface temperature (at all cells), snow and surface water depth (at all surface cells), the surface-subsurface energy flux in the trough, and the laterally-oriented subsurface energy flux between the trough the polygon interior (boundary indicated in Figure 3.1S).

3.3 Results and Discussion

3.3.1 Overall scale of feedbacks on active layer development in the trough

At cyclical steady state, $\mathrm{pALT_{tro}}$ varied among simulations from 78-130 cm (Figures 3.1a, 3.1b), results that match recent observations of ALT on the tundra ~40 km south of

Prudhoe Bay (Abolt et al., 2018). The results indicate that, with other factors held constant, $\mathrm{pALT_{tro}}$ tends to increase with trough depth so long as the trough is poorly drained. This pattern affirms conceptual models of a positive feedback on ice wedge degradation associated with trough inundation, because higher estimates of $\mathrm{pALT_{tro}}$ imply a greater probability that thaw will penetrate the sediments atop an ice wedge. We judge the strength of this positive feedback by comparing the difference in $\mathrm{pALT_{tro}}$ between early and late stages of thermokarst with observed rates of soil accumulation at the bottom of a subsiding trough. The latter have been quantified through analysis of soil cores extracted near Prudhoe Bay, Utqiaġvik, and the lower Colville River basin in northern Alaska, where it was determined that 15-30 cm of peat or more commonly accumulates over timespans of 10-30 years following the onset of subsidence (Jorgenson et al., 2006; 2015; Kanevskiy et al., 2017).

In most cases, we find that soil accumulation over timescales of decades is more than sufficient to neutralize the positive feedback on ice wedge thaw caused by surface water, because the boost to $\mathrm{pALT_{tro}}$ associated with thermokarst is only a fraction of observed peat accumulation. Among simulations with narrow troughs, for example, the difference in $\mathrm{pALT_{tro}}$ between two endmembers—an LCP with a 5 cm deep trough, and an HCP with a flooded, 85 cm deep trough—is only 7 cm, and this difference disappears altogether if the trough becomes well drained (Figure 3.1a). Should a thermokarst pool widen over time, but eventually become well-drained, there will likewise be no effective difference in $\mathrm{pALT_{tro}}$ between LCP and HCP (Figure 3.1b). In these scenarios, we infer that decimeter-scale soil accumulation at the bottom of a trough will not only stabilize the ice wedge, but enlarge the intermediate layer above it relative to its pre-thermokarst state (Figure 3.2). Notably, such a trajectory matches observations of recent thickening in the intermediate layer beneath thermokarst-affected troughs in northern Alaska, which on average measured ~30 cm (Jorgenson et al., 2015; Kanevskiy et al., 2017). Given the current thermal state of the permafrost, we project that a buffer of this thickness might withstand a summer in which TDD approaches 1500 °C d—twice as extreme a departure from mean 2000-2015 conditions as the historically warm summer of 1989 (Figures 3.1c, 3.1d). This finding suggests that, compared with terrain unaffected by thermokarst, most HCPs are relatively stable; therefore, accounting for the persistence of HCPs will be essential to projecting tundra hydrologic processes and carbon fluxes at large spatial and temporal scales.

Nonetheless, our model predicts that in limited cases, the destabilizing effects of inundation on the trough thermal regime may approach or outweigh the stabilizing influence of soil accumulation. This scenario is most feasible when troughs are wide, which magnifies the perturbation to active layer dynamics associated with surface water (discussed in the next section). We find that, when trough width increases from 1 to 3 m, the difference in $pALT_{tro}$ between non-degraded and deeply flooded troughs increases to ~30-50 cm in average years (Figure 3.1b)—suggesting that in some instances, observed rates of peat accumulation may just offset positive feedbacks on thaw within a couple decades, while in others, ice wedge thaw may progress for longer timespans, even in the absence of above-average air temperatures. We predict that in the coming decades, instances of the latter trajectory culminating in the formation of new thermokarst lakes will be rare, because: 1) trough enlargement tends to improve trough connectivity, which often enhances drainage, eliminating thermokarst pools (Liljedahl et al., 2016; Kanevskiy et al., 2017), and 2) in most cases, the capacity for a growing thermokarst pool to envelop ice wedge polygon centers will be precluded by the limited extent to which ground ice exceeds soil porosity outside of the trough, which constrains the potential for ground subsidence (Jorgenson and Shur, 2007). However, in instances characterized by poor landscape-scale drainage and large volumes of excess ground ice in the upper permafrost, we predict that positive feedbacks associated with the formation of wide trough ponds will be sufficient to sustain ground subsidence over timescales of several decades or longer.

3.3.2 Physical drivers of variability in the trough thermal regime

The influence of surface water on $pALT_{tro}$ is tied to a thermal offset between air temperature and trough-bottom temperature that increases with the scale of inundation. Fundamentally, the thermal offset exists because heat extraction from a flooded trough toward the atmosphere in winter is less efficient than the reverse transfer of energy in summer; this disparity grows as trough ponds increase in size. In winter, the offset is magnified by the accumulation of an insulating layer of snow atop a pond once its surface freezes, impeding release of the large reservoir of energy stored in the liquid water beneath (Atchley et al., 2016). This mechanism prolongs freeze-up of a thermokarst pool to an extent that scales upward with the depth of water and the thickness of snow. Thus, although each of our simulated ponds freezes to the bottom by the end of winter, relatively warm ground temperatures persist through the season beneath the deepest examples (Figure 3.3). These conditions, in turn, jump-start thawing processes in early summer, when the impedance to the sensible heat flux caused by snow is eliminated, and the relatively low albedo of ponded water drives efficient absorption of shortwave radiation. We found that this jump-start becomes especially pronounced in instances where the pore space within pockets of the active layer beneath a freezing pond fail to freeze completely in winter (*e.g.*, Figure 3.3f), spurring a talik-like effect that increases pALT$_{\text{tro}}$ considerably.

Although the low albedo of water contributes to the thermal offset, we found that the effect varies negligibly within the range of albedos reported in the literature. This conclusion was supported by a supplementary set of simulations, in which we magnified the albedo difference between bare tundra and water several times relative to the default values assumed by Amanzi-ATS, using bounds observed by Gamon et al. (2012) in Alberta (Text 3.4S). Using the alternative parametrization, we observed a difference in net radiation between flooded and bare ground that replicated observations by Langer et al. (2011a) and Jorgenson et al. (2015). However, pALT$_{\text{tro}}$ remained nearly unchanged, as the boost to net radiation was largely matched by increases to evaporation and decreases to downward sensible heat transfer (Figure 3.4S).

We attribute the intensification of the effects of surface water beneath wide troughs to the diminished influence of a laterally-oriented, conductive heat flux from the flooded trough toward the polygon interior; similar outward-oriented energy fluxes from small water bodies on the tundra have been reported by Langer et al. (2011b, 2016). The lateral energy flux is most significant in winter, when freeze-up in the sediments beneath an inundated trough is delayed by the slow phase change of the overlying surface water. During this time, because temperature at the upper boundary of the active layer (*i.e.,* the soil-water interface) cannot fall below freezing, up to 65% of cooling beneath the trough occurs via heat conduction through the adjacent rims of an LCP or through the center of an HCP (Figure 3.5S). However, as trough width increases, this mechanism of heat extraction at the trough periphery becomes a less efficient means of cooling. As a result, a greater fraction of the active layer in wide troughs remains partially unfrozen in winter, boosting the talik-like effect on $pALT_{tro}$.

The effects of rim height on $pALT_{tro}$ are complex, stemming again from the influence of lateral energy fluxes on the trough thermal regime. On one hand, due to relatively thin snow cover in winter, tall rims are effective outlets of heat for the sediments beneath flooded troughs; therefore, in cases when the trough is inundated, increased rim height weakens the talik-like effect and depresses $pALT_{tro}$ in LCPs (Figures 3.1a, 3.1b). On the other hand, the *absence* of rims in some HCPs may also cause a reduction in $pALT_{tro}$ relative to LCPs (Figure 3.1a). This latter trend is only significant in narrow troughs, and is related to a seasonal reversal of the laterally-oriented conductive heat flux at the trough boundary. The reversal arises during summer, when the rims warm more efficiently than the remainder of an LCP, as they are the first zone exposed to the atmosphere by snow ablation and remain relatively well-drained throughout the season, which reduces soil heat capacity and evaporative cooling. The resulting temperature gradients tend drive a lateral, conductive heat flux from the rims *toward* the trough. Although this seasonal flux is dwarfed by the outward transfer of energy from a flooded trough in winter, it accounts for up to 15% of total annual energy inputs into the trough subsurface when trough width is limited to 1 m (Figure 3.6S); thus, the loss of rims in polygons with narrow troughs may translate to a 5-10 cm decrease in $pALT_{tro}$ (Figure 3.1a). Just as in winter, however, this conductive heat flux at the periphery of a flooded trough becomes less significant to the thermal regime as trough width approaches 3 m. In the latter case, the talik-like effect is strongest and simulated seasonal thaw is deepest in the center of the trough (Figure 3.3d), in line with field observations.

3.3.3 Sensitivity of potential active layer thickness to warm and wet summers

Among simulations of polygons with narrow troughs, the deepening of $pALT_{tro}$ during warm summers is nearly uniform (Figure 3.1c). Using meteorological data from 1989 (TDD = 1188 °C d), $pALT_{tro}$ increases an average of ~20 cm from baseline conditions (TDD = 873 °C d); this indicates a summer severe enough to trigger thermokarst by eliminating the intermediate layer of frozen soil above a typical non-degraded ice wedge, which averages ~10 cm or less in recent field surveys from northern Alaska (Jorgenson et al., 2015; Kanevskiy et al., 2017). In a hypothetical summer approaching 1500 °C d (a mean departure of ~5 °C from mean 2000-2015 conditions), increases to $pALT_{tro}$ are nearly 30 cm, approaching the mean thickness of intermediate layers observed atop degraded but re-stabilized ice wedges in the same surveys.

When troughs are wide, the response of $pALT_{tro}$ to severe summers is more complex (Figure 3.1d). Specifically, we found that when wide troughs are flooded with more than 45 cm of water, increases to $pALT_{tro}$ are modest in most cases, and negligible, or even negative, in others. This surprising result reflects snowfall during the first four months of 1989 (as well as the hypothetical warmer years, which use the same precipitation data), which is below average in our forcing dataset. This trend results in a diminished snowpack, which enhances freeze-back in the active layer, weakening the talik-like effect that typically generates deep active layers beneath wide thermokarst pools (Figure 3.7S). The heightened sensitivity of $pALT_{tro}$ to winter conditions in wide, flooded troughs implies that, to project the trajectories of thermokarst pools at the threshold of sustained growth, it is important to consider not only summer air temperatures, but also variability in winter air temperature and snowpack. Meteorological records from Kuparuk, on the Alaska North Slope, indicate that recent trends in the latter two variables are at least as significant as the former (Menne et al., 2012) (Figure 3.8S). This suggests that, although the onset of recent thermokarst is attributable to exceptionally warm summers such as 1989, the growth of trough ponds in the past 30 years may also have been accelerated by warmer, snowier winters.

3.4 Summary

In most cases, ice wedge thaw in vegetated tundra landscapes is self-arresting, as the stabilizing influence of peat accumulation in subsiding troughs more than compensates for positive feedbacks associated with water impoundment. This indicates that HCPs are generally more stable than LCPs, and that understanding the consequences of HCP persistence at large spatial and temporal scales will be key to projecting future hydrology and carbon fluxes on the tundra. The capacity for positive feedbacks to drive ice wedge degradation for time periods longer than two decades increases when trough width approaches several meters. Instances of trough ponds coalescing into larger thermokarst lakes will probably be rare, but the expansion of already wide pools can be accelerated by mild and snowy winters, in addition to warm summers.

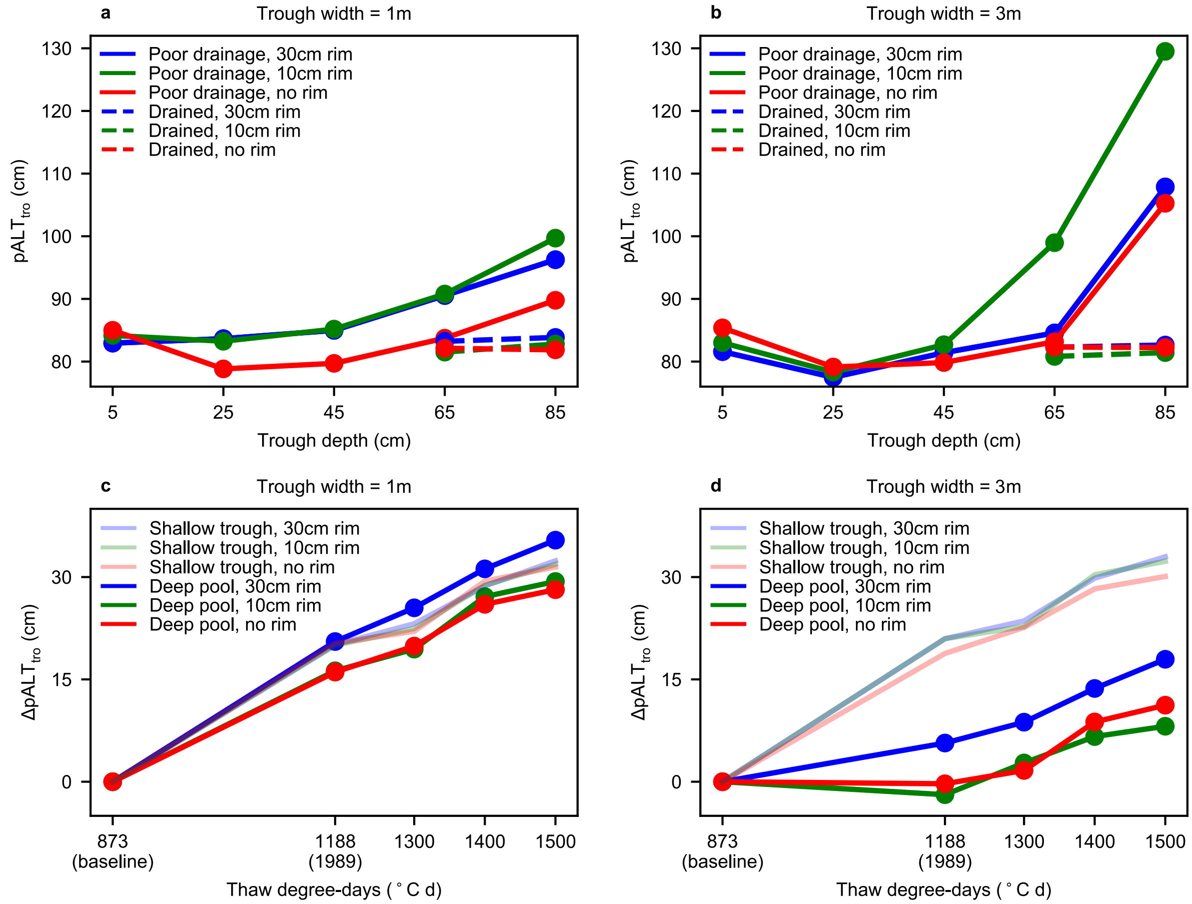

Figure 3.1

Estimates of pALT_{tro} at cyclical steady state in troughs with widths of 1 m (**a**) and 3 m (**b**). Increases to baseline pALT_{tro} during warm summers, from select simulations of troughs that are 1 m wide (**c**) and 3 m wide (**d**). 'Shallow trough' refers to a trough 5 cm deep relative to the polygon center, and 'deep pool' refers to a trough 85 cm deep with poor drainage.

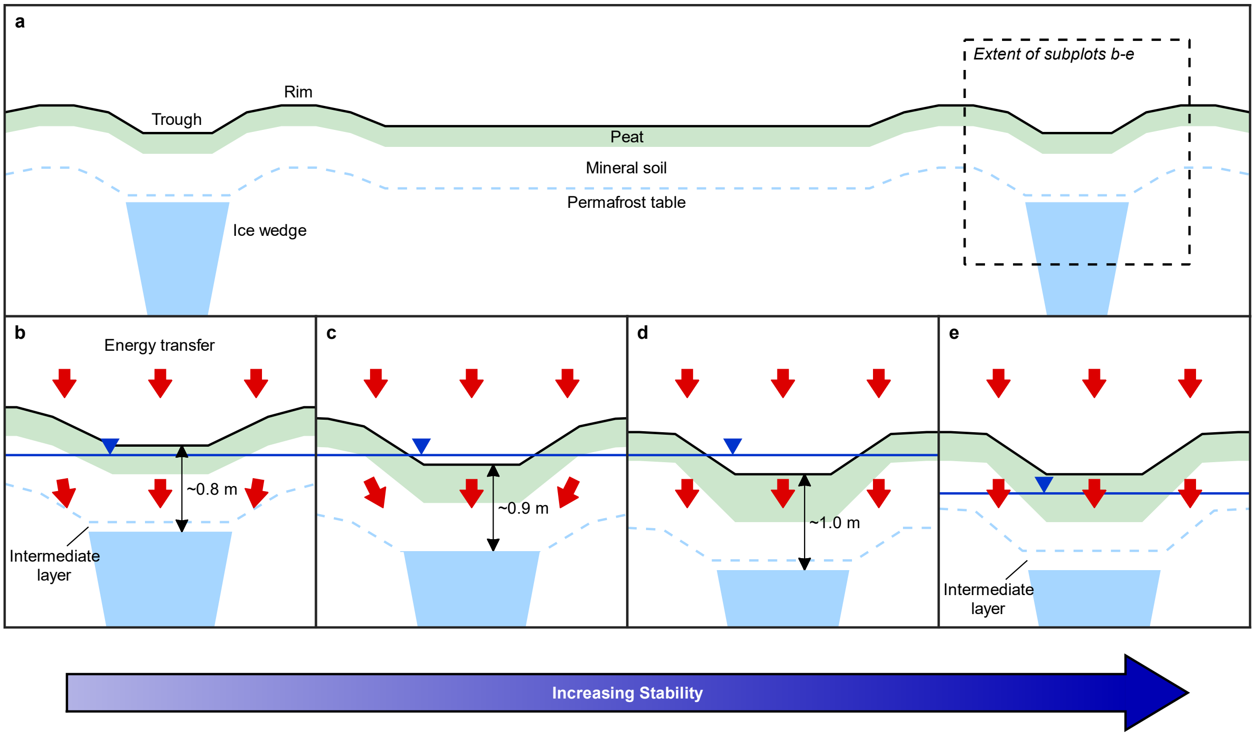

Figure 3.2

Schematic of a potential trajectory for thermokarst beneath an initially low-centered polygon (**a**). Ice wedge degradation initiates in a warm summer, when thaw penetrates the intermediate layer of frozen soil that normally separates the ice wedge from the active layer (**b**). Lateral heat conduction from the rims contribute modestly to the vulnerability of the ice wedge over the next several summers (**c**), but these thermal inputs disappear as rim size reduces. Simultaneously, soil accumulation in the trough restores the intermediate layer (**d**). Occasionally, at advanced stages of thermokarst, an abrupt enhancement of landscape-scale drainage eliminates surface water, further thickening the intermediate layer (**e**).

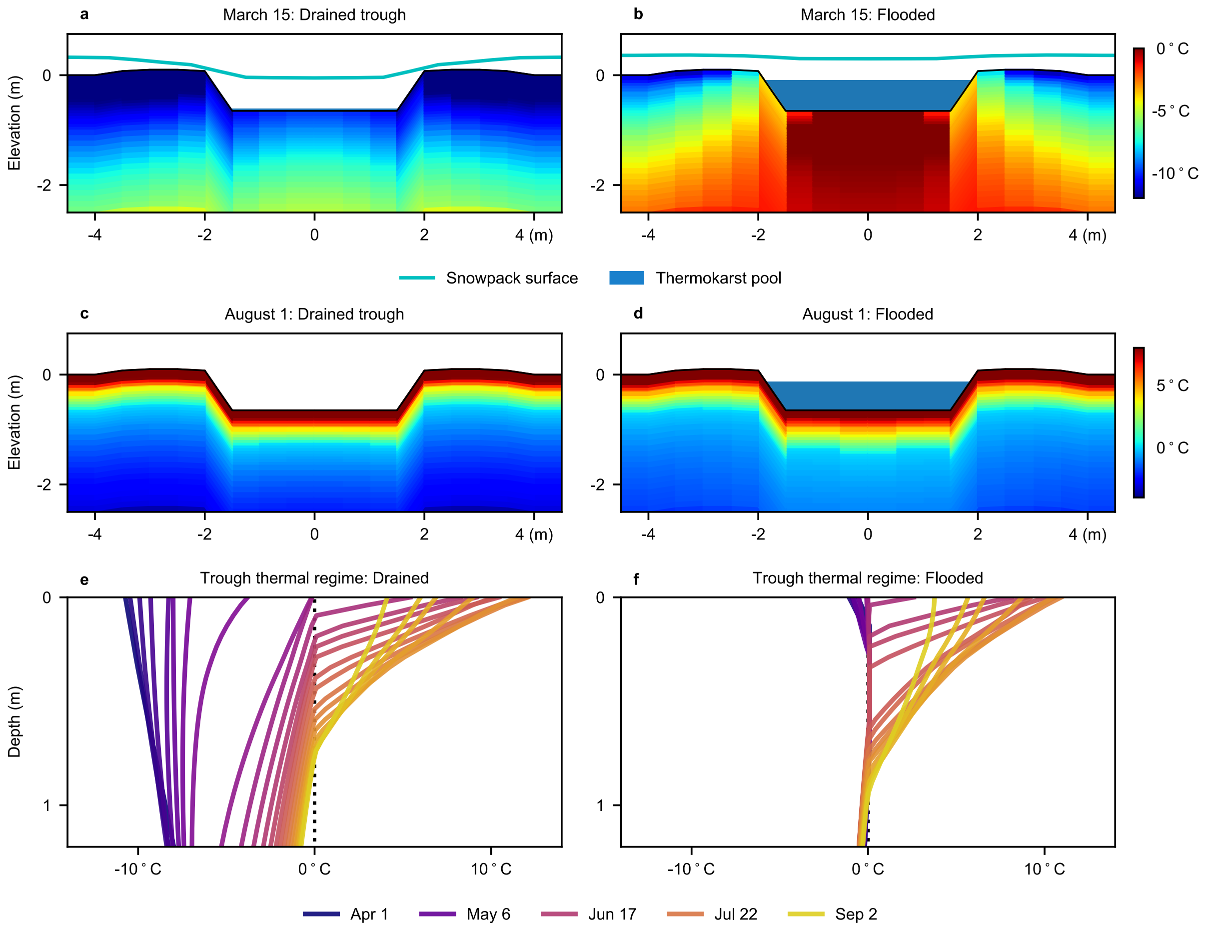

Figure 3.3

Snapshots of ground temperature, surface water, and snow pack at cyclical steady state, beneath a well-drained and an inundated trough in late winter (**a**, **b**) and late summer (**c**, **d**). Profiles of the trough thermal regime every week during the thaw season, beneath the well-drained (**e**) and inundated troughs (**f**).

REFERENCES

Abolt CJ, Young MH, Caldwell TG. 2017. Numerical modelling of ice-wedge polygon geomorphic transition. *Permafrost and Periglacial Processes* **28**: 347–355.

Abolt CJ, Young MH, Atchley AL, Harp DR. 2018. Microtopographic control on the ground thermal regime in ice wedge polygons. *The Cryosphere* **12**: 1957-1968.

Atchley AL, Painter SL, et al. 2015. Using field observations to inform thermal hydrology models of permafrost dynamics with ATS (v0.83). *Geoscientific Model Development* **8**: 2701–2722.

Atchley AL, Coon ET, et al. 2016. Influences and interactions of inundation, peat, and snow on active layer thickness. *Geophysical Research Letters* 43: GL068550.

Cabot EC. 1947. The northern Alaskan coastal plain interpreted from aerial photographs. *Geographical Review* **37**: 639-648.

Carson CE. 1968. Radiocarbon dating of lacustrine strands in Arctic Alaska. *Arctic* **21**: 12-26.

Coon ET, Moulton D, Painter SL. 2016. Managing complexity in simulations of land surface and near-surface processes. *Environmental Modelling & Software* **78**: 134–149.

Everett KR. 1980. Landforms. In: DA Walker, KR Everett, PJ Webber, J Brown (Eds.). *Geobotanical Atlas of the Prudhoe Bay Region, Alaska*, pp. 14-19. Hanover, NH: US Army Cold Regions Research and Engineering Laboratory.

Fortier D, Allard M, Shur Y. 2007. Observation of rapid drainage system development by thermal erosion of ice wedges on Bylot Island, Canadian Arctic Archipelago. *Permafrost and Periglacial Processes* **18**: 229-243.

Gamon JA, Kershaw GP, et al. 2012. Microtopographic patterns in an arctic baydjarakh field: do fine-grain patterns enforce landscape stability? *Environmental Research Letters* **7**: 015502.

Grosse G, Harden J., et al. 2011. Vulnerability of high-latitude soil organic carbon in North America to disturbance. *Journal of Geophysical Research: Biogeosciences* ***116***: G00K06.

Harp DR, Atchley AL, et al. 2016. Effect of soil property uncertainties on permafrost thaw projections: a calibration-constrained analysis. *The Cryosphere* **10**: 341–358.

Hugelius G, Strauss J, et al. 2014. Estimated stocks of circumpolar permafrost carbon with quantified uncertainty ranges and identified data gaps. *Biogeosciences* **11**: 6573-6593.

Jan A, Coon ET, et al. 2018. An intermediate-scale model for thermal hydrology in low-relief permafrost-affected landscapes. *Computational Geosciences* **22**: 163-177.

Jorgenson MT, Shur YL, Pullman ER. 2006. Abrupt increase in permafrost degradation in Arctic Alaska. *Geophysical Research Letters* **33**: GL024960.

Jorgenson MT, Shur Y. 2007. Evolution of lakes and basins in northern Alaska and discussion of the thaw lake cycle. *Journal of Geophysical Research* **112**: JF000531.

Jorgenson MT, Romanovsky V., et al. 2010. Resilience and vulnerability of permafrost to climate change. *Canadian Journal of Forest Research* **40**: 1219-1236.

Jorgenson MT, Kanevskiy M, et al. 2015. Role of ground ice dynamics and ecological feedbacks in recent ice wedge degradation and stabilization. *Journal of Geophysical Research: Earth Surface* **120**: 2280–2297.

Kanevskiy M, Shur Y, et al. 2013. Ground ice in the upper permafrost of the Beaufort Sea coast of Alaska. *Cold Regions Science and Technology* **85**: 56-70.

Kanevskiy M, Shur Y, Jorgenson MT, et al. 2017. Degradation and stabilization of ice wedges: Implication for assessing risk of thermokarst in northern Alaska. *Geomorphology* **297**: 20-42.

Karra S, Painter SL, Lichtner PC. (2014). Three-phase numerical model for subsurface hydrology in permafrost-affected regions (PFLOTRAN-ICE v1.0). *The Cryosphere* **8**: 1935-1950.

Koch JC, Jorgenson MT, et al. (2018). Ice wedge degradation and stabilization impact water budgets and nutrient cycling in Arctic trough ponds. *Journal of Geophysical Research: Biogeosciences* **123**: 2604-2616.

Lachenbruch AH. 1962. Mechanics of thermal contraction cracks and ice-wedge polygons in permafrost. Geological Society of America Special Paper 70.

Langer M, Westermann S, et al. 2011a. The surface energy balance of a polygonal tundra site in northern Siberia—Part 1: Spring to fall. *The Cryosphere* **5**: 151-171.

Langer M, Westermann S, et al. 2011b. The surface energy balance of a polygonal tundra site in northern Siberia—Part 2: Winter. *The Cryosphere* **5**: 509-524.

Langer M, Westermann S, et al. 2016. Rapid degradation of permafrost underneath waterbodies in tundra landscapes—Toward a representation of thermokarst in land surface models. *Journal of Geophysical Research: Earth Surface* **121**: 2446-2470.

Lara MJ, McGuire DA, Euskirchen ES, et al. 2015. Polygonal tundra geomorphological change in response to warming alters future CO_2 and CH_4 flux on the Barrow Peninsula. *Global Change Biology* **21**: 1634-1651.

Leffingwell EK. 1915. Ground-ice wedges, the dominant form of ground-ice on the north coast of Alaska. *Journal of Geology* **23**: 635-654.

Liljedahl AK, Boike J, Daanen RP, et al. 2016. Pan-Arctic ice wedge degradation in warming permafrost and its influence on tundra hydrology. *Nature Geoscience* **9**, 312-318.

Lipson DA, Zona D. 2012. Water-table height and microtopography control biogeochemical cycling in an Arctic coastal tundra ecosystem. *Biogeosciences* **9**: 577-591.

Mackay JR. 1990. Some observations on the growth and deformation of epigenetic, syngenetic, and anti-syngenetic ice wedges. *Permafrost and Periglacial Processes* **1**: 15-29.

Mackay JR. 1995. Ice wedges on hillslopes and landform evolution in the late Quaternary, western Arctic coast, Canada. *Canadian Journal of Earth Science* **32**: 1093-1105.

Mackay JR. 2000. Thermally induced movements in ice-wedge polygons, western Arctic coast: A long-term study. *Géographie Physique et Quarternaire* **54**: 41-68.

Menne MJ, Durre I., et al. 2012. An overview of the Global Historical Climatology Network-Daily database. *Journal of Atmospheric and Oceanic Technology* **29**: 897-910.

Murton JB. 2009. Global warming and thermokarst. In: R Margesin (Ed.), *Permafrost Soils,* pp. 185-203. Berlin: Springer.

Painter SL, Coon ET. 2016. Integrated surface/subsurface permafrost thermal hydrology: Model formulation and proof-of-concept simulations. *Water Resources Research* **52**: 6062-6077.

Raynolds MK, Walker DA, et al. 2014. Cumulative geoecological effects of 62 years of infrastructure and climate change in ice-rich permafrost landscapes, Prudhoe Bay Oilfield, Canada. *Global Change Biology* **20**: 1211-1224.

Rodell M, Houser PR, et al. 2004. The Global Land Data Assimilation System. *Bulletin of the American Meteorological Society* **85**: 381–394.

Romanovsky V, Kholodov A, et al. 2009. Network of Permafrost Observatories in North America: Temperature in deep boreholes. Arctic Data Center.

Schuh C, Frampton A, Christiansen HH. 2017. Soil moisture redistribution and its effect on inter-annual active layer temperature and thickness variations in a dry loess terrace in Adventdalen, Svalbard. *The Cryosphere* **11**: 635-651.

Schuur EAG, Bockheim J, et al. 2008. Vulnerability of permafrost carbon to climate change: Implications for the global carbon cycle. *BioScience* **58**: 701-714.

Schuur EAG, McGuire AD, et al. 2015. Climate change and the permafrost carbon feedback. *Nature* **520**: 171-179.

Sjoberg Y, Coon ET, et al. 2016. Thermal effects of groundwater flow through subarctic fens: A case study based on field observations and numerical modeling. *Water Resources Research* **52**: 1591-1606.

Wainwright HM, Dafflon B, Smith LJ, et al. 2015. Identifying multiscale zonation and assessing the relative importance of polygon geomorphology on carbon fluxes in an Arctic tundra ecosystem. *Journal of Geophysical Research: Biogeosciences* **120**, 788-808.

Wales NA, Gomez-Velez JD, Newman BD, et al. 2019. Understanding the relative importance of vertical and horizontal flow in ice-wedge polygons. *Hydrology and Earth System Sciences Discussions*. doi:10.5194/hess-2019-25.

Text 3.1S Model validation

Physical parameters (hydraulic and thermal) for soil and snow were previously validated in Amanzi-ATS simulations constructed to emulate the ground thermal regime in an LCP near Prudhoe Bay, Alaska, where ground temperature had been observed at several depths beneath the center and rims from 2014-2015 (Abolt et al., 2018). Meteorological data from 2014-2015 had been used to force simulations, allowing for a four-year spin-up. To assure that the pie wedge meshes used in the present study allowed for reasonable simulations of the ground thermal regime, we repeated the prior 2010-2015 simulation substituting a wedge-shaped mesh with a rim height of 20 cm and a trough depth of 5 cm relative to the polygon center, approximating the LCP at the field site. A comparison of simulated temperature in the center and the rim with the observational record reveals a close match, with an RMSE of ~1.2°C (Figure 3.2S)

Text 3.2S Restrictive assumptions associated with our mesh design

The computational intensity of the simulations conducted in this study was greatly reduced by constraining calculations to pie-wedge-shaped spatial domains (Fig. 3.1S). Each pie-wedge simulation was intended to represent the ground hydrologic and thermal regimes throughout an entire polygon, by symmetry (Fig. 3.3S). Nonetheless, this approach relies on a number of restrictive assumptions that must be considered alongside the results.

One primary assumption is that terrestrial hydrologic processes operating at spatial scales larger than a single ice wedge polygon have an insignificant impact on active layer thickness in the trough. This assumption is not always valid. For example, field observations indicate that, on occasion, catchment-scale runoff may channelize within interconnected thermokarst troughs and persist throughout the summer, driving severe (*i.e.*, meter-scale) ice wedge degradation over time scales of months, due to advective heat transfer associated with the streamflow (*e.g.*, Fortier et al., 2007). Nonetheless, these instances appear to be rare in terms of total area affected; several recent landscape-scale surveys of aerial photography and satellite imagery indicate that, after the early-summer snow melt, the vast majority of surface water in polygonal terrain occurs within discontinuous thermokarst pools, resembling the ponds simulated in this study (Jorgenson et al., 2006; 2015; Raynolds et al., 2014; Liljedahl et al., 2016; Kanevskiy et al., 2017). Liljedahl et al. (2016) report that, during the period of snow melt, runoff does commonly result in channelized flow through the troughs of HCP landscapes; however, in most cases, this streamflow is highly ephemeral, limited to a time of year in which liquid water temperature is near-freezing, resulting in minimal advective heat transfer toward the ice wedges. Field observations indicate that groundwater exchange among adjacent polygons also tends to be limited; in tracer studies near Utqiaġvik, Alaska, for example, the majority of dye injected into the centers of an LCP and an HCP remained within the polygon boundaries after two complete thaw seasons (Wales et al., 2019). These studies as a whole imply that our use of pie-wedge meshes is justified, as hydrologic exchange among polygons is probably small in most cases, resulting in minimal impact on the ground thermal regime.

Another restrictive assumption associated with our use of pie-wedge meshes is that microtopographic slope and aspect have negligible impacts on the ground thermal regime. This assumption is necessary, as a hypothetical hexagonal polygon would be comprised of pie wedges facing six different directions (Fig. 3.3S), and Amanzi-ATS does not at present account for the impact of slope or aspect on surface irradiation. Nonetheless, the influence of slope and aspect on ice wedge degradation may be significant, as the greatest slopes in polygonal terrain typically occur at the peripheries of polygons (adjacent to the ice wedges), either on the rims of LCPs or the outer edges of HCPs. We speculate that, to an extent, aspect-related effects might cancel each other out at the scale of an entire trough; for example, any thermokarst trough with a poorly-irradiated, north-facing wall, will likewise have a well-irradiated, south-facing wall. However, field observations of the ground thermal regime are necessary to validate this assumption. Such work is warranted, as our simulations suggest that up to 15% of the annual thermal energy inputs to the trough active layer occur via laterally-oriented conduction through the adjacent sediments (Fig. 3.6S).

One final assumption in our experimental design is that active layer thickness in the trough is not affected by the depth of upper face of the ice wedge, so long as the active layer does not reach the top of the ice wedge. This assumption is tied to one of the central objectives of our simulations, which is to determine the depth of soil atop an ice wedge necessary to prevent the ice wedge from thawing in summer. As described in the Methods section, we approached this objective by calculating active layer thickness in a polygon with no cells assigned the physical properties of an ice wedge (Fig 3.1S). We considered this the simplest approach to our sensitivity analysis, as active layer thickness was unknown at the time of mesh construction, and the placement of an ice wedge too close to the surface would retard the downward progress of a seasonal thawing front, resulting in an incorrectly low estimate of potential active layer thickness. To test the validity of this assumption, we repeated a subset of pie wedge simulations after potential active layer thickness had been estimated, but included an ice wedge just below the bottom of the active layer, and monitored whether our estimate of potential active layer thickness changed. The subset of simulations represented diverse geomorphology, including an LCP (with a rim height of 30 cm and a trough depth of 5 cm), a well-drained HCP (with a trough depth of 85 cm), and a poorly drained HCP (with a trough depth of 85 cm). In the repeated simulations, the ice wedge was placed just below the bottom of the initial estimate of the active layer, by less than 5 cm (Fig 3.9S). The porosity of the ice wedge was assigned a value of 0.999. In all three simulations, our estimates of potential active layer thickness increased slightly when the ice wedge was included, but by less than 2 cm (Table 3.1S). This effect appears to be related to capillarity in mineral soil. When an ice wedge is not present, a fraction of the pore space in the upper permafrost becomes liquid each summer, even as ground temperatures remain sub-freezing, due to interactions between water molecules and the soil matrix; this process absorbs latent heat, which is wicked away from the overlying soil, marginally impeding active layer development. In contrast, when the upper permafrost is occupied by nearly pure ice, capillarity is eliminated, and the ice wedge does not partially thaw, removing this energy sink. This phenomenon results in a consistent underestimation of potential active layer thickness in simulations without an ice wedge. However, as the scale of the effect is smaller than any of the feedbacks discussed in this paper, we conclude that the absence of an ice wedge in our sensitivity analysis does not meaningfully change our findings.

Text 3.3S Acquisition of meteorological forcing data

All meteorological data were extracted or derived from the output of the Noah land surface model, a component of NASA's Global Land Data Assimilation System (GLDAS) (Rodell et al., 2004). The model simulates global meteorological conditions at a spatial resolution of 0.25º and a temporal resolution of 3 hours, ingesting observational data from ground stations and satellites. Output was extracted from the pixel centered at 148.875ºW, 69.875ºN, the same location used by Abolt et al. (2018) to validate soil parameters summarized in Table 2.1S in a polygon-scale model of thermal hydrology. Variables used to force simulations in Amanzi-ATS included air temperature, relative humidity, wind speed, incoming shortwave radiation, incoming longwave radiation, rainfall rate, and snowfall rate.

To construct a baseline year for bringing simulations to cyclical steady state, data were downloaded and processed from 2000-2015. Mean day-of-year values for each variable were calculated, generating a year-long synthetic time series representing average conditions from the recent past. The thaw degree-day (TDD) index (*i.e.*, the time integral of temperatures above 0ºC) of this synthetic year was 873 ºC d. Data from 1989 (TDD = 1188 ºC d) were used to represent a historically warm and wet year, known to have triggered extensive landscape-scale ice wedge degradation in the high Arctic (Jorgenson et al., 2006; 2015). In simulations of future, more extreme meteorological scenarios, data from 1989 were used once more, but with manipulations applied to air temperature. During each day of the year with a mean air temperature above 0ºC, air temperature was multiplied by a constant to attain a higher TDD index. This procedure was used to generate years in which TDD was equal to 1300, 1400, and 1500 ºC d. During the 133 days during which air temperature was above freezing, these manipulations represented average departures of 3.2, 4.0, and 4.7 ºC from baseline (2000-2015) conditions.

Text 3.4S Sensitivity of model output to albedo parameterization

By default, Amanzi-ATS assigns albedos of 0.141 to water and 0.135 to bare tundra (Atchley et al., 2015), based on observations from Cogley (1979) and Grenfell and Perovich (2004). We explored the sensitivity of seasonal thaw depths in the trough to this parameterization by repeating a subset of simulations, assuming a higher-contrast scenario between soil and water. Supplementary simulations were executed on all meshes with a trough width of 1 m, assigning albedos of 0.05 to water and 0.15 to bare tundra, based on observations from Gamon et al. (2012). In the high-contrast set of simulations, potential active layer thickness in the trough ($\mathrm{pALT}_{\mathrm{tro}}$) was effectively unchanged from the main set of simulations (Figure 3.4S). Unlike earlier simulations, however, downward net radiation on sunny days in early summer was modestly higher above inundated troughs relative to well-drained troughs, matching field observations from Langer et al. (2011a) and Jorgenson et al. (2015).

Table 3.1S

Summary of simulations including cells designated as in ice wedge, described in Text 3.2S

Rim height (cm)	Trough depth (cm)	Trough drainage	pALTtro (cm) (without ice wedge)	pALTtro (cm) (with ice wedge)
30	5	poorly-drained	82.9	83.6
0	85	poorly-drained	89.8	91.0
0	85	well-drained	81.9	82.5

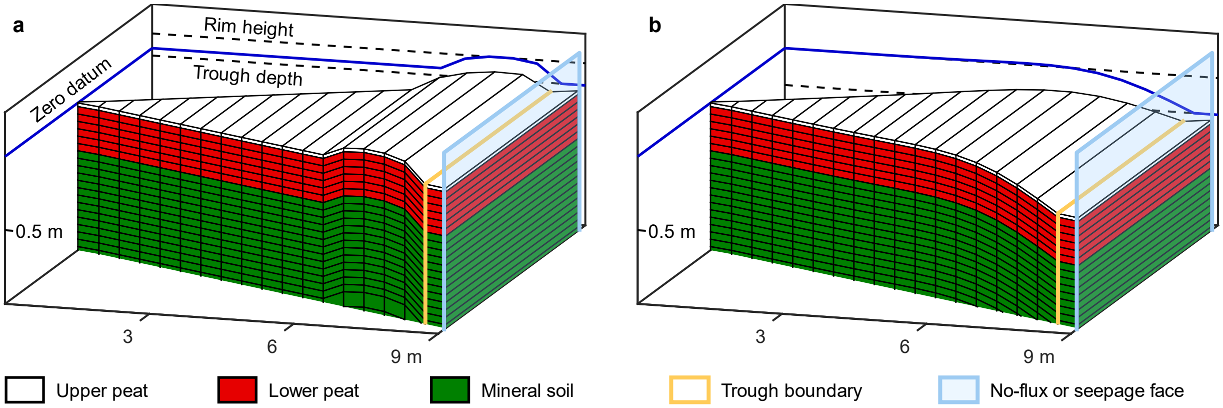

Figure 3.1S

Schematic of pie-wedge meshes used for Amanzi-ATS simulations, with important boundaries indicated (vertical exaggeration=3). Examples include an LCP (**a**) and an HCP (**b**) with narrow troughs. Only top layers are shown; mesh extends (as mineral soil) to a depth of 50 m.

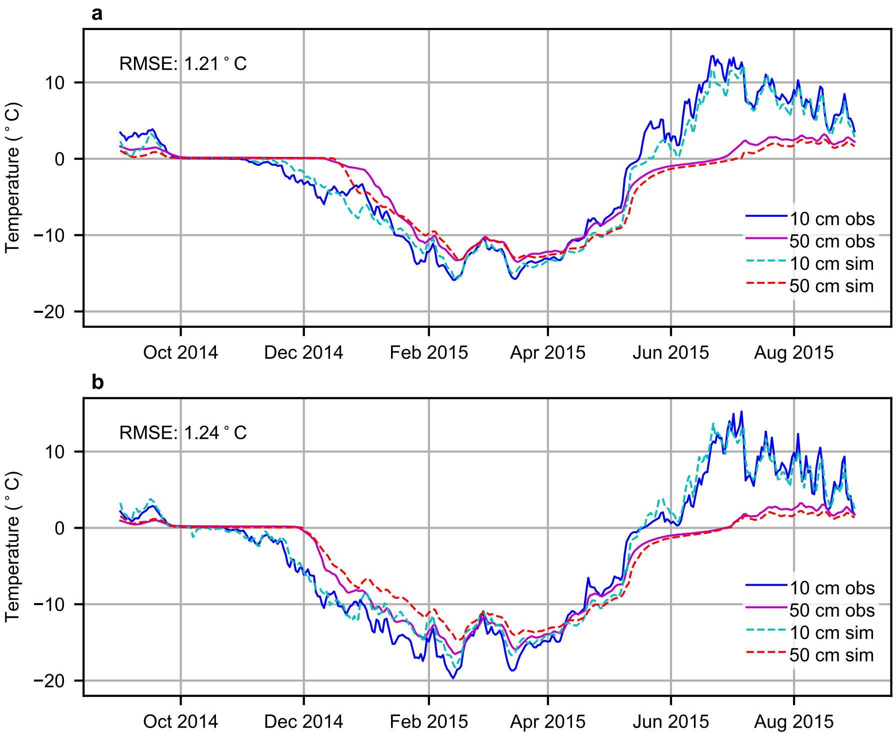

Figure 3.2S

Comparison of simulated ground temperature in the center (**a**) and rim (**b**) of an idealized pie wedge mesh with observational data from a low-centered polygon near Prudhoe Bay, Alaska, described in Abolt et al. (2018).

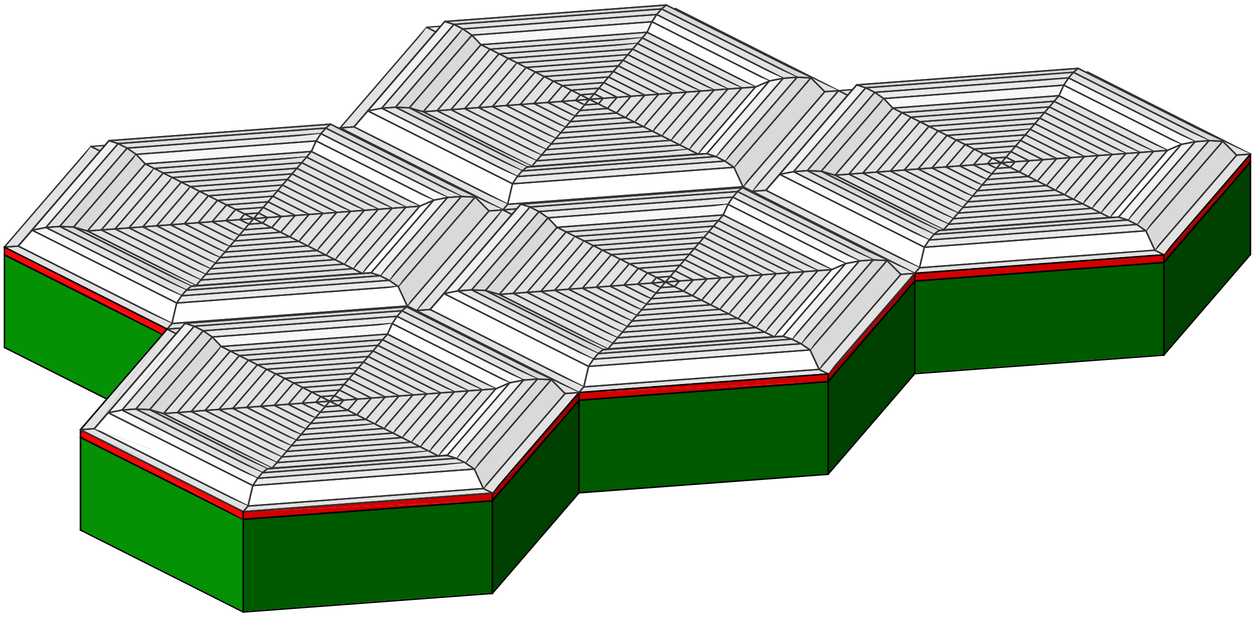

Figure 3.3S

Schematic of an idealized landscape of ice wedge polygons, comprising repeated instances of the same pie wedge unit. Simulations executed on a single pie wedge mesh were designed on the assumption that energy and hydrologic fluxes between adjacent pie wedge units are negligible through symmetry.

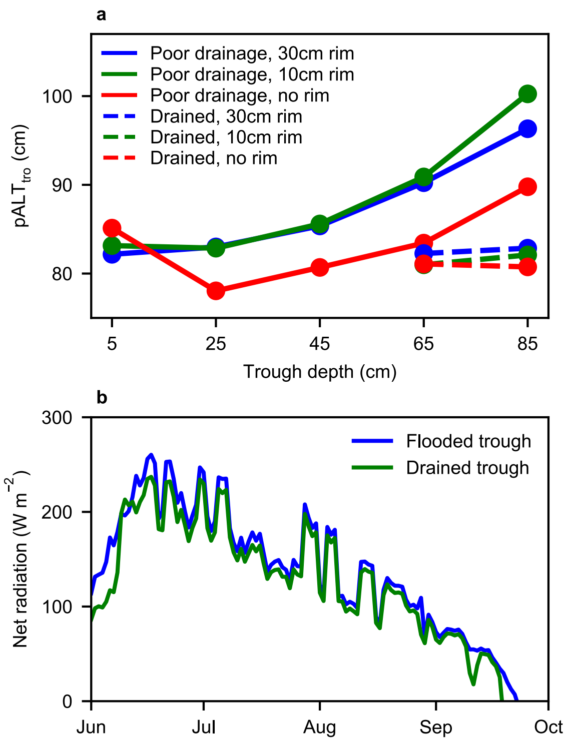

Figure 3.4S

Potential active layer thickness in the trough assuming a high albedo contrast between surface water and bare tundra (**a**). Time series of daily net radiation into the trough during summer at cyclical steady state, comparing results from simulations with 5 and 85 cm troughs, the latter inundated (**b**). Differences between a flooded and a drained trough on sunny days in early June are similar in scale to observations reported by Langer et al. (2011a) and Jorgenson el al. (2015).

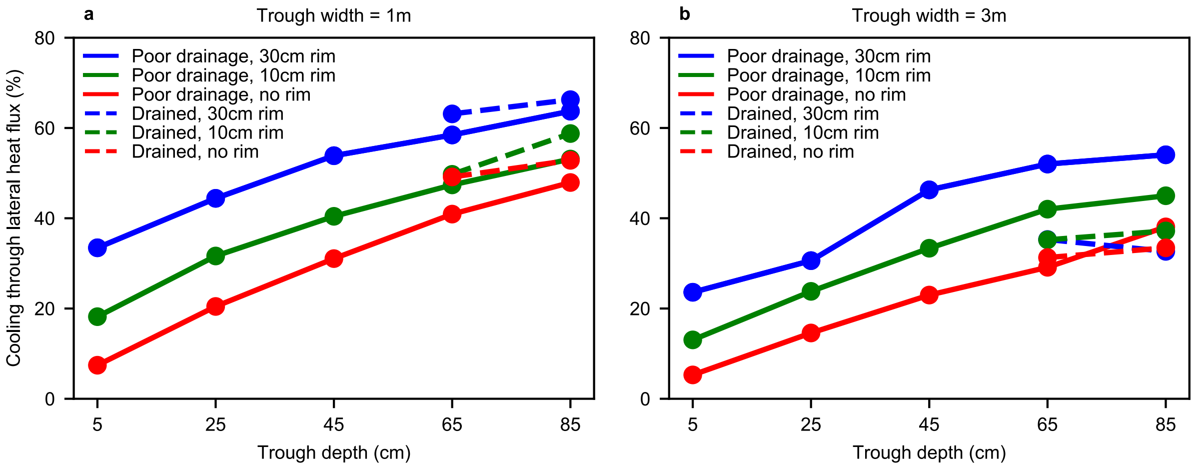

Figure 3.5S

Percent of winter cooling in the active layer of the trough attributable to lateral, conductive energy fluxes between the trough and the polygon interior, at cyclical steady state. Results shown for troughs with widths of 1 m (**a**) and 3 m (**b**). Ratios were calculated by dividing the net annual outward conductive energy flux at the boundary of the trough (plane indicated in Figure 3.1S) by the gross annual downward flux of energy into the trough.

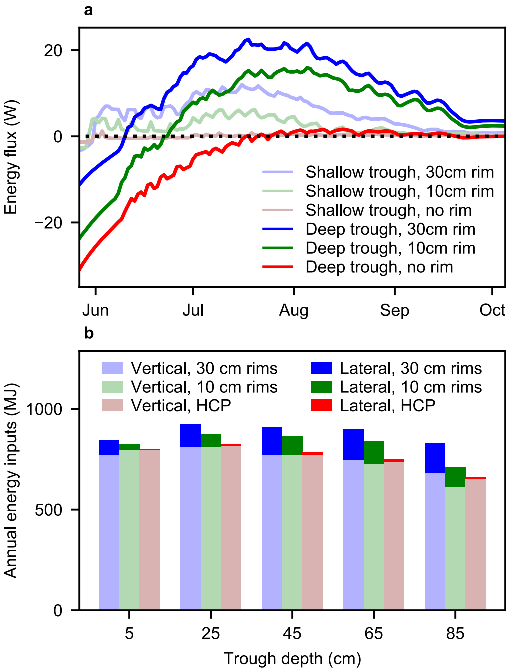

Figure 3.6S

Laterally-oriented conductive heat flux from the polygon interior toward the trough in summer, from simulations with narrow troughs (**a**) (Note: Boundary indicated in Figure 3.1S). Comparison between seasonally integrated, laterally-oriented thermal inputs to the trough subsurface and vertical inputs, from simulations with poor drainage (**b**). (Note: In both plots, fluxes into the trough soil column as positive. ‘Shallow trough’ signifies a depth of 5 cm, and ‘deep trough’ refers to an 85 cm trough with poor drainage.

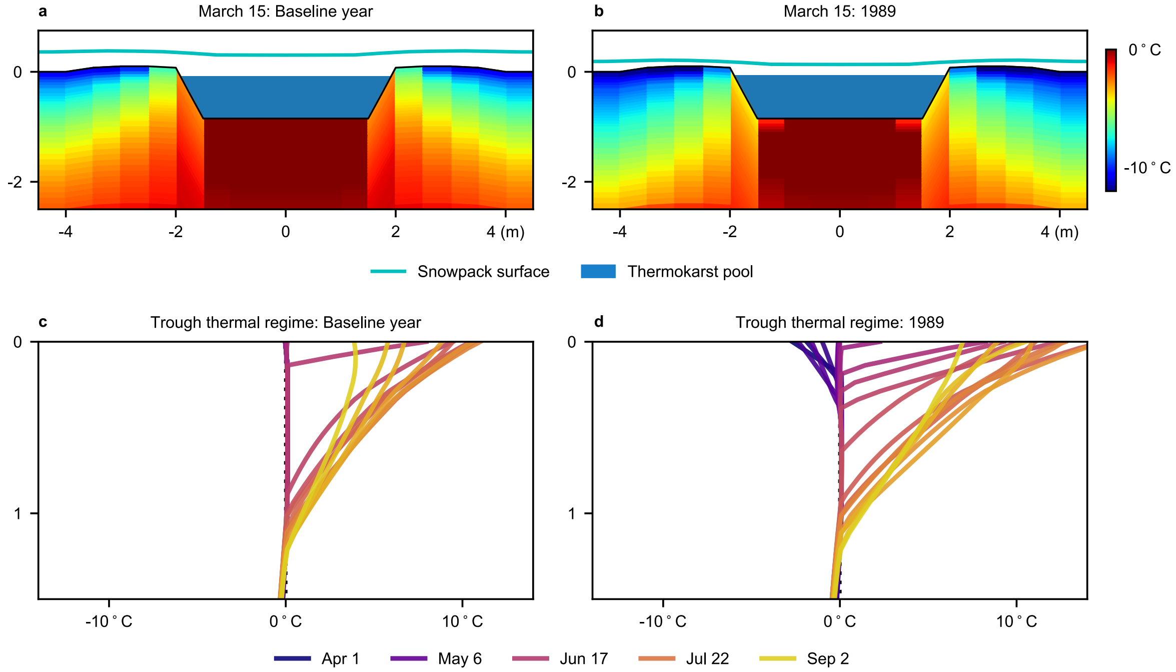

Figure 3.7S

Snapshots of ground temperature, snow depth, and surface water in late winter beneath a wide, deeply flooded trough, during an average year (**a**) and using forcing data from 1989 (**b**). Profiles of the ground thermal regime beneath the trough bottom each week during the thaw season, during the average year (**c**) and 1989 (**d**). Despite markedly warm summer conditions, the active layer fails to deepen appreciably in 1989 due to enhanced freeze-back during the winter, caused by thin snow cover.

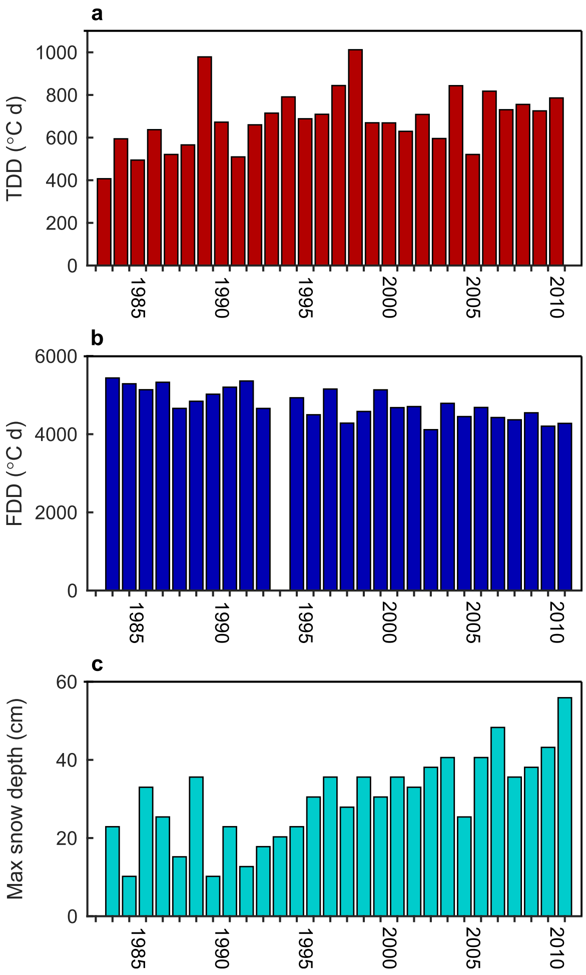

Figure 3.8S

Historic meteorology at the Kuparuk, Alaska station (ID USC00505136) of the Global Historical Climatology Network (GHCN), chosen for its long record of continuous data (Menne et al., 2012). An upward tend is evident in thaw degree days (TDD; the time integral of air temperatures greater than 0°C), from 1982-2011, with particularly severe summers in 1989 and 1998 (**a**). Simultaneously, a downward trend in freezing degree days (FDD) indicates increasingly mild winters (**b**). (Note: There is no estimate from the winter of 1993-1994 due to a one-month gap in data.) An upward trend in maximum snow accumulation (**c**) contributed to favorable conditions for thermokarst over the same period by providing enhanced insulation for the active layer beneath flooded troughs in winter.

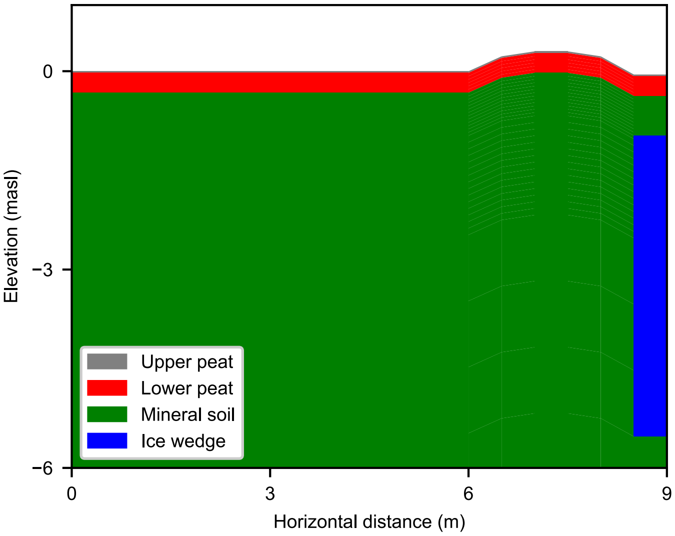

Figure 3.9S

Cross-section of a pie-wedge mesh representing an LCP, modified to include an ice wedge, for simulations described in Text 3.2S.

Chapter 4: A machine-learning-based tool for rapid extraction of ice wedge polygons from high-resolution digital elevation models[2]

ABSTRACT

We present a workflow for rapid delineation and microtopographic characterization of ice wedge polygons within high-resolution digital elevation models. At the core of the workflow is a convolutional neural network used to detect pixels representing polygon boundaries. A watershed transformation is subsequently used to segment imagery into discrete polygons. Fast training times (<5 minutes) permit an iterative approach to improving skill as the routine is applied across broad landscapes. Results from study sites near Utqiaġvik and Prudhoe Bay, Alaska demonstrate robust performance in diverse tundra settings, with manual validations demonstrating 70-96% accuracy by area at the kilometer scale. The methodology permits precise, spatially extensive measurements of polygonal microtopography and trough network geometry.

4.1 Introduction

This research addresses the problem of delineating and measuring ice wedge polygons within high-resolution digital elevation models (DEMs). Ice wedge polygons are the surface expression of ice wedges, a form of ground ice nearly ubiquitous to coastal tundra environments

---

[2] published as: Abolt CJ, Young MH, Atchley AL, Wilson CJ. 2019. Rapid machine-learning-based extraction and measurement of ice wedge polygons in high-resolution digital elevation models. *The Cryosphere* 13: 237-245. CJA conceived the study, developed and the workflow and wrote the manuscript.

in North America and Eurasia (Leffingwell, 1915; Lachenbruch, 1962). High resolution inventories of ice wedge polygon microtopography are of hydrologic and ecologic interest, because decimeter-scale variability in polygonal relief can drive pronounced heterogeneity in soil drainage (Liljedahl et al., 2016) and surface emissions of CO_2 and CH_4 (Lara et al., 2015; Wainwright et al., 2015). At typical sizes, several thousand ice wedge polygons may occupy a single square kilometer of terrain, motivating our development of an automated approach to mapping. The key innovation in our method is the use of a convolutional neural network (CNN), a variety of machine learning algorithm, to identify pixels representing polygon boundaries. Integrated within a set of common image processing operations, this approach permits the extraction of microtopographic attributes from entire populations of ice wedge polygons at the kilometer scale or greater.

Previous geospatial surveys of polygonal microtopography have often aimed to map the occurrence of two geomorphic endmembers: basin-shaped low-centered polygons (LCPs), which are characterized by rims of soil at the perimeters, and hummock-shaped high-centered polygons (HCPs), which often are associated with permafrost degradation. Employing historic aerial photography, several prior analyses have demonstrated a pan-Arctic acceleration since 1989 in rates of LCP conversion into HCPs, a process which improves soil drainage and stimulates enhanced emissions of CO_2 (Jorgenson et al., 2006; Raynolds et al., 2014; Jorgenson et al., 2015; Liljedahl et al., 2016). Nonetheless, precise rates of geomorphic change have been difficult to quantify, as these surveys typically have relied on proxy indicators, such as the presence of ponded water in deepening HCP troughs. More Recently, in an effort to characterize contemporary polygonal microtopography, a landcover map of LCP and HCP occurrence across the Arctic coastal plain of northern Alaska was developed using multispectral imagery from the Landsat 8 satellite at 30 m resolution (Lara et al., 2018). This dataset offers a static estimate of variation in polygonal form over unprecedented spatial scales; however, geomorphology was inferred from the characteristics of pixels larger than typical polygons, preventing inspection of individual features.

Higher-resolution approaches to segment imagery into discrete ice wedge polygons have often been motivated by efforts to analyze trough network geometry. On both Earth and Mars, for example, paleo-environmental conditions in remnant polygonal landscapes have been inferred by comparing parameters such as boundary spacing and orientation with systems in modern periglacial terrain (e.g., Pina et al., 2008; Levy et al., 2009; Ulrich et al., 2011). An early semi-automated approach to delineating Martian polygons from satellite imagery was developed by Pina et al. (2006), who employed morphological image processing operations to emphasize polygonal boundaries, then applied a watershed transformation (discussed in Section 4.3.1.3) to identify discrete polygons. This workflow was later applied to lidar-derived DEMs from a landscape outside Utqiaġvik, Alaska by Wainwright et al. (2015), but in their experience and our own, robust results at spatial scales approaching a square kilometer or greater were elusive.

Our application of CNNs to the task of identifying polygonal troughs was inspired by the remarkable solutions that CNNs recently have permitted to previously intractable image processing problems. Aided by advances in the performance of graphics processing units (GPUs) over the last decade, CNNs have demonstrated unprecedented skill at tasks analogous to ice wedge polygon delineation, such as cell membrane identification in biomedical images (Ciresan et al., 2012) or road extraction from satellite imagery (Kestur et al., 2018; Xu et al., 2018).

Motivated by this potential, an exploratory study was recently conducted by Zhang et al. (2018), who demonstrated that a sophisticated neural network, the Mask R-CNN of He et al. (2017), is capable of end-to-end extraction of ice wedge polygons from satellite-based optical imagery, capturing ~79% of ice wedge polygons across a 134 km^2 field site and classifying each as HCP or LCP. The authors concluded that the method has potential for pan-Arctic mapping of polygonal landscapes. Here we explore an alternative approach, using a less complex CNN paired with a set of post-processing operations, to extract ice wedge polygons from high-resolution DEMs derived from airborne Lidar surveys. An advantage to this method is that training the CNN is rapid (~5 minutes or less on a personal laptop), permitting an iterative workflow in which supplementary data can easily be incorporated to boost skill in targeted areas. We demonstrate the suitability of this approach to extract ice wedge polygons with very high accuracy (up to 96% at the kilometer scale), applying it to ten field sites of 1 km^2 outside Utqiaġvik and Prudhoe Bay, Alaska. Because our method operates on high resolution elevation data, it enables direct measurement of polygonal microtopography, and we anticipate that in the future, the method will permit precise monitoring of surface deformation in landscapes covered by repeat airborne surveys.

4.2 Study areas and data acquisition

To demonstrate the flexibility of our approach, we applied it simultaneously at two clusters of study sites near Utqiaġvik and Prudhoe Bay, Alaska, settings with highly divergent ice wedge polygon geomorphology, ~300 km distant from one another (Fig 4.1S).

4.2.1 Utqiaġvik

The first cluster of study sites (Figs. 4.2S-4.3S) is located within 10 km of the Beaufort Sea coast in the Barrow Environmental Observatory, operated by the National Environmental Observatory Network (NEON). Mean elevation is less than 5 m above sea level, and vegetation consists of uniformly low-growing grasses and sedges. Mesoscale topography is mostly flat but marked by depressions up to 2 m deep associated with draws and drained lake beds. In the landcover map of Lara et al. (2018), the area is characterized by extensive coverage by both LCPs and HCPs, with occasional lakes and patches of non-polygonal meadow. Microtopography at the sites reflects nearly ubiquitous ice wedge development, which becomes occluded in some of the depressions. Ice wedge polygons are of complex geometry and highly variable area, ranging from ~10 m^2 to >2000 m^2. An airborne lidar survey was flown in August 2012 as part of the U.S. Department of Energy's Next Generation Ecosystems Experiment-Arctic program (https://ngee-arctic.ornl.gov/). The resulting point cloud was processed into a 25 cm horizontal resolution DEM with an estimated vertical accuracy of 0.145 m (Wilson et al., 2012). In the present study, to compare algorithm performance on data of variable spatial resolution, the 25 cm DEM was resampled at 50 cm and 100 cm resolution. Two sites of 1 km^2, here referred to as Utqiaġvik-1 and Utqiaġvik-2, were extracted from the DEMs and processed using our workflow.

4.2.2 Prudhoe Bay

The second cluster of sites (Figs. 4.4S-4.11S) is approximately 300 km east of the first and farther inland, located ~40 km south of Prudhoe Bay, AK (Fig 4.1S). As at Utqiaġvik, vegetation consists almost exclusively of low and even-growing grasses and sedges. Mesoscale topography is generally flat, with a slight (<4%) dip toward the northwest. In the landcover map of Lara et al. (2018), the area is primarily characterized by HCPs, with smaller clusters of LCPs, patches of non-polygonal meadow, and occasional lakes. Ice wedge polygons are generally of more consistent area than those of Utqiaġvik, ~400-800 m^2. Airborne lidar data was acquired in August 2012 by the Bureau of Economic Geology at the University of Texas at Austin (Paine et al., 2015) and subsequently processed into 25 cm, 50 cm, and 100 cm resolution DEMs. Vertical accuracy was estimated at 0.10 m. As the Prudhoe Bay survey area is substantially larger than the survey area at Utqiaġvik, eight sites of 1 km^2, here referred to as Prudhoe-1 through Prudhoe-8, were extracted from the DEMs and processed using our workflow.

4.3 Methods

4.3.1 Polygon delineation algorithm

A chart summarizing our iterative workflow is presented in Fig. 4.1, and several intermediate stages in the polygon delineation algorithm are illustrated in Fig. 4.2. In the first (pre-processing) stage, regional trends were removed from a DEM (Fig. 4.12S), generating an image of polygonal microtopography (Fig. 4.2a). Next, the microtopographic information was processed by a CNN, which was trained to use the 27×27 neighborhood surrounding each pixel to assign a label of "boundary" or "not boundary" (Fig. 4.2b). A distance transformation was then applied, (i.e., each non-boundary pixel was assigned a negative intensity proportional to its Euclidean distance from the closest boundary), generating a grayscale image analogous to a DEM of isolated basins, in which the polygonal boundaries appear as ridges (Fig. 4.2c).

Subsequently, a watershed transform was applied to segment the image into discrete ice wedge polygons (Fig. 4.2d). These steps, and a post-processing algorithm used to remove non-polygonal terrain from the final image, are described in detail below.

4.3.1.1 Pre-processing

In the pre-processing stage, regional topographic trends were estimated by processing the DEM with a 2D filter, which assigned to each pixel the mean elevation within a 20 m radius. This radius was chosen such that the area over which elevation was averaged would be larger than a typical ice wedge polygon. Polygon-scale microtopography was then estimated by subtracting the regional topography from the DEM (Fig 4.12S). In preparation for passing the data to the CNN, microtopography was subsequently converted to 8-bit gray-scale imagery. The minimum intensity (0) was assigned to depressions of 0.7 m or greater, and the maximum intensity (255) was assigned to ridges of 0.7 m or greater. These bounds captured >99% of pixel values at each study site. Finally, one thumbnail-sized image was created for each pixel in the microtopography raster, capturing the immediate neighbourhood surrounding it. These thumbnail images were the direct input to the CNN. The CNN required the width in pixels of each thumbnail to be an odd multiple of 9; therefore, at 50 cm resolution the thumbnails were assigned a width of 27 pixels (13.5 m), at 25 cm resolution a width of 45 pixels (11.25 m), and at 100 cm resolution a width of 27 pixels (27 m). The width of these thumbnails was chosen such that each image would contain sufficient spatial context for a human observer to distinguish easily between polygonal boundaries, which typically were demarcated by inter-polygonal troughs, and other microtopographic depressions such as LCP centers.

4.3.1.2 Convolutional neural network

The function of the CNN in our workflow was to identify pixels likely to represent boundaries. Conceptually, a CNN is a classification tool that accepts images of a fixed size (in our case, the thumbnails described in the previous section) as input and generates categorical labels as output. The CNN determines decision criteria through training with a set of manually-labeled images. The architecture of a CNN consists of a user-defined sequence of components, or layers, which take inspiration from the neural connections of the visual cortex. We developed our CNN in MATLAB (R2017b) using the Image Processing, Parallel Computing, and Neural Network toolboxes. We purposefully constructed the CNN with an architecture of minimal complexity, to maximize the efficiency of training and application. Here we briefly describe the function of each layer in our CNN; for more detailed description, the reader is directed to Ciresan et al. (2012).

Summarized in Table 4.1S, the most important components of our CNN were a single convolutional layer, a max-pooling layer, and two fully connected layers. In the convolutional layer, a set of 2D filters was applied to the input image, generating intermediate images in which features including concavities, convexities, or linear edges were detected. The max-pooling layer downsized the height and width of these intermediate images by a factor of three, by selecting the highest intensity pixel in a moving 3×3 window with a stride of 3 pixels. Each pixel in the downsized intermediate images was then passed as an input signal to the fully connected layers, which functioned identically to standard neural networks. Two additional components of our CNN were Rectified Linear Unit (ReLU) layers, which enhance non-linearity by reassigning a value of zero to any negative signals output by a preceding layer, and a softmax layer, which converted the output from the final fully connected layer into a probability for each categorical label (i.e., boundary or not boundary).

During training, the weights of the 2D filters in the convolutional layer and the activation functions of the neurons in the fully connected layers were optimized to correctly predict the labels in a training deck of images. Our workflow was designed to generate the training deck primarily by processing 100 ×100 m tiles of manually-labeled imagery. In each of these tiles, boundary pixels were delineated by hand in a standard raster graphics editor, a process that required ~1 hour per tile at 50 cm resolution (Fig. 4.13S). Our algorithm imported these tiles, identified the geographic coordinates of each pixel identified as a boundary, then created a thumbnail image centered on that pixel from the 8-bit microtopographic imagery. This procedure generated several thousand thumbnail images centered on boundaries from each manually delineated tile. Subsequently, an equal number of pixels not labeled as boundaries were selected at random, and the thumbnail extraction procedure was repeated, generating a set of non-boundary images for the training deck. Finally, for more targeted training that did not require full delineation of a 100 ×100 m tile, individual instances of boundary or non-boundary features could also be added to supplement the training deck, based again on manual delineation (Fig. 4.13S). Just prior to training, 25% of the training deck assembled by these methods was set aside to be used for validation.

Once trained, the CNN was executed to assign a label of "boundary" or "not boundary" to the thumbnail image corresponding to each pixel of a study site. These labels were then reassembled into a binary image of polygon boundaries (Fig. 4.2b), which was further processed to extract discrete ice wedge polygons.

4.3.1.3 Polygon extraction

After applying the CNN to classify all pixels at a site as boundary or not boundary, we extracted discrete ice wedge polygons by applying several standard image processing operations. The first step was elimination of "salt and pepper" noise in the binary image, which we accomplished by eliminating all contiguous sets of boundary-identified pixels with an area < 20 m2. This threshold was selected based on the reasoning that most true boundary pixels should be part of a continuous network, covering an area arbitrarily larger than 20 m^2, while most false detections should occur in smaller clusters. Next, we applied a distance transform, assigning to every non-boundary pixel a negative intensity equal to its Euclidean distance from the nearest boundary. This created an intermediate image in which each ice wedge polygon appeared as a valley, surrounded on all or most sides by ridges representing the ice wedge network (Fig. 4.2c). At this stage, to prevent over-segmentation, valleys with maximum depths of 1.5 meters or less were then identified and merged with the closest neighbor through morphological reconstruction (Soille, 1992). The effect of this procedure was to ensure that the algorithm would only delineate polygons whose centers contained at least one point greater than 1.5 m from the boundaries, as field observations indicate that ice wedge polygons tend to measure at least several meters across (Leffingwell, 1915; Lachenbruch, 1962). Next, watershed segmentation was applied to divide the valleys into discrete polygons (Fig. 4.2d). Our use of this operation was inspired by its incorporation in the polygon delineation method developed by Pina et al. (2006). Conceptually, this procedure was analogous to identifying the up-gradient region or area of attraction surrounding each local minimum.

4.3.1.4 Partitioning of non-polygonal ground

In the final stage of delineation, we partitioned out regions of a survey area that had been segmented using the techniques described above, but were unlikely to represent true ice wedge polygons. For example, polygons were eliminated from the draw in the southern half of Utqiaġvik-1 (Fig. 4.2S), where microtopography was too occluded to permit accurate delineation. Toward this aim, our algorithm analysed individually each boundary between two polygons (black line segments in Fig. 2D), tabulating the number of pixels that had been identified positively by the CNN (white pixels in Fig. 4.2b). It then dissolved all boundaries in which less than half the pixels had been classified positively, merging adjacent polygons. In practice, this procedure resulted in areas of non-polygonal terrain being demarcated by unusually large "polygons." We removed these areas by partitioning out any polygon with an area greater than 10,000 m^2, a threshold selected to be arbitrarily larger than most real ice wedge polygons. This procedure had the strengths of being conceptually simple and providing a deterministic means of partitioning non-polygonal terrain from the rest of a survey area.

4.3.2 Microtopographic analysis

To demonstrate the capabilities of our workflow for microtopographic analysis, we developed a simple method for measuring the relative elevation at the center of each delineated polygon, serving as a proxy for LCP or HCP form. In each polygon, we first applied a distance transform, calculating the distance from the closest boundary of all interior pixels. We then divided the area of the polygon in half at the median distance from boundaries, designating a ring of "outer" pixels and an equally sized core of center pixels. Microtopographic relief was then estimated as the difference in mean elevation between the center and outer pixels.

4.3.3 Case study experimental design

The case study was first conducted using topographic data at 50 cm resolution, then repeated at 25 cm and 100 cm resolution. Training was focused primarily on sites Prudhoe-1 and Utqiaġvik 1. Leveraging the rapid training and application times of our CNN, we manually delineated one 100 ×100 m tile of imagery at a time from either site, trained the CNN, extracted results from both sites, then introduced additional training data from regions of poor performance to improve skill (Fig. 4.1). After four iterations of this approach, the CNN incorporated training data from three fully-delineated tiles at Utqiaġvik-1 and one at Prudhoe 1, representing 3% and 1% of the sites, respectively. From this point, we opted to "fine-tune" the CNN by supplementing the training deck directly with instances of problematic features, rather than using information from fully-delineated tiles. Several examples of boundary and non-boundary features were included from Utqiaġvik-1 and Prudhoe-1. Next, to test its extensibility, the CNN was applied across the remaining sites, and re-trained once more. In this final iteration, several instances of boundary and non-boundary features (but no fully delineated tiles) were incorporated into the training deck from sites Prudhoe-2, Prudhoe-3, and Prudhoe-4. No training data at all were incorporated from sites Prudhoe-5 through Prudhoe 8 or Utqiaġvik 2. (All training data used in the final iteration of our workflow can be viewed in the data and code repository accompanying this article.) Once this procedure was complete at 50 cm resolution, training decks at 25 cm and 100 cm resolution were prepared. To generate CNNs comparable to the network trained on 50 cm data, the 25 cm and 100 cm training decks were constructed using data sampled from identical geographic locations, but manual labeling was performed without reference to the labeled 50 cm resolution data.

After the CNN was trained and applied across all study sites, we quantified the performance of the polygon delineation algorithm through manual validation. At each site, we first calculated the total area and number of polygons extracted from the landscape. We then randomly sampled 500 of the computer-delineated polygons, and classified each as either whole, fragmentary, conglomerate, or false. Fragmentary polygons were defined as computer-delineated polygons that included less than 90% of one real polygon; conglomerate polygons were defined as computer-delineated polygons comprising parts of two or more real polygons; and false polygons were defined as computer-delineated polygons occupying terrain in which no polygonal pattern was deemed visible to the human evaluator. The percentage of computer-delineated polygonal terrain corresponding to each class was then calculated by number of polygons and by area. This procedure was completed for all ten study sites at 50 cm data resolution, and for sites Prudhoe-1 and Utqiaġvik-1 at 25 cm and 100 cm resolution.

4.4 Results and discussion

4.4.1 Training speed and accuracy

Due to the compact architecture of our CNN, training speeds at 50 cm resolution and 100 cm resolution were rapid. At 50 cm resolution, the training procedure operated on a deck of ~36,000 thumbnail images. Executed on a personal laptop with an Intel i7 CPU and a single GeForce MX150 GPU, accuracies >97% on the training deck and >95% on the validation deck of thumbnails were achieved in less than five minutes. At 100 cm resolution, the procedure operated on ~12,000 thumbnail images, achieving comparable levels of accuracy within 90 seconds. These speeds enable the iterative approach to training on which our workflow is based (Fig. 4.1), as the CNN can be re-trained quickly to incorporate new data when applied across increasingly large areas.

Using 25 cm resolution data, the training procedure operated on a set of ~115,000 thumbnail images. Accuracies >97% on the training deck and >95% on the validation deck were once more obtained, but training required just under one hour on the same computer. This substantial increase to training time is attributable to the facts that more thumbnail images were processed, and the number of pixels in each thumbnail was larger, making execution of the CNN more computationally expensive.

4.4.2 Delineation speed and validation

Operating at 50 cm resolution, delineation of ice wedge polygons within a 1 km^2 field site required ~2 minutes, including application of the CNN and subsequent post-processing. Results generally were very accurate; across study sites, ~1000-5000 ice wedge polygons were detected per square kilometer, of which 85-96% were estimated as “whole” during manual validation, representing 70-96% of the polygonal ground by area (Table 4.1). The most common type of error at all sites with <95% accuracy was incorrect aggregation of several real ice wedge polygons into a single feature. Unsurprisingly, performance was strongest at sites with clearly defined polygon boundaries and relatively simple polygonal geometry, such as Prudhoe-1, Prudhoe-7, and Prudhoe-8 (Figs. 4.1S, 4.10S, 4.11S). In contrast, performance was weakest at sites such as Utqiaġvik-2 or Prudhoe-6 (Figs. 4.2S, 4.9S), where considerable swaths of terrain are characterized by faint microtopography, as ice wedge polygons appear to grade into non-polygonal terrain. In such locations, polygonal boundaries frequently went undetected, resulting in the delineation of unrealistically large conglomerate polygons. In general, the results of the delineation clearly illustrate that the polygonal network at Utqiaġvik possesses more complex geometry than Prudhoe Bay, with many instances where secondary or tertiary ice wedges appear to subdivide larger ice wedge polygons.

Although simple, our post-processing procedure for partitioning out non-polygonal ground from the results was generally accurate. Examples of features successfully removed from the 50 cm resolution DEMs included thaw lakes (Figs. 4.6S-4.10S), drained thaw lake basins (Fig. 4.2S), stream beds (Figs. 4.5S, 4.9S), non-polygonal marsh (Figs. 4.3S, 4.7S, 4.9S), shallow ponds (Fig. 4.7S), and the flood plain of a braided stream (Fig. 4.10S). Because the partitioning procedure removed areas with a low density of boundaries identified by the CNN, we found that it could be trained efficiently by supplementing the training deck with extra examples of “non-boundary” thumbnails extracted from these regions. Across the study sites, we encountered almost no cases where well-defined polygons were mistakenly partitioned out. Instances of non-polygonal ground mistakenly classified as polygonal accounted for less than 1% of machine-delineated polygons by area.

When the delineation algorithm was repeated using data at 100 cm resolution, delineation speeds increased somewhat, but performance dropped significantly, with greater declines occurring in the challenging environment of Utqiaġvik (Table 4.2S). We attribute declines in performance to an obscuration of fainter polygonal boundaries at this resolution, and to decreases in the amount of contextual information that can be derived from the neighborhood of any given pixel, reducing the capacity for the algorithm to distinguish between polygonal troughs and other microtopographic depressions (Fig. 4.14S). Somewhat surprisingly, performance also declined slightly using data at 25 cm resolution, with larger fractions of fragmentary and false polygons accounting for most of the increases in errors (Table 4.2S). We attribute these mistakes to the larger number of distinguishable features in the higher resolution data, leading the algorithm to more frequently mistake features not encountered in the training dataset as boundary pixels. As the imagery nonetheless is of sufficient resolution for our purposes, we anticipate that, with augmentations to the training dataset, performance at 25 cm resolution could improve and even exceed performance at 50 cm resolution; however, performance speeds were generally inhibitory to our workflow, as delineation required ~50 minutes per square kilometer. We therefore conclude that 50 cm resolution data is optimal for our analysis.

4.4.3 Measurement of polygonal microtopography

The time required to execute our procedure for measuring polygonal microtopography varied from ~10-30 seconds per square kilometer at 50 cm resolution, depending on the number of polygons delineated. A comparison of calculated relief at polygon centers between Prudhoe-1 and Utqiaġvik-1 reveals that both sites are characterized by the prevalence of HCPs, which surround smaller clusters of LCPs (Fig. 4.3). Relief tends to be more extreme at Utqiaġvik, with the relative elevation of polygon centers commonly approaching 20-30 cm. Our automated calculations of relief align well with visual inspection of the DEMs, as rimmed LCPs are consistently assigned negative center elevations. To our knowledge, our results represent the first direct measurement of polygonal relief at the kilometer-scale, demonstrating a spectrum of center elevations rather than a binary classification into LCP or HCP. We anticipate these measurements may be useful for further investigations into relationships between microtopography, soil moisture, and carbon fluxes (e.g., Wainwright et al., 2015).

4.4.4 Comparison with Mask R-CNN and future applications

Several key differences are apparent between the workflow presented in this paper (hereafter termed the CNN-watershed approach) and a recent implementation of Mask R-CNN for mapping of ice wedge polygons (Zhang et al., 2018), revealing relative strengths to each approach. An advantage of the CNN-watershed approach, stemming from its sparse neural architecture, is that training times are extremely rapid, facilitating iterative improvements to skill (Fig. 4.1). In contrast, although inference times using the CNN-watershed approach are reasonable, extraction of ice wedge polygons over broad landscapes is several times faster using Mask R-CNN, with a reported time of ~21 minutes for inference over 134 km^2 of terrain (Zhang et al., 2018). Because the CNN-watershed approach operates on high-resolution DEMs, it enables direct quantification of polygonal relief, whereas Mask R-CNN instead produces a binary classification of each polygon as either LCP or HCP. The CNN-watershed approach is therefore useful for generating unique datasets summarizing polygonal geomorphology, demonstrating high-performance at spatial scales typical of airborne surveys using lidar or photogrammetry to produce high-resolution DEMs. In comparison, because Mask R-CNN has been trained to operate on satellite-derived optical imagery with global coverage, it is uniquely well-suited for application across very broad regions, with potential to generate pan-Arctic maps of land cover by polygon type. Because of differences in training and inference procedures and the spatial scales at which they ideally operate, the training data requirements and accuracy of the two approaches are difficult to compare directly; nonetheless, in several aspects, performance appears to be similar (Text 4.1S).

Because the CNN-watershed approach generates direct measurements of polygonal microtopography, one application to which it is uniquely amenable is precise monitoring of microtopopographic deformation in areas covered by repeat airborne surveys. Through such analysis, we anticipate that it will permit polygon-level quantification of ground subsidence over timespans of years, potentially yielding new insights into the vulnerability of various landscape units to thermokarst. An additional research problem to which the CNN-watershed approach is well-suited is quantification of polygonal network parameters, such as boundary spacing and orientation, to explore relationships to environmental factors such as climate (e.g., Pina et al., 2008; Ulrich et al., 2011). These boundaries (black line segments in Figs 4.2D, 4.3B, 4.3D) are naturally delineated through implementation of the watershed transformation. We acknowledge that, because the surface expression of ice wedges is sometimes subtle or non-existent, ground-based delineation methods are the highest-accuracy approach to mapping ice wedge networks (Lousada et al., 2018). Nonetheless, by segmenting machine-delineated networks into individual boundaries, our workflow permits the estimation of network statistics at spatial scales unattainable through on-site surveying.

4.5 Conclusions

A relatively simple CNN paired with a set of common image processing techniques is capable of extracting polygons of highly variable size and geometry from high-resolution DEMs of diverse tundra landscapes. Successful application of the CNN is facilitated by its sparse neural architecture, which permits rapid training, testing, and incorporation of new data to improve skill. The optimal spatial resolution for DEMs processed using the workflow is ~50 cm. Potential applications for the technology include: generation of high-resolution maps of land cover by polygon type, precise quantification of microtopographic deformation in areas covered by repeat airborne surveys, and rapid extraction of center elevations and boundary parameters including spacing and orientation. These capabilities can improve understanding of environmental influences on network geometry and facilitate assessments of contemporary landscape evolution in the Arctic.

Data and code for the tool are available at: http://doi.org/10.5281/zenodo.2554542.

ACKNOWLEDGEMENTS

We are grateful for the support provided for this research, which included: the Next Generation Ecosystem Experiments Arctic (NGEE-Arctic) project (DOE ERKP757) funded by the Office of Biological and Environmental Research in the U.S. Deparment of Energy Office of Science, and the NASA Earth and Space Science Fellowship program, for an award to CJA (80NSSC17K0376). We thank Ingmar Nitze (Alfred Wegener Institute for Polar and Marine Research) and Weixing Zhang (University of Connecticut) for highly constructive feedback during peer review, and Dylan Harp (Los Alamos National Laboratory) for helpful conversations during manuscript preparation. We acknowledge the Texas Advanced Computing Center (TACC) at The University of Texas at Austin for providing HPC resources that have contributed to the results reported within this paper.

Table 4.1 Results of manual validation at 50 cm data resolution (sites are 1 km^2).

			% of polygons by instance				*% of polygons by area*			
Site	Polygons identified	Polygonal area (%)	Whole	Fractional	Conglomerate	Non-polygonal	Whole	Fractional	Conglomerate	Non-polygonal
Utqiaġvik-1	2555	68.3	94.2	2.2	2.2	1.4	86.9	1.4	7.5	4.2
Utqiaġvik-2	2613	68.8	91.6	2.8	5.6	0.0	79.9	3.6	16.5	0.0
Prudhoe-1	3227	99.9	95.6	2.8	1.4	0.2	96.3	2.2	1.4	0.0
Prudhoe-2	4685	94.5	91.6	1.4	7.0	0.0	87.7	1.7	10.6	0.0
Prudhoe-3	1112	48.2	91.2	3.6	5.2	0.0	82.3	4.2	13.4	0.0
Prudhoe-4	1956	60.4	88.2	4.2	7.2	0.4	81.4	3.2	14.9	0.5
Prudhoe-5	2969	77.9	91.8	4.0	4.2	0	87.7	1.7	10.6	0
Prudhoe-6	1605	65.5	85.8	5.4	8.2	0.4	69.5	4.8	22.1	3.4
Prudhoe-7	1348	47.3	94.0	2.2	3.6	0.2	90.5	1.7	7.9	0.0
Prudhoe-8	3288	100	96.0	2.2	1.6	0.2	95.2	1.5	3.2	0.0

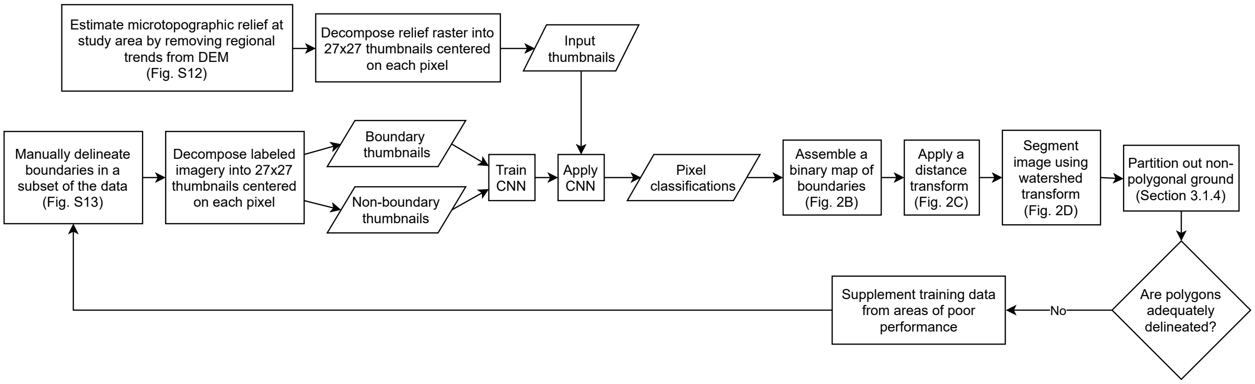

Figure 4.1

Schematic of our iterative workflow for polygon delineation.

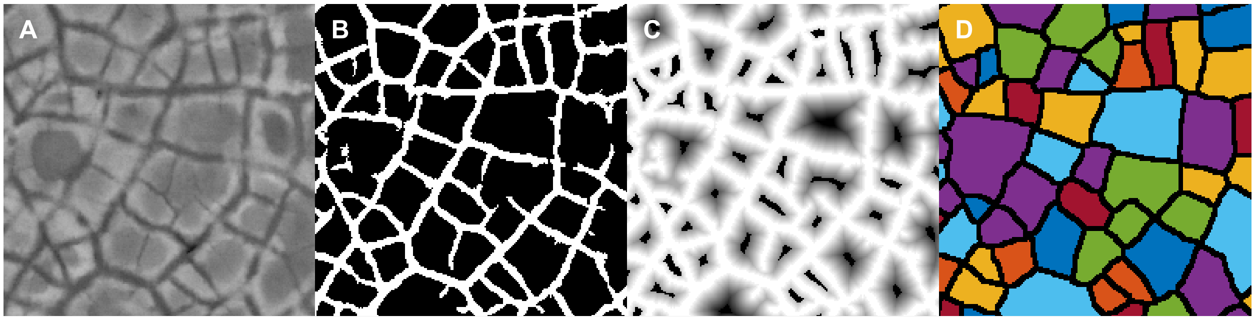

Figure 4.2

Illustration of several intermediate stages in our workflow. The CNN processes information stored in 8-bit grayscale imagery representing microtopography (A), estimated by removing regional trends from the lidar DEM (Fig S2). The CNN identifies pixels likely to represent troughs (B). Each non-trough pixel is assigned a negative intensity equal to its distance from a trough (C) and a watershed transformation is applied to segment the image into discrete polygons (D) (colors randomly applied to emphasize polygonal boundaries).

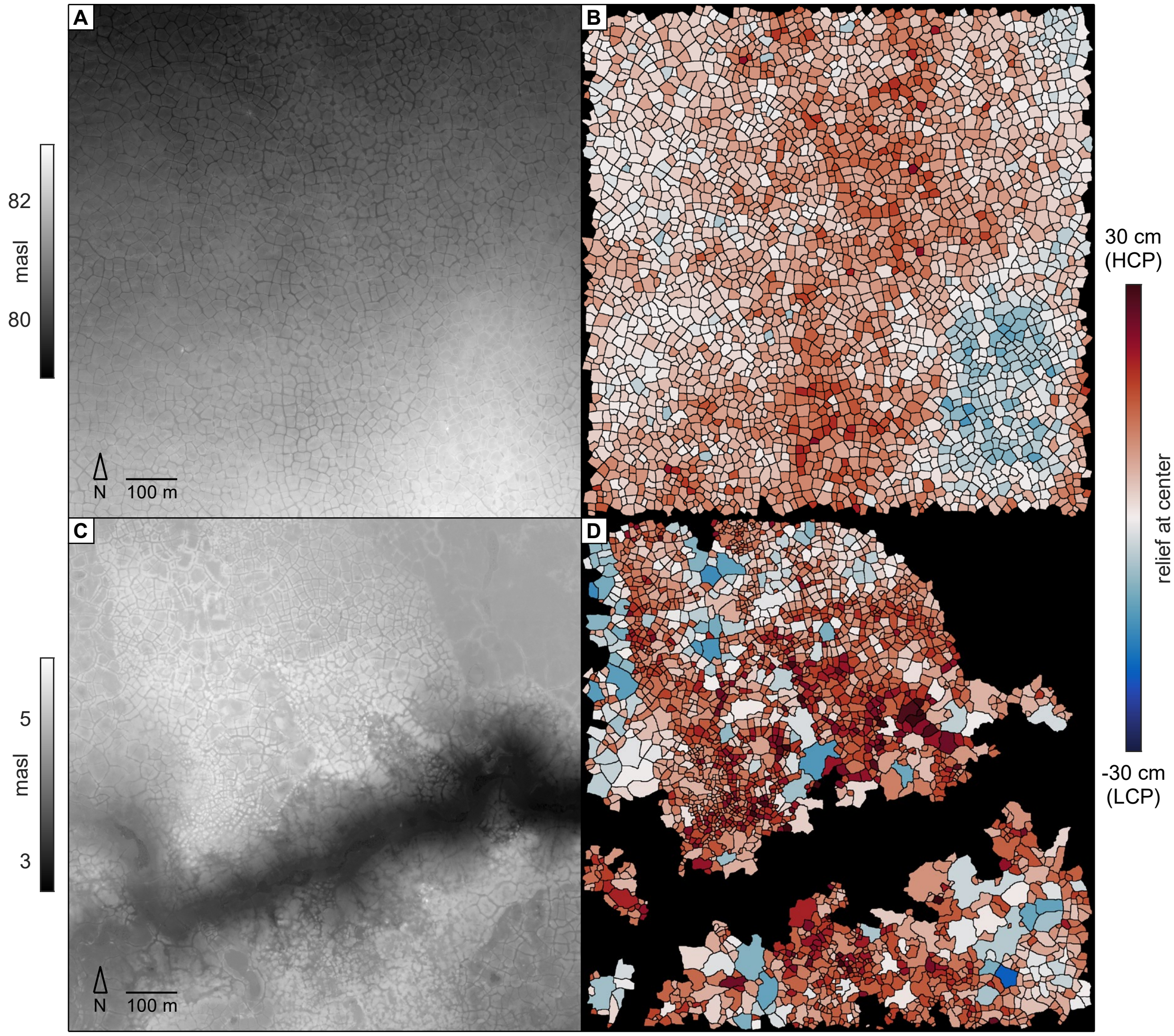

Figure 4.3

DEMs and estimates of polygonal relief at sites Prudhoe-1 (A, B) and Utqiaġvik-1 (C, D). Polygons crossing the boundaries of study sites are removed in (B, D).

REFERENCES

Abolt CJ, Young MH, Atchley AL, Wilson CJ. 2019. CNN-watershed: A machine-learning based tool for delineation and measurement of ice wedge polygons in high-resolution digital elevation models. Zenodo repository. doi:10.5821/zenodo.2537167.

Ciresan D, Giusti A, Gambardella LM, Schmidhuber J. 2012. Deep neural networks segment neuronal membranes in electron microscopy images. In: Pereira F, Burges CJC, Bottou L, Weinberger Q (eds). Advances in Neural Information Processing Systems 25, pp. 2843-2851, Curran Associates, Inc.

He K, Gkioxari G, Dollar P, Girshick R. 2017. Mask R-CNN. In: Proceedings of the 2017 IEEE International Conference on Computer Vision, IEEE.

Jorgenson MT, Shur YL, Pullman ER. 2006. Abrupt increase in permafrost degradation in Arctic Alaska. *Geophysical Research Letters* **33**: GL024960.

Jorgenson MT, Kanevskiy M, Shur Y, Moskalenko N, Brown DRN, Wickland K, Striegl R, Koch J. 2015. Role of ground ice dynamics and ecological feedbacks in recent ice wedge degradation and stabilization. *Journal of Geophysical Research: Earth Surface* **120**: 2280–2297.

Kestur R, Farooq S, Abdal R, Mehraj E, Narasipura O, Mudigere M. 2018. UFCN: A fully convolutional neural network for road extraction in RGB imagery acquired by remote sensing from an unmanned aerial vehicle. *Journal of Applied Remote Sensing* **12**: 016020.

Lachenbruch AH. 1962. Mechanics of thermal contraction cracks and ice-wedge polygons in permafrost. Geological Society of America Special Paper 70.

Lara MJ, McGuire DA, Euskirchen ES, et al. 2015. Polygonal tundra geomorphological change in response to warming alters future CO_2 and CH_4 flux on the Barrow Peninsula. *Global Change Biology* **21**: 1634-1651.

Lara MJ, Nitze I, Grosse G, McGuire AD. 2018. Tundra landform and vegetation trend maps for the Arctic Coastal Plain of northern Alaska. *Scientific Data* **5**: 180058.

Leffingwell EK. 1915. Ground-ice wedges, the dominant form of ground-ice on the north coast of Alaska. *Journal of Geology* **23**: 635-654.

Levy JS, Marchant DR, Head JW. 2010. Thermal contraction crack polygons on Mars: A synthesis from HiRISE, Phoenix, and terrestrial analogue studies. *Icarus* **226**: 229-252.

Liljedahl AK, Boike J, Daanen RP, et al. 2016. Pan-Arctic ice wedge degradation in warming permafrost and its influence on tundra hydrology. *Nature Geoscience* **9**, 312-318.

Lousada M, Pina M, Vieira G, Bandeira L, Mora C. 2018. Evaluation of the use of very high resolution aerial imagery for accurate ice-wedge polygon mapping (Adventdalen, Svalbard). *Science of the Total Environment* **615**: 1574-1583.

Paine JG, Andrews JR, Saylam K, Tremblay TA. 2015. Airborne LiDAR-based wetland and permafrost-feature mapping on an Arctic Coastal Plain, North Slope, Alaska. In: *Remote Sensing of Wetlands*, Tiner RW, Klemas VV, Lang MW (eds). CRC Press: Boca Raton, FL.

Pina P, Saraiva J, Bandeira L, Barata T. 2006. Identification of Martian polygonal patterns using the dynamics of watershed contours. In: Campilho A, Kamel M (eds). Image Analysis on Recognition, pp. 691-699, Springer-Verlag, Berlin-Heidelberg.

Pina P, Saraiva J, Bandeira L, Antunes J. 2008. Polygonal terrains on Mars: A contribution to their geometric and topological characterization. *Planetary and Space Science* **56**: 1919-1924.

Raynolds MK, Walker DA, et al. 2014. Cumulative geoecological effects of 62 years of infrastructure and climate change in ice-rich permafrost landscapes, Prudhoe Bay Oilfield, Canada. *Global Change Biology* **20**: 1211-1224.

Soille P. 2004. Morphological Image Analysis, Springer-Verlag: Berlin Heidelberg.

Ulrich M, Hauber E, Herrzschuh U, Hartel S, Schirrmeister L. 2011. Polygon pattern geomorphometry on Svalbard (Norway) and western Utopia Planitia (Mars) using high resolution stereo remote-sensing data. *Geomorphology* **134**: 197-216.

Wainwright HM, Dafflon B, Smith LJ, et al. 2015. Identifying multiscale zonation and assessing the relative importance of polygon geomorphology on carbon fluxes in an Arctic tundra ecosystem. *Journal of Geophysical Research: Biogeosciences* **120**, 788-808.

Wilson C, Gangodagamage C, Rowland J. 2013. Digital elevation model, 0.5 m, Utqiaġvik Environmental Observatory, Alaska, 2012. Next Generation Ecosystem Experiments Arctic Data Collection, Oak Ridge National Laboratory, US Department of Energy, doi:10.5440/1109234.

Xu YY, Xie Z, Feng YX, Chen ZL. 2018. Road extraction from high-resolution remote sensing imagery using deep learning. *Remote Sensing* **10**: 1461.

Zhang W, Witharana C, Liljedahl A, Kanevskiy M. 2018. Deep convolutional neural networks for automated characterization of Arctic ice-wedge polygons in very high spatial resolution aerial imagery. *Remote Sensing* **10**: 1487.

Text 4.1S Comparison of training requirements and accuracy between CNN-watershed and Mask R-CNN algorithms.

Due to differences in the training and inference procedures used by each algorithm, training data requirements and accuracy are difficult to compare directly. Nonetheless, in several aspects, performance appears to be similar. In the present study, the CNN-watershed approach is trained initially on data derived from four manually-labeled 100 m tiles, representing 0.04 km^2. This training data is supplemented with extra examples of boundary and non-boundary features, the convex hulls of which sum to ~0.07 km^2, and the trained model is extrapolated across 10 km^2. The training to application ratio is therefore ~0.011, or 1.1%. In comparison, Mask R-CNN was trained on data from 340 90 m tiles, or ~2.75 km^2, then extrapolated across ~134 km^2, resulting in a training to application ratio of ~0.020 or 2.0% (Zhang et al., 2018). In general, within the area across which the CNN-watershed approach was applied, it was less likely than Mask R-CNN to fail to detect polygonal terrain, but more prone to mistakenly aggregate multiple ice wedge polygons into a single unit. These errors were particularly common at sites characterized by transitional terrain where ice wedge polygons grade into non-polygonal ground. It is reasonable to expect such mistakes in these areas, as microtopography is typically faint and polygons often appear to be bound incompletely by troughs. At one such site (Prudhoe-6), the number of incorrect conglomerate polygons by area delineated by the CNN-watershed algorithm was ~22% (Table 4.1). This number closely resembles the 21% of human-delineated polygons estimated to go undetected by Mask R-CNN in satellite-based optical imagery (Zhang et al., 2018).

Table 4.1S Architecture of our CNN.

Layer	Type	Neurons
1	Convolutional	8 arrays of 27×27
2	ReLU†	8 arrays of 27×27
3	Max-pooling	8 arrays of 9×9
4	ReLU	8 arrays of 9×9
5	Fully-connected	64
6	ReLU	64
7	Fully-connected	2
8	ReLU	2
9	Softmax	2

† - ReLu – rectified linear unit

Table 4.2S Results of manual validation at 100 cm and 25 cm resolution.

			% of polygons by instance				*% of polygons by area*			
Site	Polygons identified	Polygonal area (%)	Whole	Fractional	Conglomerate	Non-polygonal	Whole	Fractional	Conglomerate	Non-polygonal
Utqiaġvik-1 (100 cm)	3058	74.3	73.4	18.6	6.2	1.8	65.5	16.6	13.4	4.1
Prudhoe-1 (100 cm)	3019	100	85.6	11.8	2.6	0.0	88.0	79.7	4.0	0.0
Utqiaġvik-1 (25 cm)	2870	71.6	89.0	3.8	3.4	3.8	83.4	2.0	9.7	4.8
Prudhoe-1 (25 cm)	3193	100	93.6	3.4	2.4	0.6	94.0	1.6	4.3	0.1

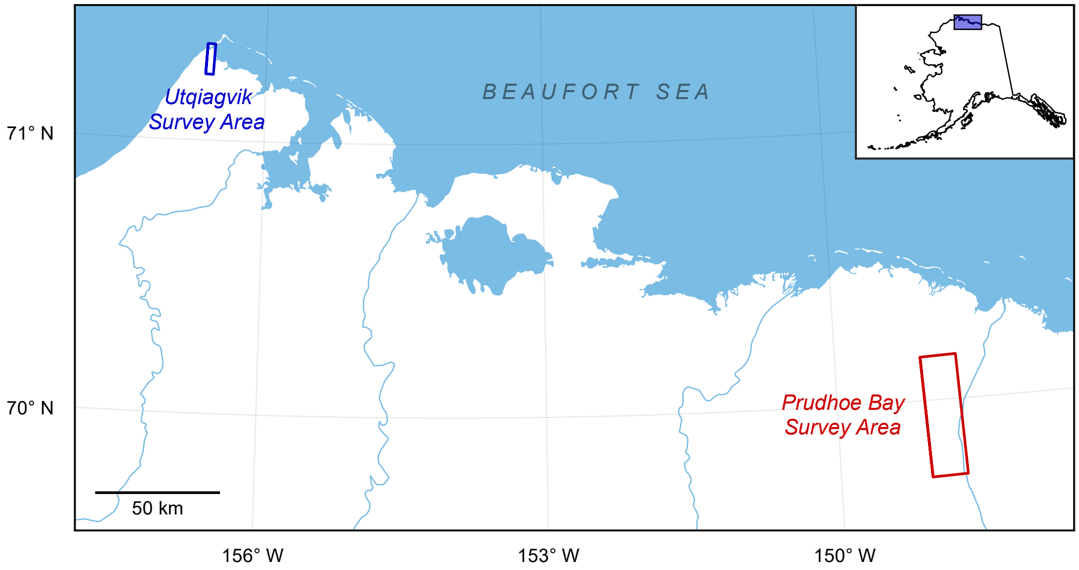

Figure 4.1S

Bounding boxes of airborne lidar surveys.

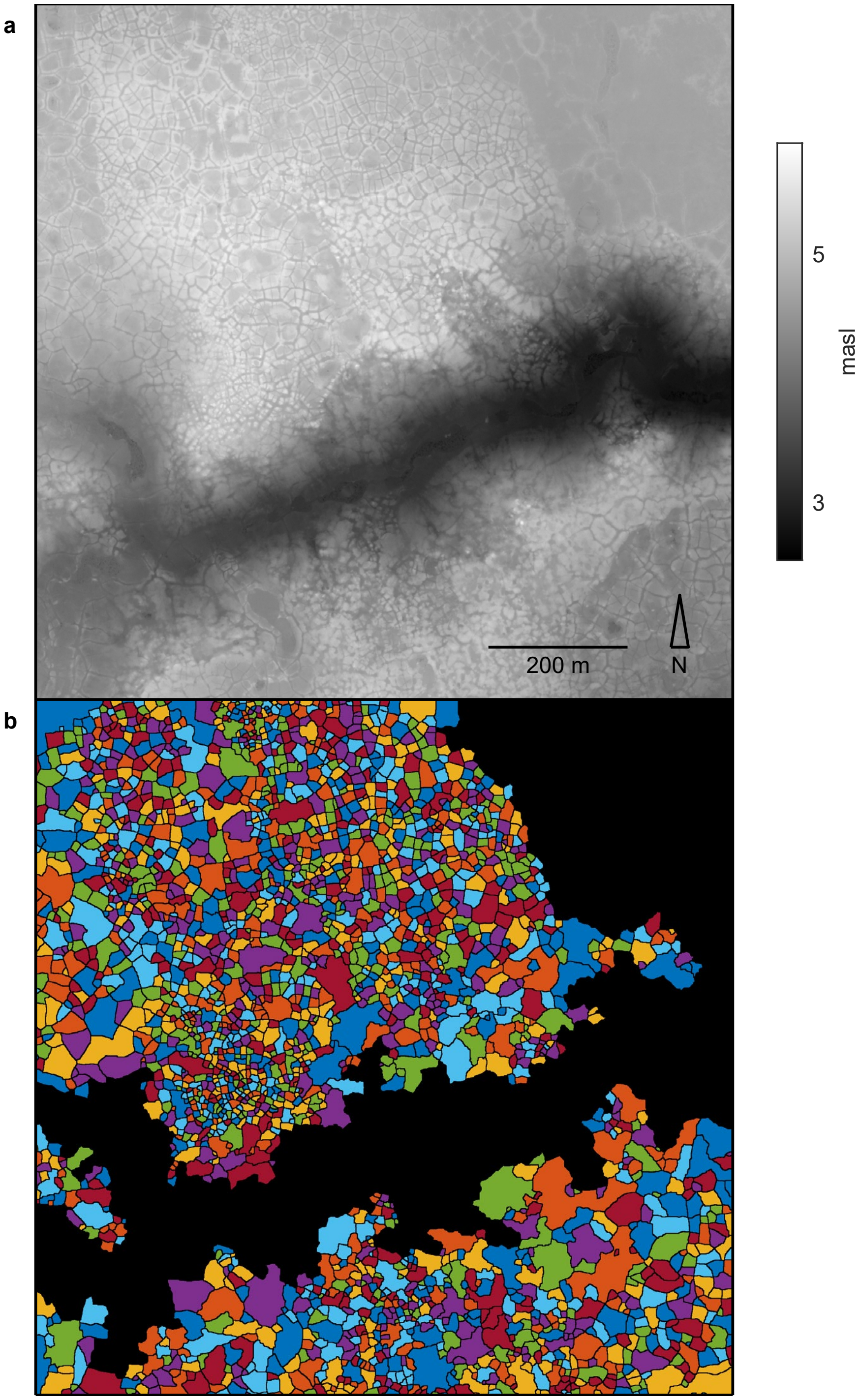

Figure 4.2S 50 cm DEM (**a**) and polygon delineation (**b**) at site Utqiaġvik-1.

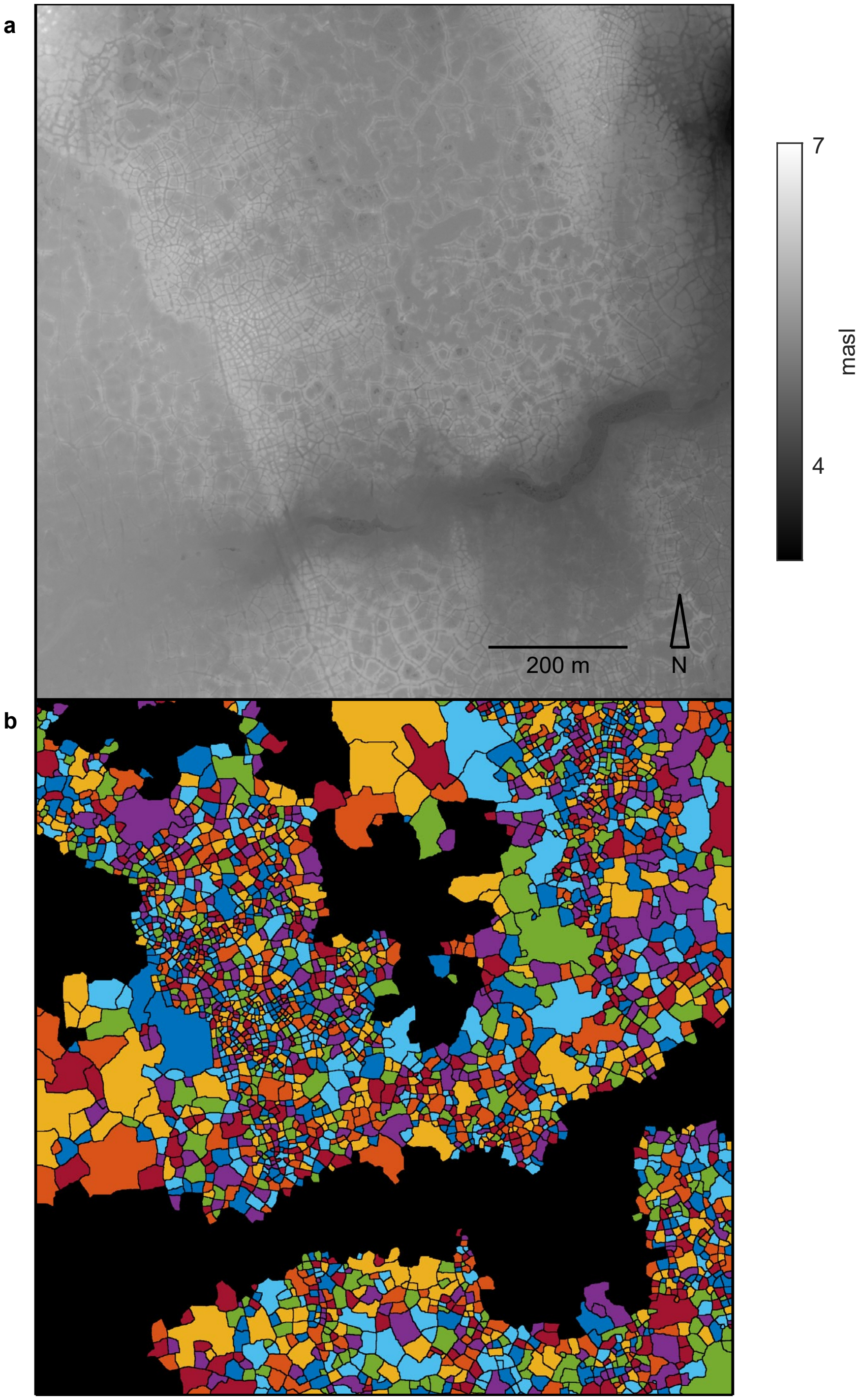

Figure 4.3S 50 cm DEM (a) and polygon delineation (b) at site Utqiaġvik-2.

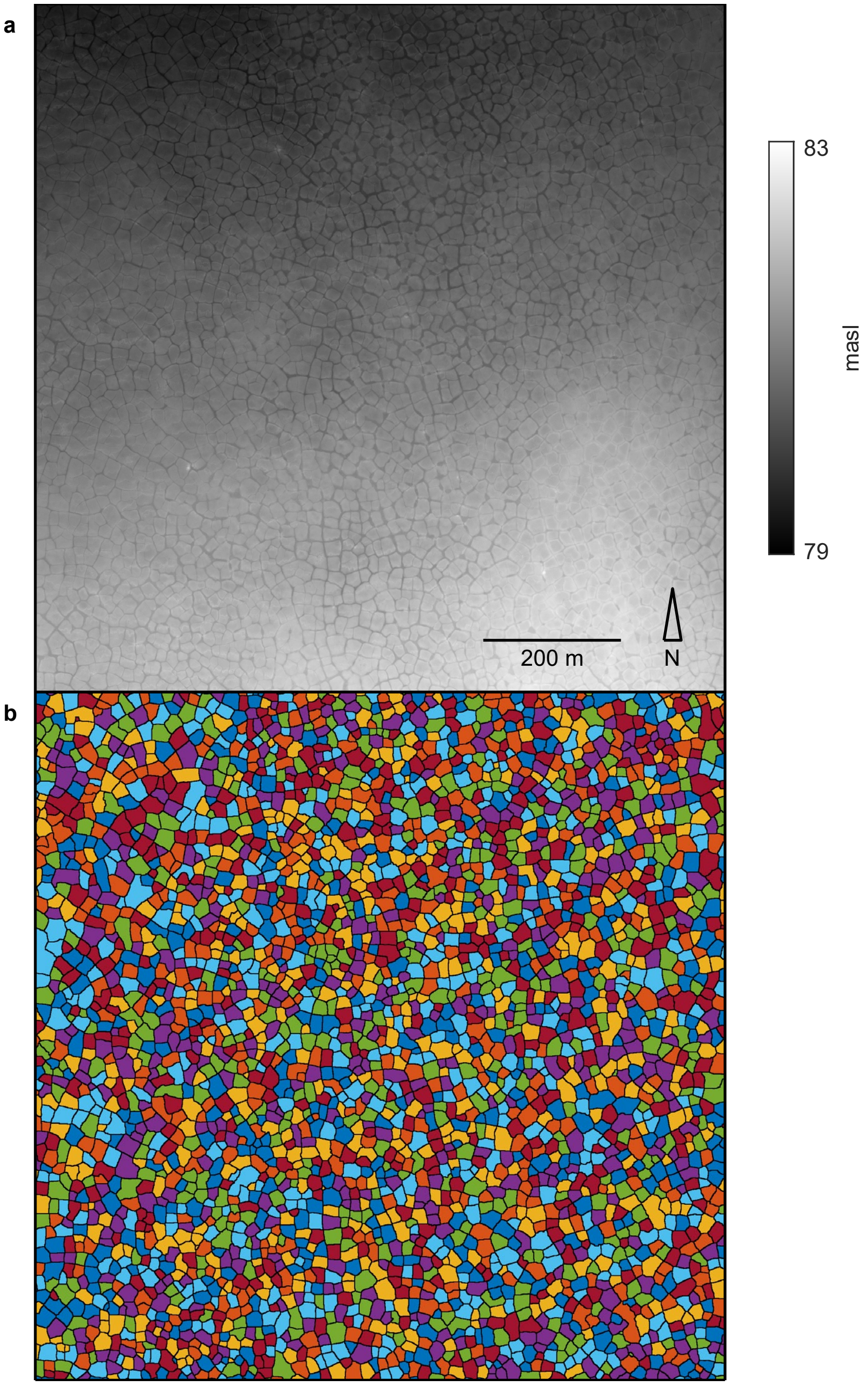

Figure 4.4S 50 cm DEM (**a**) and polygon delineation (**b**) at site Prudhoe-1.

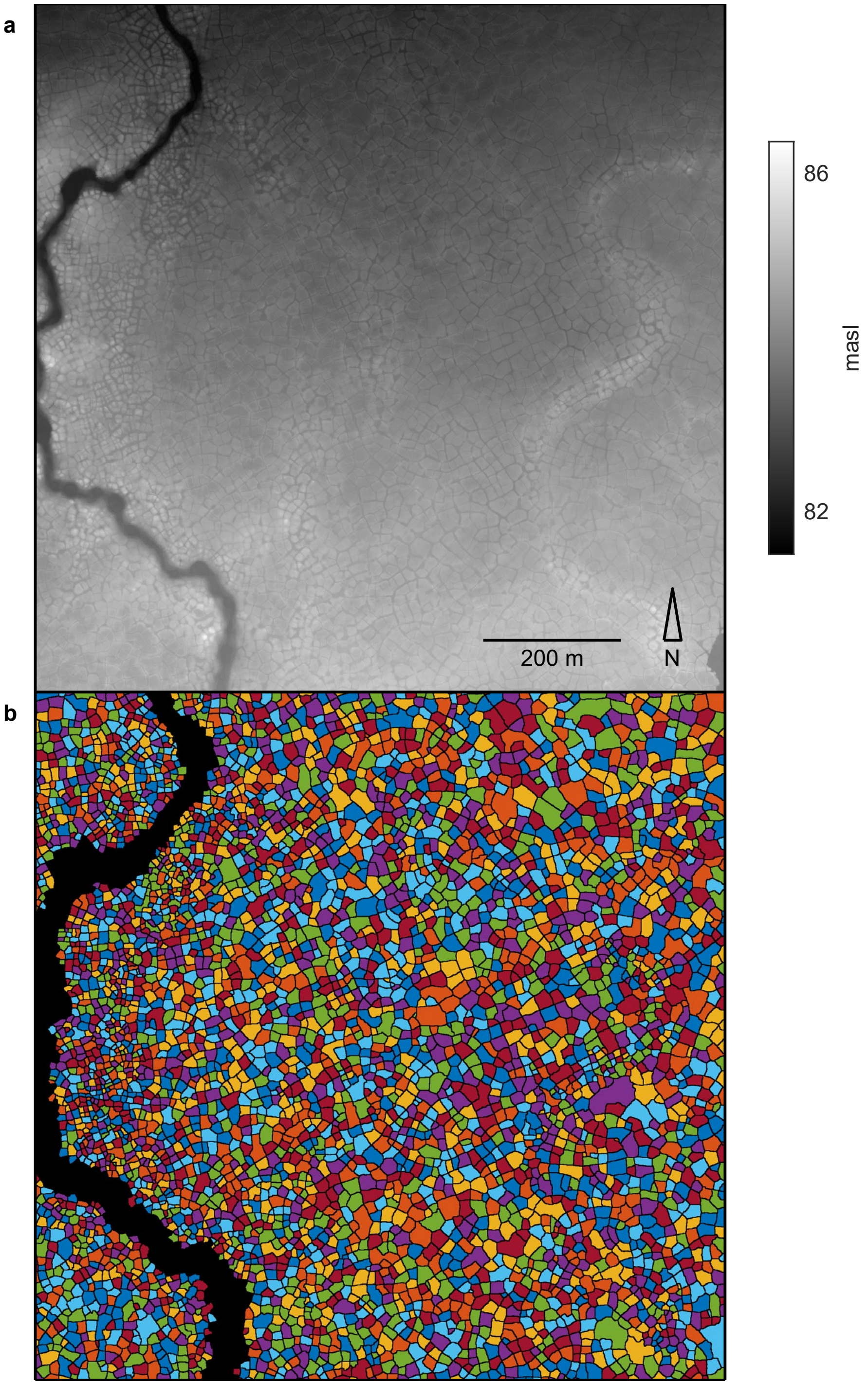

Figure 4.5S 50 cm DEM (**a**) and polygon delineation (**b**) at site Prudhoe-2.

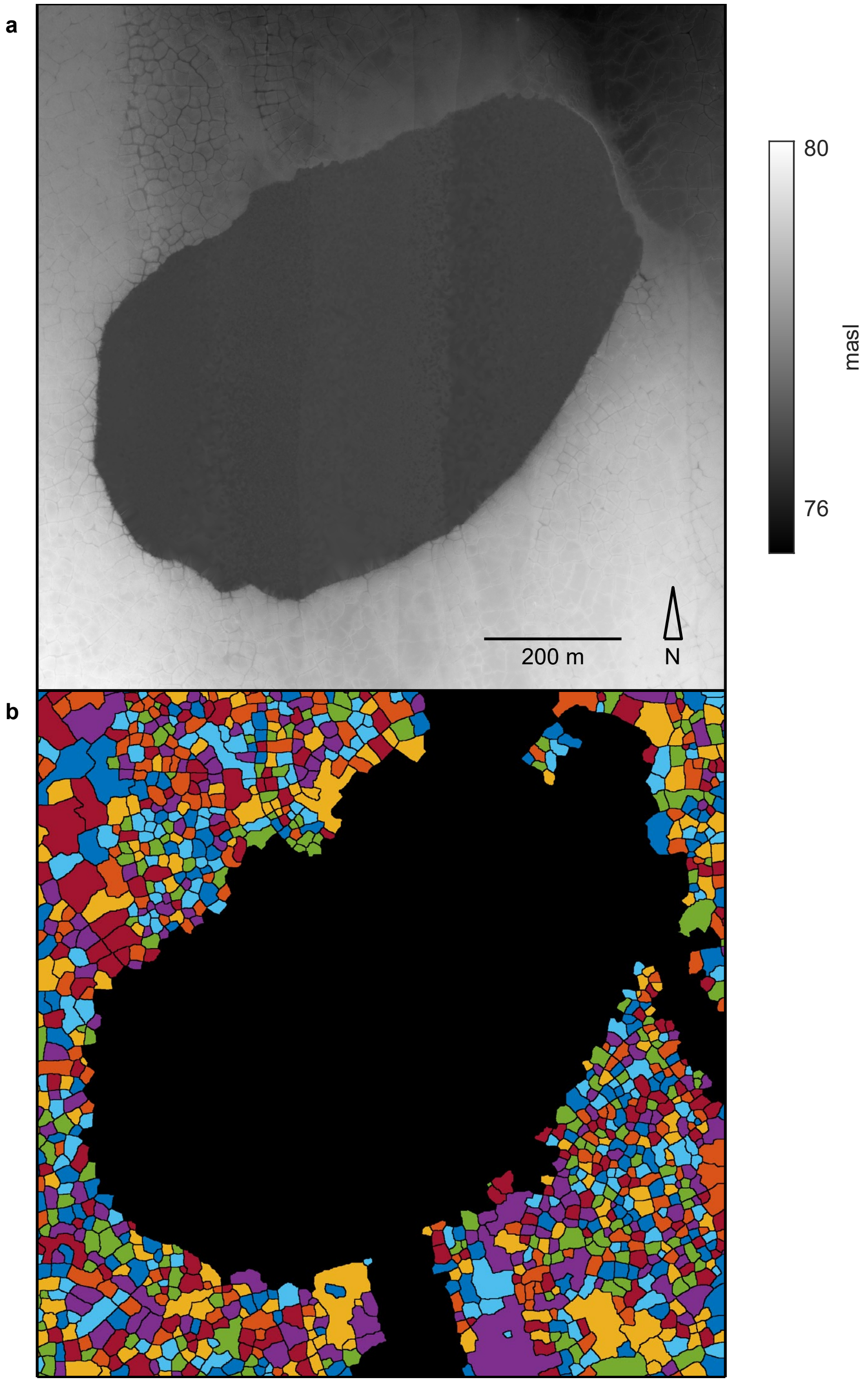

Figure 4.6S 50 cm DEM (**a**) and polygon delineation (**b**) at site Prudhoe-3.

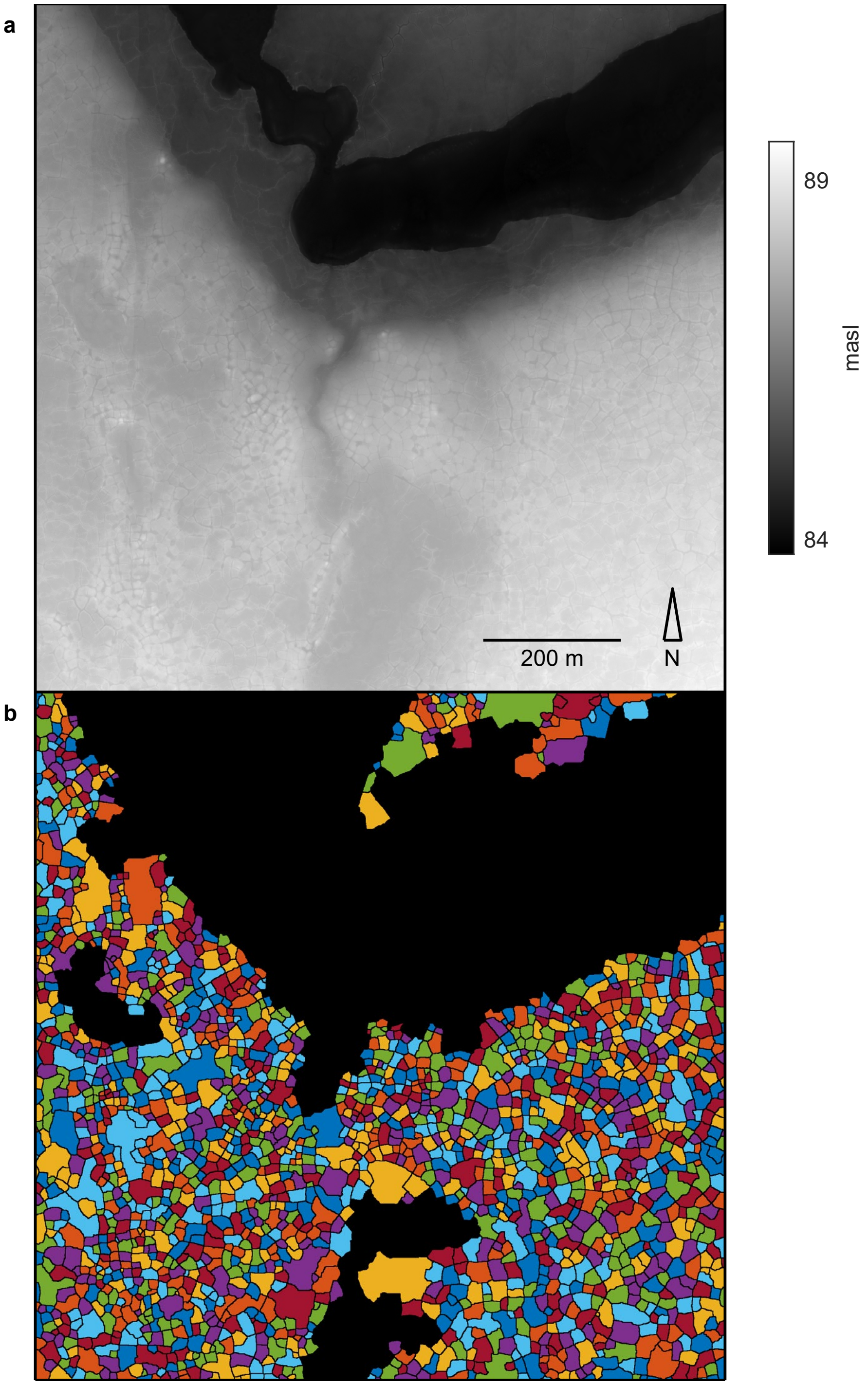

Figure 4.7S 50 cm DEM (**a**) and polygon delineation (**b**) at site Prudhoe-4.

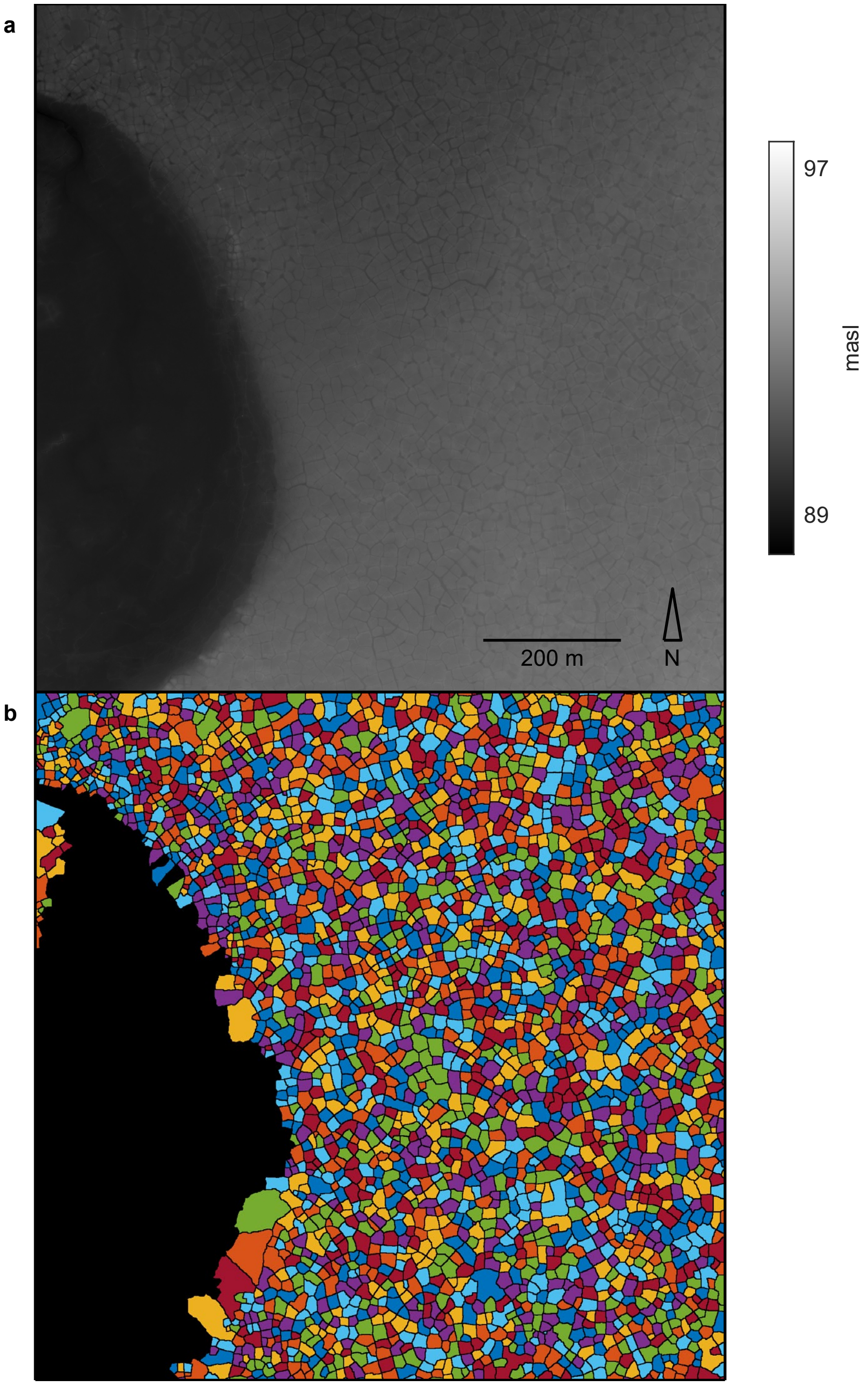

Figure 4.8S 50 cm DEM (**a**) and polygon delineation (**b**) at site Prudhoe-5.

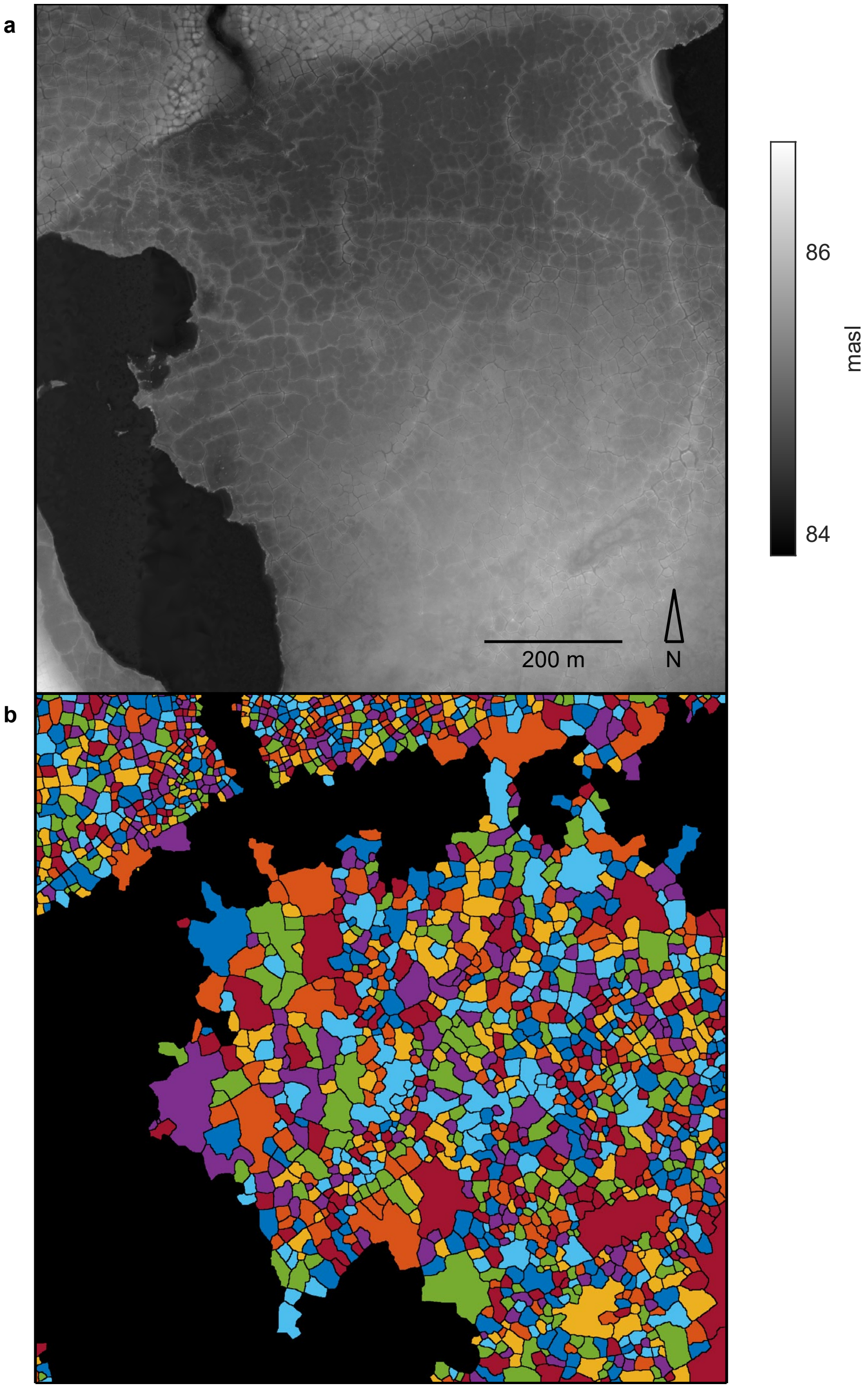

Figure 4.9S 50 cm DEM (**a**) and polygon delineation (**b**) at site Prudhoe-6.

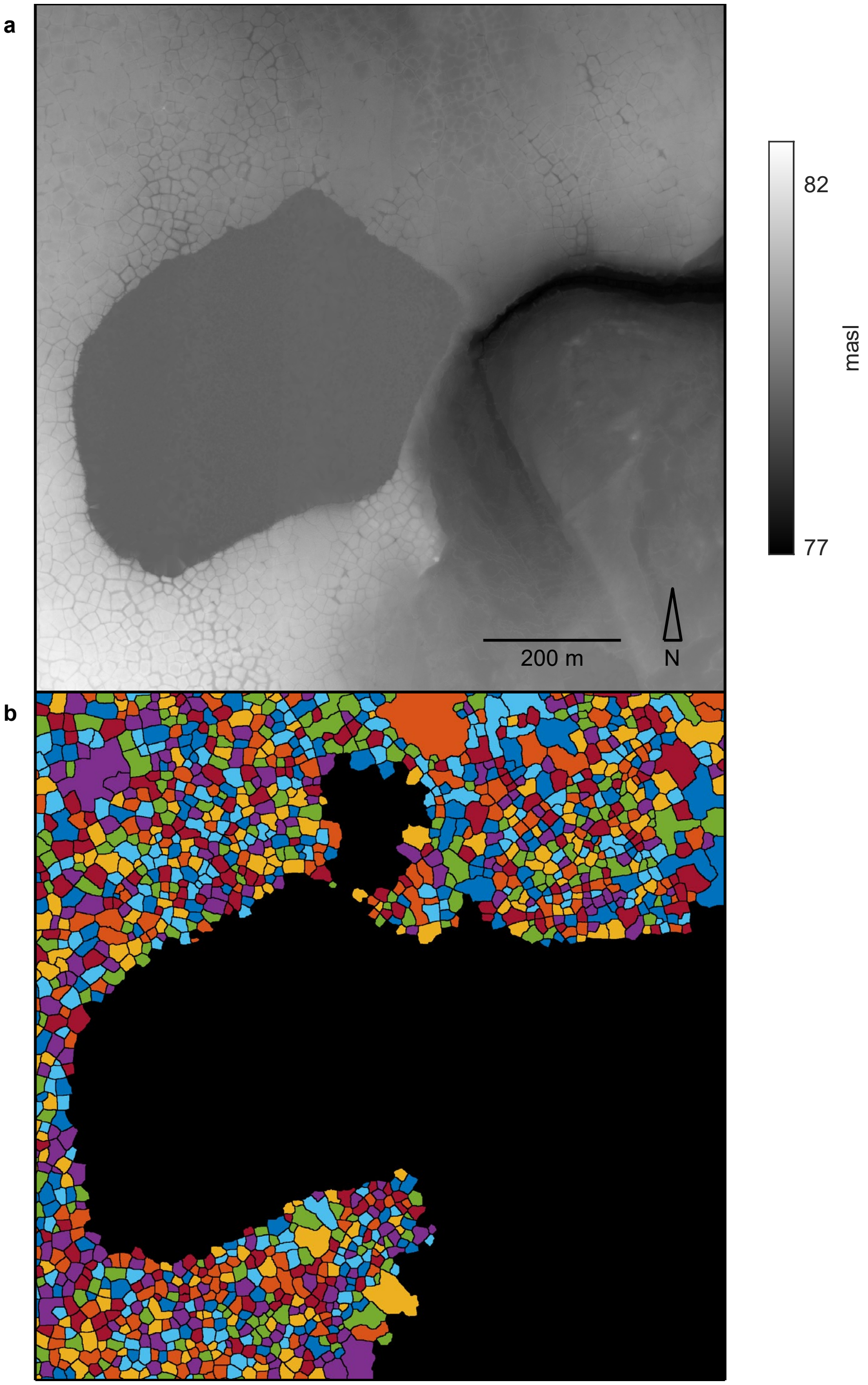

Figure 4.10S 50 cm DEM (**a**) and polygon delineation (**b**) at site Prudhoe-7.

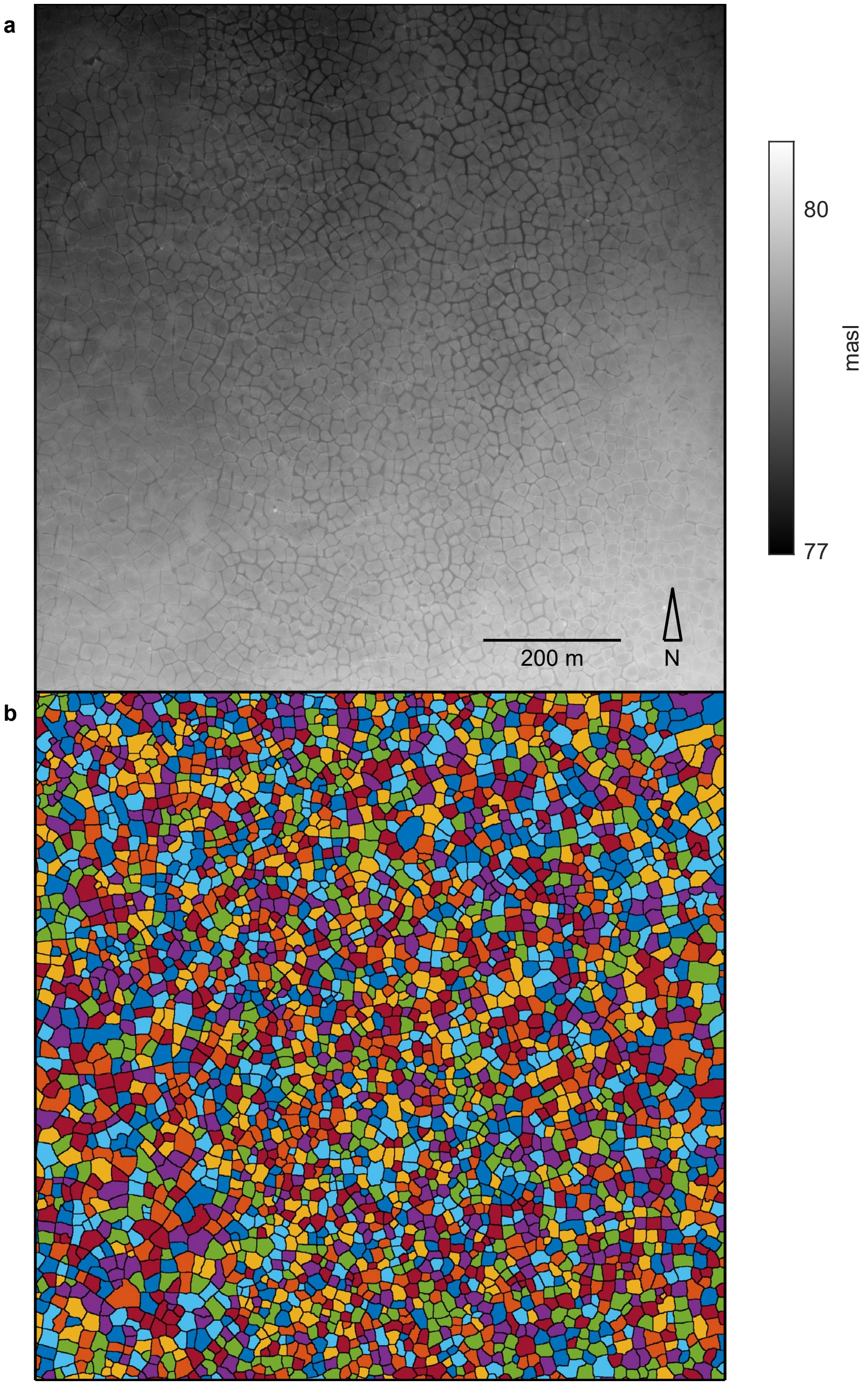

Figure 4.11S 50 cm DEM (**a**) and polygon delineation (**b**) at site Prudhoe-8.

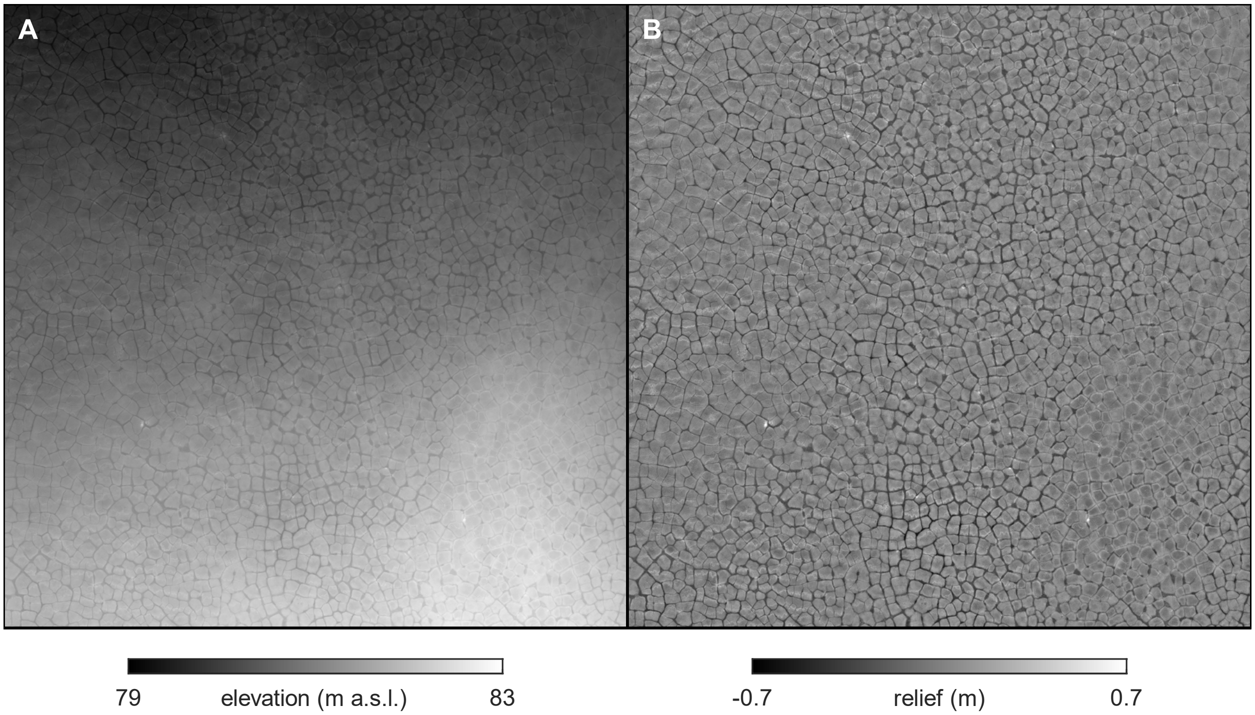

Figure 4.12S

50 cm DEM of the Prudhoe Bay training site before (**a**) and after (**b**) removing regional trends to isolate microtopography.

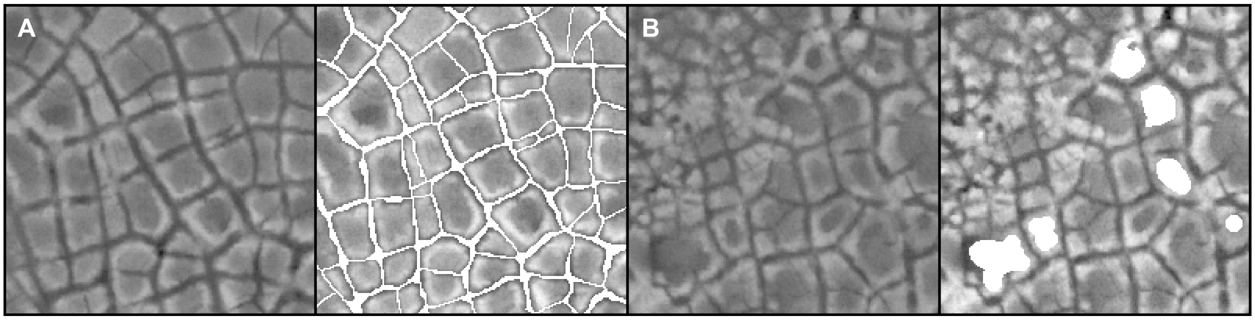

Figure 4.13S

Samples of manually delineated data used to train the CNN, including a tile in which troughs are fully delineated (**a**) and a tile used to supplement the training deck with extra examples of non-trough pixels (**b**).

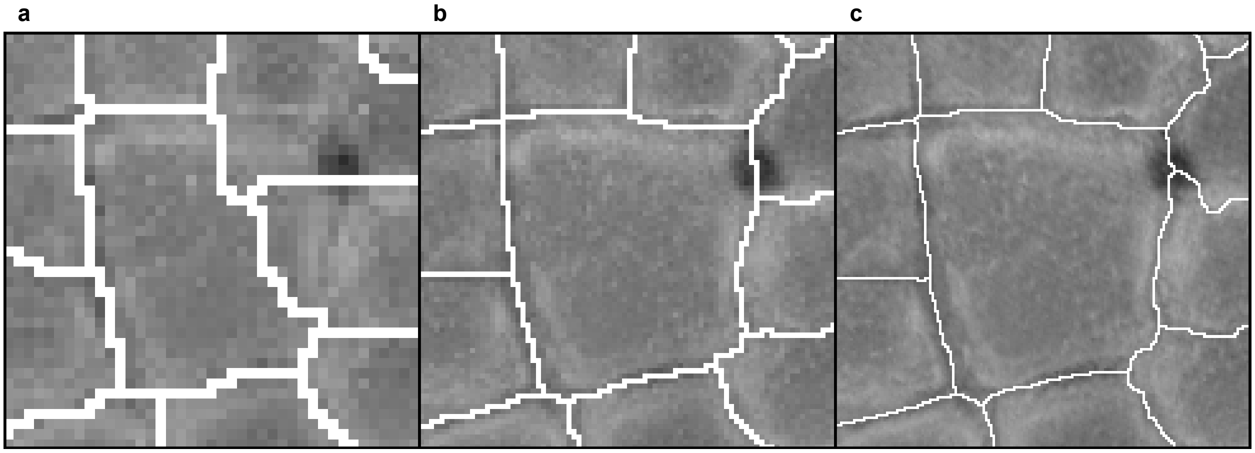

Figure 4.14S

Delineation algorithm performance on the same ice wedge polygon at 100 cm (**a**), 50 cm (**b**), and 25 cm (**c**) resolution. Each image is 40 m across. Note that anomalously low pixels in the polygon center in (**a**) are mistaken as polygon boundaries, incorrectly fragmenting the polygon.

Chapter 5: High resolution mapping of heterogeneity in ice wedge polygon geomorphology, Prudhoe Bay, Alaska

5.1 Introduction

One of the challenges to understanding Arctic feedbacks on global climate change is accounting for the influence of ice wedge polygon microtopography on mobilization of soil organic carbon. Ice wedge polygons are archetypal features of tundra landscapes, segmenting the land surface into discrete units some tens of meters across (Leffingwell, 1919; Lachenbruch, 1962). The geomorphology of ice wedge polygons plays an important role in mediating fluxes of energy (Gamon et al., 2012; Abolt et al., 2018), water (Liljedahl et al., 2011; 2016), and carbon (Olivas et al., 2011; Zona et al., 2011; Lara et al., 2015; Wainwright et al., 2015) between the atmosphere and the subsurface, as polygons often introduce conspicuous microtopography to otherwise flat terrain. This microtopography exerts complex controls on biophysical processes, which often vary on spatial scales of meters. In basin-like low-centered polygons (LCPs), for example, rims of soil raised only a few decimeters at the polygon edges tend to be better drained than the frequently inundated centers, driving pronounced gradients in photosynthetic activity, aerobic respiration, and methanogenesis (Zona et al., 2011). Although such fine-scale heterogeneity is well-documented in ground-based studies, accounting for its influence on carbon fluxes at spatial scales relevant to global climate processes remains a major challenge (Schuur et al., 2015). The difficulty of this upscaling is compounded by the transient nature of the microtopography itself, which often deforms in response to increased ground temperatures (Jorgenson et al., 2006; 2015).

Thus far, most efforts to account for the effects of microtopographic variability on carbon fluxes have taken a bottom-up approach, estimating local (*i.e.*, point-scale to plot-scale) gas exchange using gas flux chambers (Zona et al., 2011; Olivas et al., 2011; Lara et al., 2015; Wainwright et al., 2015), eddy covariance towers (Sturtevant et al., 2012; Sturtevant and Oechel, 2013), or a combination of *in-situ* gas sampling with numerical modeling of turbulent boundary layer mixing (Martin et al., 2018). Generally, efforts to extrapolate such measurements across greater spatial and temporal scales have followed some variant of a two-step method, in which: 1) the present day landscape is segmented into various landcover classes, such as LCPs, high-centered polygons (HCPs), and trough ponds, with each class represented by local observations; and 2) an attempt is made to forecast trends in the area represented by each landcover class over the next several decades, such as decreases in LCP terrain and increases in HCPs and trough ponds. Among other sources of uncertainty, this approach relies on the assumptions that: 1) point- or plot-scale observations of gas fluxes are representative of larger landscape units, 2) landscape evolution will follow a particular trajectory, and 3) future carbon fluxes from any particular landcover class will be similar to present fluxes.

In the last ten years, findings from the bottom-up approach have varied markedly at spatial scales varying from meters to kilometers. For example, while one investigation found that spatial heterogeneity in aerobic and anaerobic respiration at the sub-polygon level (*e.g.*, between LCP rims and centers) can exceed variability among polygon types (*e.g.*, between LCPs and HCPs) (Zona et al., 2011), a subsequent study at a different field site reached precisely the opposite conclusion (Wainwright et al., 2015). At the landscape scale, most studies predict that ice wedge-related thermokarst will drive greater emissions of CO_2 and CH_4 to the atmosphere over the next century, but some work suggests that the tundra will continue to act as a net carbon sink, perhaps more strongly than it does today (Lara et al., 2015).

One prominent source of uncertainty in these prior investigations is that the study sites are not necessarily representative of the broader tundra landscape, but tend to concentrate on ice wedge polygons within drained lake basins—a landform that is nearly ubiquitous to tundra regions of North America and Siberia, but only represents 20-45% of the land surface at regional scales (Hinkel et al., 2013). Another source of uncertainty is related to projected trends in the fraction of the land surface occupied by inundated troughs, or themorkast pools. While nearly all previous investigations suggest that changes in the abundance of trough ponds will influence regional carbon fluxes—one study, for example, indicates that such ponds may emit three times more CO_2 and seventeen times more CH_4 than drained troughs (Martin et al., 2018)—there is no consensus that ice wedge degradation will permanently increase the scale of inundation. In particular, while it is well-established that early to mid-stages of ice wedge degradation tend to drive the expansion of thermokarst pools (Jorgenson et al., 2006; 2015), it has increasingly been documented that late stages of thermokarst may trigger the abrupt elimination of surface water, as the improved connectivity of subsiding troughs enhances landscape-scale drainage (Liljedahl et al., 2016; Kanevskiy et al., 2017).

Recently, the deployment of airborne and spaceborne sensors for estimating atmospheric CO_2 and CH_4 concentrations has permitted an alternative, top-down approach to estimating carbon fluxes on the tundra. Operating from 2012-2015, NASA's Carbon in Arctic Reservoirs Vulnerability Experiment (CARVE) comprised a series of several hundred flights across the Alaska North Slope, on an airplane equipped with a downward-pointed spectrometer designed to estimate air-column fractions of CO_2 and CH_4, and a sampling chamber designed to make *in situ*, point-scale observations of atmospheric composition several times a minute in flight (Miller and Dinardo, 2012). Launched in 2014, the Orbiting Carbon Observatory 2 (OCO-2) satellite likewise hosts a spectrometer tailored to estimate air-column fractions of greenhouse gases, with a ground footprint of ~3 km^2 (Crisp et al., 2015). Since the end of the CARVE mission, observations from the aircraft have been interpreted through inverse simulations of a high-resolution weather model to infer surface sources and sinks of carbon at a spatial resolution of 0.25°× 0.25° (Henderson et al., 2015). NASA aims eventually to conduct a similar analysis of measurements from OCO-2, releasing global maps of land-surface gas fluxes at a resolution of 4° × 5°. However, the interpretation of such data products in relation to ice wedge polygon geomorphology is currently inhibited by a paucity of geospatial products quantifying polygonal form over wide spatial scales. A significant advance toward addressing this gap was recently made when Lara *et al.* (2018) released a map of estimated landcover class across the Alaska North Slope at 30 m resolution, dividing the tundra primarily into LCPs, HCPs, and flat-centered polygons (FCPs) using spectral data from the Operational Land Imager on the Landsat 8 satellite. The dataset comprises a geospatial catalogue of polygonal class across an unprecedentedly large region; however, polygon-level heterogeneity within and among classes in factors such as area, relief, and trough inundation are impossible to estimate, as the map was inferred through spectral analysis of pixels larger than typical ice wedge polygons.

Here, we take the next step toward closing the gap in spatial scales between bottom-up and top-down approaches to estimating carbon fluxes in polygonal terrain, using a high-resolution, lidar-derived digital elevation model (DEM) to delineate and measure the microtopography associated with ~10^6 discrete ice wedge polygons across an ~1,000 km^2 region of tundra on the Alaska North Slope. The dataset offers an unprecedented quantitative summary of polygon-level geomorphology over a broad landscape characteristic of the Arctic Coastal Plain. Complementing the map of individual polygons, we also infer the distribution of surface water on the tundra and map the occurrence of thaw ponds using return signal intensity data from the lidar sensor. Employing these datasets, we address questions of the degree to which ice wedge polygons within drained thaw lake basins—on which most previous field studies concentrate—are representative of the broader tundra; the level of heterogeneity in terms of relief, trough inundation, and area within previous classifications of the surface as LCP, HCP, or FCP; and where trough ponds are most abundant. In the future, we anticipate the datasets will be useful for selecting representative field plots for bottom-up approaches to estimating carbon fluxes, and for attributing causes of spatial heterogeneity in equivalent estimates from top-down methods. Among other applications, the datasets also present a unique opportunity to quantify contemporary rates of microtopographic deformation across a broad landscape, should additional airborne lidar surveys be conducted in the coming years.

5.2 Study area and data acquisition

The airborne lidar survey area comprises 1042 km^2 in northern Alaska, USA, centered ~60 km south of Prudhoe Bay (Figure 5.1). The site is roughly bounded by the Sagananirkok River to the east and the Kuparuk river to the west, and falls within the Arctic peaty lowlands ecological landscape, which occupies approximately half of the Arctic Coastal Plain (Jorgenson and Grunblatt, 2013). Soil pits excavated in the region indicate that, throughout most of the site, surface sediments are capped with ~1-3 m of Pleistocene-aged aeolian silts, grading upward into a mantle of peat some tens of centimeters thick, which has developed over the last several thousand years (Walker and Everett, 1991; Rawlinson, 1993). These silts overlie several meters of coarse alluvial sands and gravels, deposited by ancient braided streams carrying sediments northward from the Brooks Range mountains (Shur et al., 2014). Typifying the broader coastal plain, the study area contains hundreds of shallow thaw lakes, generally less than 5 m deep, and ranging in area from ~1 ha to 1 km^2. Interspersed among these modern lakes, the site also contains >100 instances of ancient thaw lake basins that have drained in the last 10,000 years, leaving shallow valleys in the modern land surface, in which the original fluvial sediments often are reworked and capped with lacustrine silts (Jorgenson and Shur, 2007). Throughout the survey area, vegetation is generally low-lying and homogeneous, consisting primarily of grasses and sedges.

The acquisition of lidar data occurred in two phases, during August 2012 and August 2014. The primary laser pulsing system on the lidar instrument (Chiroptera, Airborne Hydrography AB) operated within the near-infrared spectrum (1064 nm) at a frequency of 400 kHz (a second pulsing system fired at 38 kHz operated at 515 nm to measure bathymetric profiles of surface water bodies). Deployed in an aircraft at a nominal altitude of 400 m, it generated a point cloud representation of the land surface with an average return density greater than 20 points m^{-2}. These data were rasterized into a 50 cm horizontal resolution DEM, in which vertical and horizontal accuracies were estimated at 10 cm or less (Paine et al., 2015) (Figure 5.1a). Complementing the DEM, a 50 cm resolution raster of return signal intensity was also generated and used to infer the presence of surface water (discussed in next section).

For the purposes of our geospatial analysis, we loosely followed the approach of Jorgenson and Shur (2007), dividing the land surface in our survey into several units (Figure 5.1b). These included: 1) open water; 2) drained thaw lake basins; 3) the primary surface, or interstitial tundra, comprising old fluvial sediments unaffected by ancient thaw lakes; 4) exposed alluvial sands and gravels, associated with modern braided streams; and 5) the flood plain of the Sagavanirktok River, a peat-mantled unit that extends from the exposed modern gravels to a prominent terrace 1-3 km west of the stream. Boundaries for the Kuparuk River and Sagavanirktok River alluvial sands and gravels were modified from Jorgenson and Grunblat (2013), while drained thaw lake basins and the floodplain of the Sagavanirktok River were outlined manually using Google Earth imagery and the lidar DEM.

5.3 Map generation and geospatial analysis

5.3.1 Mapping the occurrence of ice wedge polygons

Ice wedge polygons were delineated within the DEM using a novel, deep learning-based approach presented in Abolt et al. (2019), which is briefly summarized here. At its core, the method relies on a classification tool known as a convolutional neural network (CNN) to identify pixels representing polygon boundaries within the DEM. Conceptually, a CNN is a tool used to assign a label (*e.g.*, ‘dog’, or ‘cat’) to an image. Loosely inspired by the visual cortex of the human brain, a CNN develops its own classification criteria during training by “studying” a set of manually labeled images provided by the user. Our CNN was designed to operate individually on each pixel of a DEM, treating a 27 × 27 pixel (13.5 × 13.5 m) neighborhood surrounding the pixel as a grayscale image, and classifying the pixel as either a polygon boundary (*i.e.*, a trough between adjacent polygons) or not a boundary. A set of common image processing techniques was then employed to segment the DEM into discrete polygonal units, using the boundary pixels identified by the CNN for guidance (Figure 4.2, Section 4.3.1.3). Following image segmentation, any units greater than 5,000 m^2, a threshold arbitrarily larger than most real ice wedge polygons, were assumed to represent patches of non-polygonal ground and were eliminated. Units in the exposed alluvial sand and gravel landscape were also eliminated, as polygonal relief rarely forms in these sediments, but pits between bars were frequently mistaken by the CNN for troughs.

We generated the training data for our CNN by manually classifying pixels from the DEM as either "boundary" or "non-boundary" using a basic raster graphics editor. The training deck of images consisted of 27 × 27 pixel grayscale images centered on these labeled pixels, which were derived primarily from four plots, each 1 ha, dispersed across the survey area. Every pixel within these plots was assigned one of the two classes. Supplementing the data from these primary plots, additional instances of "boundary" and "non-boundary" pixels were added from smaller regions elsewhere in the survey area; the convex hulls of these extra features summed to ~10.5 ha. The training data thus represented ~14.5 ha of terrain, or ~0.015% of the survey area. Training was conducted on a personal laptop with a single NVIDIA MX150 graphics processing unit (GPU). In less than 30 minutes of processing, the CNN classified the training deck of images with >98% accuracy.

The polygon delineation algorithm was executed on an HPC cluster at the Texas

Advanced Computing Center using four NVIDIA K-40 GPUs and required approximately eight hours of processing time. Following delineation, the accuracy of the map was estimated through manual validation using the same technique as Abolt et al. (2019). 5,000 polygons from across the survey area were randomly selected for inspection, and each was classified as either: whole; fragmentary (*i.e.*, occupying less than 90% of a real ice wedge polygon); conglomerate (composed of multiple real polygons); or false (occupying non-polygonal terrain). The results of this validation were tabulated at large across the study area and by landscape unit.

5.3.2 Detection of thermokarst pools

Thermokarst pools, in the form of flooded troughs, were mapped exploiting observations of return signal intensity associated with each point in the lidar dataset. Because water is strongly absorbing of near infrared radiation, surface water bodies in imagery derived from the return intensity data were starkly apparent as dark objects in relation to bare tundra (Figure 5.2a). Unfortunately, at large spatial scales, a simple thresholding operation to extract these bodies proved to be impractical, as the return intensity signal tends to drift throughout the survey area—a trend that has been attributed in other surveys to fluctuations in plane altitude and the energy emitted by the laser pulsing system (Garroway et al., 2011). However, we found that thermokarst pool mapping was amenable to pixel-by-pixel processing using a CNN, following the workflow described in the previous section for classifying DEM pixels as polygon boundaries and non-boundaries. Accordingly, we trained a second CNN with similar neural architecture to the first using 38 ha of return intensity data at 50 cm horizontal resolution, in which each pixel was classified manually as surface water or bare tundra (Figure

5.2b). All bodies of surface water less than 1 ha extracted through these means were treated as thermokarst pools. Manual validations were performed on 200 instances, to classify each result as true or false.

5.3.3 Estimation of ice wedge polygon attributes and statistical analysis

To characterize spatial heterogeneity in polygon geomorphology, a series of attributes were assigned to each delineated polygon, including centroid location in UTM coordinates, area, mean elevation, relief at the polygon center, and percent coverage by thermokarst pools. Relief at the polygon center was used as a proxy for LCP, HCP, or FCP status, and was estimated using a simple method. First, a distance transform was employed to assign each pixel within a polygon a number equal to its Euclidean distance from the closest boundary; the pixels were then split at the median value, dividing the polygon evenly into an exterior, ring-shaped zone and an equally sized interior zone. Relief was defined as the difference in mean elevation between the inner and outer zones, omitting any pixels identified as a thermokarst pool from the calculation. Percent coverage by thermokarst pools (which tended to occupy troughs at the polygon boundaries) was calculated by simply dividing the area of thermokarst pools overlapping each polygon by the total area of the polygon.

The statistical analysis was designed primarily to determine the degree to which polygons within drained thaw lake basins are representative of the broader tundra, and the level of heterogeneity among LCPs, FCPs, and HCPs, in terms of polygonal relief, polygonal area, and percent coverage by thermokarst pools. Toward the first objective, empirical distributions of polygonal relief, area, and percent coverage by surface water were calculated for polygons within drained thaw lake basins and for all polygons at large across the survey area. Because the distributions tended to be non-normal, a nonparametric Kolmogorov-Smirnov test was used to evaluate the null hypothesis that polygons within drained thaw lake basins were representative of the broader landscape in each statistic. Toward the second objective, each polygon in the survey area was assigned a nominal class of HCP if center relief was greater than 5 cm, FCP if center relief was between -5 and 5 cm, and LCP if center relief was less than -5 cm. Empirical distributions of area and percent inundation were calculated for each of these classes. Variation among polygon classes and landscape units was quantified using a Kruskal-Wallis test. Finally, the percent coverage of the land surface by ice wedge polygons was tabulated by landscape unit, and the map was inspected visually for qualitative patterns in polygon geomorphology.

5.4 Results and discussion

Throughout the study area, we delineated a total of 1,056,856 polygons, representing an average density of ~1,000 polygons km^{-2} and a total area of ~314.08 km^2. Polygonal terrain thus comprises ~30% of the site, or ~34% of the tundra surface, after excluding exposed alluvial sands and gravels and water bodies larger than one hectare. Ice wedge polygons are irregularly, but broadly, dispersed across the landscape (Figure 5.3). Overall, the spatial distribution of our results is comparable to a mapping conducted by Zhang et al. (2018), who delineated polygons across a ~134 km^2 landscape using visual imagery; in their study, total area was not reported, but polygons were detected at an average density of ~1,200 polygons km^{-2}. As in the Zhang study, the fraction of our site occupied by identifiable polygons likely underestimates the area affected by ice wedges, which often form a polygonal network at the top of the permafrost without a clear reflection in surface topography. In recent years, it has become common for such terrain throughout the Arctic to develop into HCPs, as thaw penetrates the tops of the ice wedges, spurring the formation of new troughs (Liljedahl et al., 2016; Jorgenson et al., 2018; Saito et al., 2018). This process may be incipient throughout much of the tundra mapped as non-polygonal at our survey area, as a sparse occurrence of ice wedge trough segments was frequently detected in the DEM, but individual segments failed to interconnect and divide the ground surface into discrete polygons.

In general, our mapping of polygon boundaries was very accurate. Across the study area at large, ~91% of polygons inspected manually were correctly delineated (Table 5.1). The accuracy was somewhat lower on the floodplain of the Sagavanirktok river, where polygonal microtopography was somewhat muted, and ~79% of mapped polygons had accurate boundaries. Among all landscape units, errors were roughly evenly divided into fractional polygons, falsely identified polygons among non-polygonal terrain, and conglomerations of several real polygons into a single unit, implying that the algorithm is not clearly biased toward either over-detection or under-detection of polygon boundaries. A set of two-sample Kolmogorov-Smirnov tests failed to detect differences between incorrectly mapped polygons and the entire population of polygons in estimates of relief at the center ($p = 0.81$), area ($p = 0.41$), or percent coverage by open water ($p = 0.84$) at the 5% significance level, indicating that these errors are unlikely to significantly impact the empirical distributions of these processes. Instances of clearly polygonal ground that went undetected by our algorithm were rare in terms of the total area affected, but tended to occur in linear swaths, where centimeter-scale divergence in estimated elevation from overlapping flight lines of the airborne survey introduced random noise into the DEM, obscuring polygonal boundaries.[3]

Our second CNN, trained to detect of thermokarst pools using lidar return intensity data, was also very accurate. Among the 200 ponds used for manual validations, 96% were deemed to represent real open water surfaces. False positives again occurred in sites of high noise associated with overlapping flight lines. Where bodies of open water overlapped ice wedge polygons, the vast majority (>95%) were found along the troughs at polygon boundaries, representing true thermokarst pools. However, small ponds within LCP centers were occasionally detected as well. These ponds were thus included in the calculation of percent coverage by thermokarst pools assigned to each polygon.

Qualitatively, the spatial distribution of polygonal ground at our site is highly uneven, with the greatest density of polygons occurring in the southeastern portion of the site, just west of the terrace that separates the primary surface from the floodplain of the Sagavarnirktok River (Figure 5.3b). Here, an especially high concentration of HCPs, closest to the floodplain, grades relatively smoothly westward into terrain dominated by LCPs. At the spatial scale of tens of meters, this gradation is sporadically interrupted by clusters of HCPs adjacent to sites of enhanced surface drainage, such as streams or the upgradient shores of thaw lakes. In the center of the survey area, well-developed polygons are sparse, despite the tundra being pockmarked by occasional ice wedge troughs; while in the northern half, extensive polygonal development is punctuated by a high density of streams and ponds. The very high spatial resolution of our

---

[3] We estimate this error affected mapping of less than 5% of the polygonal ground at the site, and anticipate that it will be resolved in the near future through additional post-processing of the lidar data.

mapping permits visualization of this heterogeneity in the land surface with unprecedented detail. Viewed across a spatial scale of kilometers, our map reveals subtle variation in polygonal relief, shape, and trough inundation that is impossible to capture in a categorical land cover map (Figure 5.4).

Unsurprisingly, our statistical analysis revealed that polygons within thaw lake basins are not representative of the broader, heterogeneous landscape and are significantly different in terms of microtopographic relief, area, and percent coverage by surface water (Kolmogorov-Smirnov test, $p < 0.001$ in all cases) (Figure 5.5). On average, polygons within drained thaw lake basins are lower-centered, larger, and less inundated than elsewhere. These trends may stem from several possible causes. The relative abundance of LCPs, for example, may reflect soil moisture in the active layer, which tends to be higher in lake basins than on the primary surface (Jorgenson and Shur, 2007), and may suppress seasonal thaw depths by increasing volumetric heat capacity, thereby limiting ice wedge thaw (French, 1996; Chapter 4). The reduced presence of thermokarst ponds within basins may also reflect limited ice wedge degradation; nonetheless, even in instances of sustained ice wedge thaw, the maximum area of trough ponds in basins is probably limited, as the ice wedges tend to be younger (having begun growing post-lake drainage) and therefore smaller than on the primary surface, curbing the potential for ground subsidence (Jorgenson and Shur, 2007). The relatively large area of polygons in drained thaw lake basins also is possibly associated with comparatively young ice wedge networks. Here, older polygons tend to become subdivided by the development of secondary and tertiary ice wedges, which develop after the evolution of microtopography changes the location of thermal contraction ground cracking, altering winter ground temperatures and the subsurface stress field

(Burn and O'Neill, 2015; Abolt et al., 2018).

Outside of drained thaw lake basins, a set of Kruskal-Wallis tests paired with post-hoc analysis revealed significant variation among all landscape units in which polygons were mapped in terms of polygonal relief, area, and inundation ($p < 0.001$ in all cases) (Figure 5.5). On the floodplain of the Sagavanirktok River, for example, well-developed polygons were rare (occupying just 15% of the terrain) but tended to be larger, flatter, and less inundated than elsewhere. Each of these trends matches predictions from Lachenbruch's (1962; 1966) pioneering analysis of the thermal mechanics of ice wedge cracking. In that study, it was demonstrated that ice wedges should be smaller and more widely interspersed in coarse alluvial sediments than in fine grained soils, due to a lower coefficient of thermal contraction. Because ice wedges in coarse sediments are narrower in cross section, it follows that LCP rims should be less prominent, and troughs should be smaller, even above ice wedges affected by thermokarst. In sharp contrast to the floodplain, well-developed polygons are more common on the primary surface than anywhere else on the tundra, occupying 38% of the area; they are also smaller, higher-centered, and more inundated. The relatively high occurrence of thermokarst pools on the primary surface and the smaller area of the polygons likely reflects the age of the ice wedges, which almost certainly began developing prior to wedges in less stable sediments elsewhere on the tundra (Jorgenson and Shur, 2007; Morse and Burn, 2013). In comparison, these older wedges tend to be wider, increasing the size of the ponds that form during thermokarst, and more riddled with secondary and tertiary wedges, subdividing the oldest polygons into smaller units.

A second set of Kruskal-Wallis tests confirmed that differences among landscape units remain significant ($p < 0.001$ in all cases) within each nominal class of polygons (*i.e.*, within

LCPs, HCPs, and FCPs). The analysis revealed that, contrary to the prevailing trend among the population at large, LCPs tend to be larger on the primary surface than elsewhere on the tundra; otherwise, however, trends within nominal classes mirrored patterns detected throughout the survey area (Figure 5.6). Despite this variability among landscape units, the analysis also revealed that variability in area and inundation among polygon classes tends to follow consistent patterns. For example, on all landscape units, HCPs tend to be smaller than other polygons by area, and FCPs are the least inundated by thermokarst pools. This finding implies that, for the purpose of upscaling local observations of carbon fluxes, dividing polygonal terrain into nominal classes of LCP, FCP, and HCP is a sensible approach. Nonetheless, the high level of variability among each class (reflected in the large error bars in Figure 5.6) underscores the uncertainty inherent in bottom-up approaches to estimating landscape-scale carbon fluxes.

With regard to the relationship between ice wedge polygon class and thermokarst pools, our results indicate that nearly an equal portion of LCPs and HCPs (~40%) across the landscape are affected to some extent by surface water; however, when flooded, LCPs tend to experience a greater degree of inundation than HCPs (Figure 5.7). This nuance complements recent observations from elsewhere in the Arctic, that HCP formation often is associated with gradual thermokarst pool development, but surface water expansion may stop or even reverse at some critical threshold, at which the increasing interconnectivity of HCP troughs permits enhanced surface drainage (Liljedahl et al., 2016; Kanevskiy et al., 2017). Our findings seem to confirm that the transition of LCPs into HCPs does not necessarily increase the area of flooded troughs, which may function as hotspots for CO_2 and CH_4 emissions from the active layer

(Martin et al., 2018). Nonetheless, the current analysis cannot reveal whether ice wedge degradation itself increases in the fraction of the land surface occupied by thermokarst pools, as it is unclear whether the HCPs in our research area developed originally from LCPs, or from FCPs or completely flat terrain, in which thermokarst pools are less common.

Despite this ambiguity, one of the primary contributions from the present study is a baseline dataset from 2012-2014, against which results from future surveys may be compared. We anticipate that, should new high-resolution topographic data be acquired in the coming years in the same survey area, our delineation of polygon boundaries will permit direct quantification of contemporary microtopographic deformation in up to ~10^6 polygons, complementing observations of pond growth or decline. The data from such a survey will permit a robust analysis of what attributes render ice wedge polygons most susceptible to continued thermokarst, and whether troughs are becoming wetter or drier over time. By providing the starting point to quantify contemporary landscape evolution at high resolution, the present map will ultimately help to constrain projections of landscape-scale carbon fluxes derived from bottom-up and top-down approaches, reducing uncertainty in Arctic feedbacks to global climate change.

5.5 Summary

A novel machine-learning based algorithm was used to delineate and measure the microtopography of ice wedge polygons across ~1,000 km^2 of terrain through analysis of a high-resolution DEM. Approximately 10^6 polygons were detected, distributed unevenly through the landscape, representing 34% of the landcover. Lidar return intensity data were used to infer the percent coverage of each ice wedge polygon by thermokarst pools. Significant variation was observed in the morphology of polygons among landscape units; ice wedge polygons in drained thaw lake basins and in an alluvial floodplain tended to be lower-centered, larger, and less affected by the development of thermokarst pools than those found on the primary surface of the tundra. High-centered polygons were not affected to a greater degree by thermokarst pools than low-centered polygons, but the troughs of both endmembers were more inundated than flat-centered polygons. Our approach permits visualization of landscape heterogeneity in polygon morphology at an unprecedented spatial resolution; across the landscape, gradation between polygonal types occurs both gradually and abruptly. We anticipate that our map will function as a tool for constraining estimates of landscape-scale carbon fluxes from bottom-up and top-down approaches, and as a baseline for quantifying contemporary landscape deformation through future surveys.

Table 5.1

Results of manual validations of the polygon delineation, by landscape unit and across the survey area at large.

Landscape unit	Whole	Fragments	Conglomerates	False	Total
Primary surface	843	31	35	20	930
Thaw lake basins	51	2	3	1	56
Flood plain	11	3	0	0	14
Total	905	36	38	21	1000

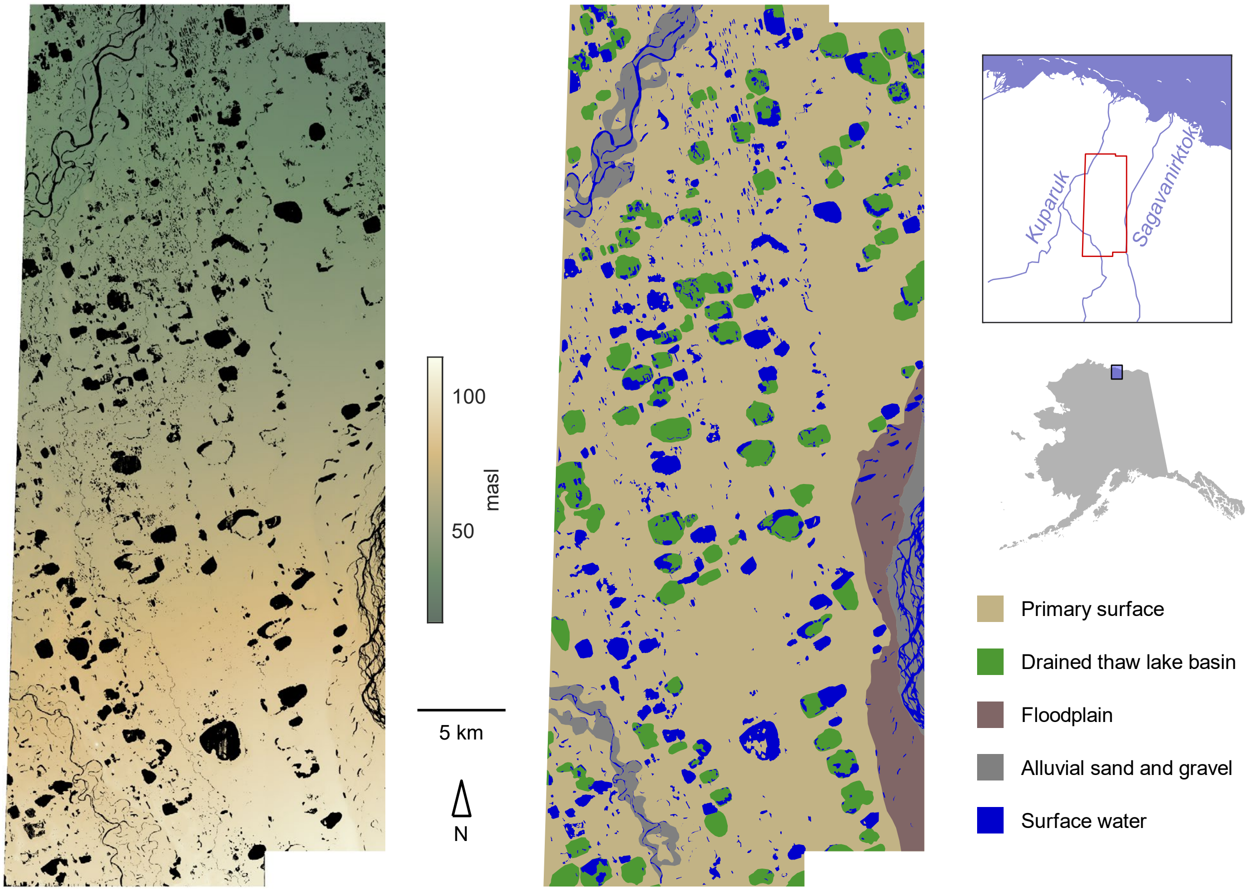

Figure 5.1

DEM of the survey area (left) and division of the site into landscape units (right), loosely following the approach of Jorgenson and Shur (2007). Location within Alaska shown in inset maps.

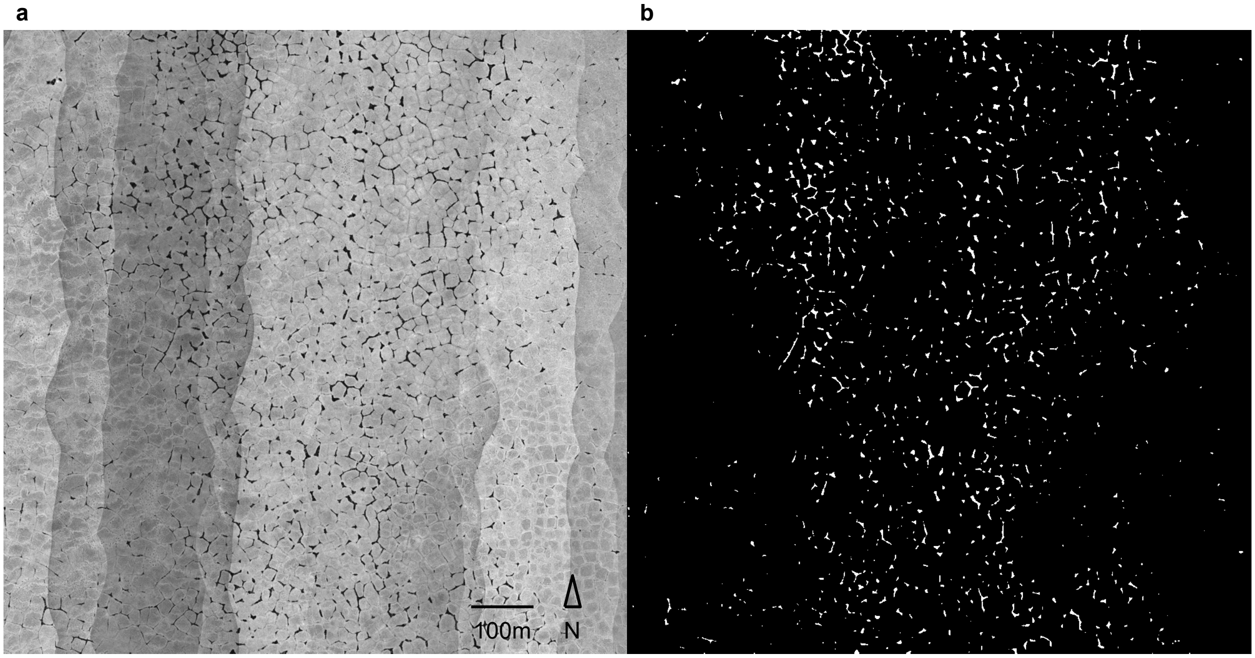

Figure 5.2

(a) 50 cm raster of lidar return intensity data from a 1 km^2 plot and **(b)** thermokarst pools inferred through application of the second CNN.

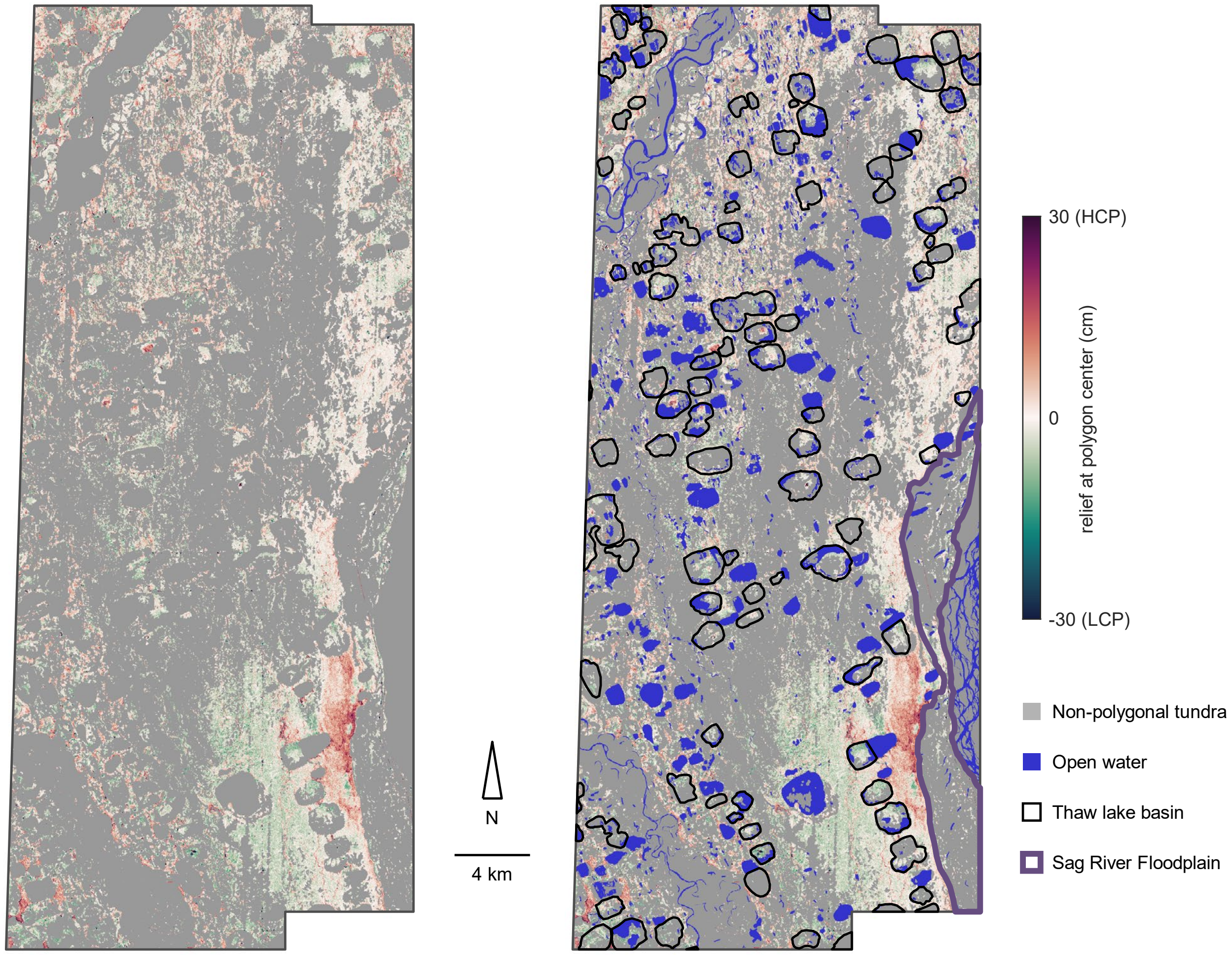

Figure 5.3

Microtopographic relief of ice wedge polygons mapped across the landscape (left) with open water, drained thaw lake basins, and the Sagavanirktok River floodplain outlined for reference (right).

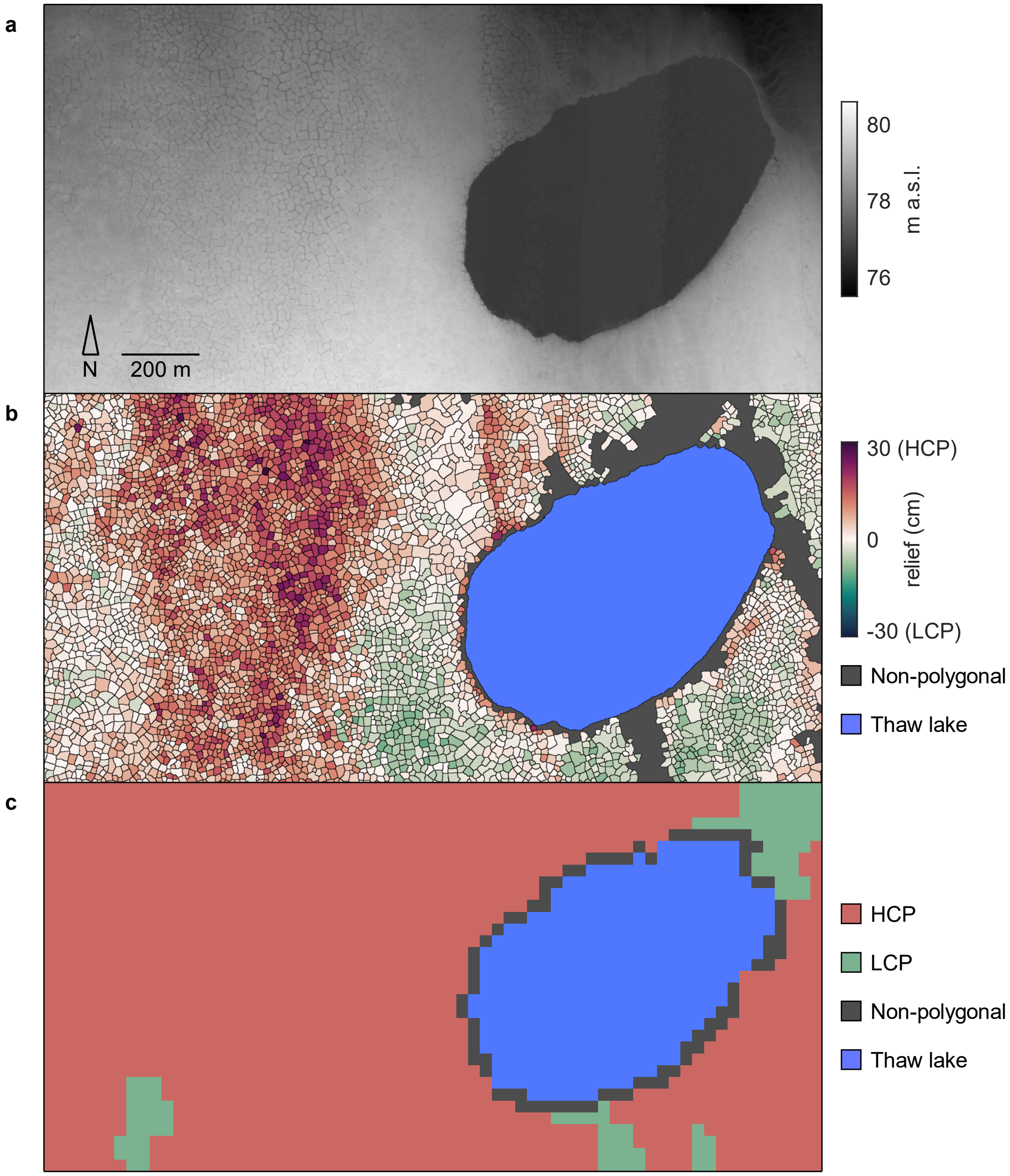

Figure 5.4

(a) 50 cm resolution DEM of a 2 km^2 region of the DEM, **(b)** inferred polygonal geomorphology from our approach, and **(c)** landcover map at 30 m resolution from Lara et al. (2018), used for comparison.

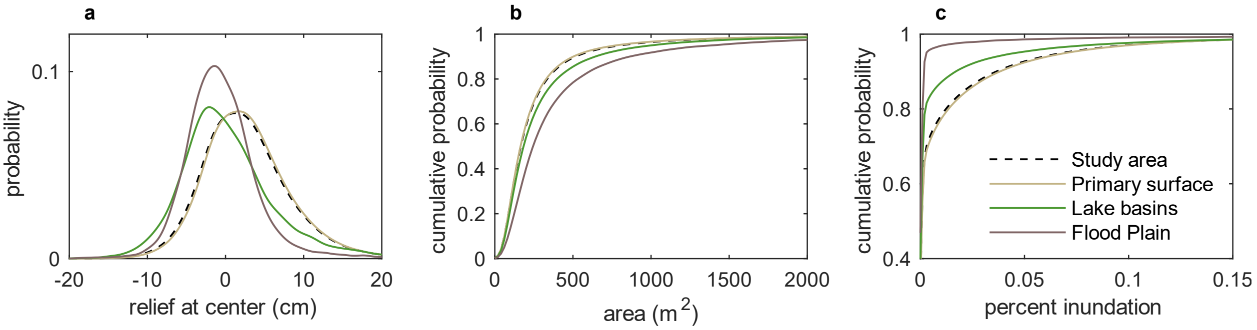

Figure 5.5

(a) Empirical distributions of microtopographic relief expressed as a probability distribution function, with **(b)** polygonal area**,** **(c)** and percent inundation by thermokarst pools expressed as cumulative distribution functions.

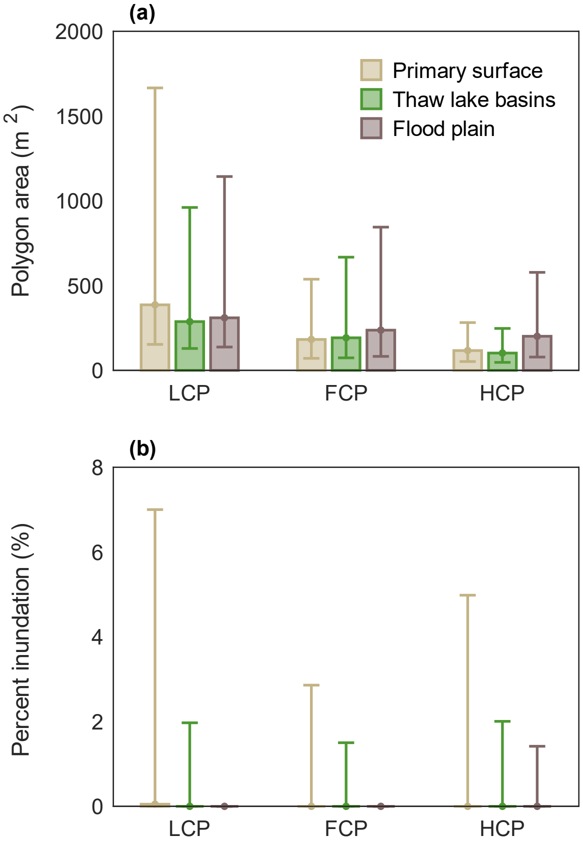

Figure 5.6

(a) Median area and **(b)** percent inundation by thermokarst pools, for nominal LCPs, FCPs, and HCPs by landscape unit, with 10th and 90th percentiles indicated by error bars. Note: Median percent cover by thermokarst pools is at or near zero among all polygon classes.

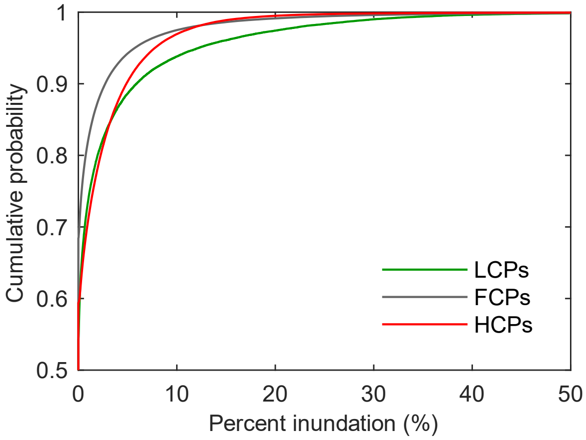

Figure 5.7

Empirical cumulative distribution functions of percent coverage by thermokarst pools for LCPs, FCPs, and HCPs across the survey area at large.

REFERENCES

Abolt CJ, Young MH, Atchley AL, Harp DR. 2018. Microtopographic control of the ground thermal regime in ice wedge polygons. *The Cryosphere* **12**: 1957-1968.

Abolt CJ, Young MH, Atchley AL, Wilson CJ. 2019. Rapid machine-learning-based extraction and measurement of ice wedge polygons in high-resolution digital elevation models. *The Cryosphere* **13**: 237-245.

Crisp D, OCO-2 Science Team. 2015. Measuring atmospheric carbon dioxide from space with the Orbiting Carbon Observatory-2 (OCO-2). In: Proceedings of SPIE Meeting 9607, Earth Observing Systems XX.

Gamon JA, Kershaw CP, Williamson S, Hik DS. 2012. Microtopographic patterns in an arctic baydjarakh field: Do fine-grain patterns enforce landscape stability? *Environmental Research Letters* **7**: 015502.

Garroway K, Hopkinson C, Jamieson R. 2011. Surface moisture and vegetation influences on lidar intensity data in an agricultural watershed. *Canadian Journal of Remote Sensing* **37**: 275-284.

Henderson JM, Eluszkiewicz J, Mountain ME, et al. 2015. Atmospheric transport simulations in support of the Carbon in Arctic Reservoirs Vulnerability Experiment (CARVE). *Atmospheric Chemistry and Physics* **15**: 4093-4116.

Jorgenson MT, Shur Y, Pullman ER. 2006. Abrupt increase in permafrost degradation in Arctic Alaska. *Geophysical Research Letters* **25**: L02503.

Jorgenson MT, Shur Y. 2007. Evolution of lakes and basins in northern Alaska and discussion of the thaw lake cycle. *Journal of Geophysical Research* **112**: F02S17.

Jorgenson MT, Kanevskiy M, Shur Y, et al. 2015. Role of ground ice dynamics and ecological feedbacks in recent ice wedge degradation and stabilization. *Journal of Geophysical Research: Earth Surface* **120**, 2280-2297.

Kanevskiy M, Shur Y, Jorgenson MT, et al. 2017. Degradation and stabilization of ice wedges: Implication for assessing risk of thermokarst in northern Alaska. *Geomorphology* **297**: 20-42.

Lachenbruch AH. 1962. Mechanics of thermal contraction cracks and ice-wedge polygons in permafrost. Geological Society of America Special Paper 70.

Lara MJ, McGuire DA, Euskirchen ES, et al. 2015. Polygonal tundra geomorphological change in response to warming alters future CO_2 and CH_4 flux on the Barrow Peninsula. *Global Change Biology* **21**: 1634-1651.

Lara MJ, Nitze I, Grosse G, McGuire AD. 2018. Tundra landform and vegetation trend maps for the Arctic Coastal Plain of northern Alaska. *Scientific Data* **5**: 180058.

Leffingwell EK. 1915. Ground-ice wedges, the dominant form of ground-ice on the north coast of

Alaska. *Journal of Geology* **23**: 635-654.

Liljedahl AK, Boike J, Daanen RP, et al. 2016. Pan-Arctic ice wedge degradation in warming permafrost and its influence on tundra hydrology. *Nature Geoscience* **9**, 312-318.

Martin AF, Lantz TC, Humphreys ER. 2018. Ice wedge degradation and CO_2 and CH_4 emissions in the Tuktoyaktuk Coastlands, Northwest Territories. *Arctic Science* **4**, 130-145.

Miller CE, Dinardo SJ. 2012. CARVE: The Carbon in Arctic Reservoirs Vulnerability Experiment. In: Proceedings of IEEE Aerospace Conference 2012.

Olivas PC, Oberbauer SF, Tweedie C, Oechel WC, Lin D, Kuchy A. 2011. Effects of fine-scale topography on CO_2 flux components of Alaskan coastal plain tundra: Response to contrasting growing seasons. *Arctic Antarctic and Alpine Research* **43**: 256-266.

Paine JG, Andrews JR, Saylam K, Tremblay TA. 2015. Airborne LiDAR-based wetland and permafrost-feature mapping on an Arctic Coastal Plain, North Slope, Alaska. In: *Remote Sensing of Wetlands*, Tiner RW, Klemas VV, Lang MW (eds). CRC Press: Boca Raton, FL.

Sturtevant CS, Oechel WC, Zona D, Kim Y, Emerson CE. 2012. Soil moisture control over autumn season methane flux, Arctic Coastal Plain of Alaska. *Biogeosciences* **9**: 1423-1440.

Sturtevant CS, Oechel WC. 2013. Spatial variation in landscape-level CO_2 and CH_4 fluxes from arctic coastal tundra: Influence from vegetation, wetness, and the thaw lake cycle. *Global Change Biology* **19**: 2853-2866.

Wainwright HM, Dafflon B, Smith LJ, et al. 2015. Identifying multiscale zonation and assessing the relative importance of polygon geomorphology on carbon fluxes in an Arctic tundra ecosystem. *Journal of Geophysical Research: Biogeosciences* **120**, 788-808.

Zona D, Lipson DA, Zulueta RC, Oberbauer SF, Oechel WC. 2011. Microtopographic controls on ecosystem functioning in the Arctic Coastal Plain. *Journal of Geophysical Research* **116**: G001241.

Chapter 6: Conclusion

The fundamental questions guiding this research were:

1. How does microtopographic deformation during thermokarst exert feedbacks on the ground thermal regime?
2. How stable is the land surface after thermokarst?
3. What will the land surface look like decades to centuries from now?

The preceding investigations into these questions yielded insights into the geomorphic changes that will occur in polygonal landscapes as air temperatures in the Arctic increase, and resulted in a new tool for quantifying microtopographic relief in high-resolution digital elevation models (DEMs). By helping to constrain projections of land surface evolution on the tundra, this research ultimately will reduce uncertainty in projections of hydrologic and ecological processes on the tundra as the climate continues to warm.

Chapter 2 focused on how variability in polygonal microtopography influences ground temperatures in winter, which in turn determine the likelihood of thermal contraction cracking. The investigation revealed that during cold months, low-centered polygon (LCP) rims function as preferential outlets of heat to the atmosphere—much like the ears of a jackrabbit—due to the relatively thin snowpack that develops atop them. This conclusion was reached through a combination of 1) hypothesis testing using ground temperature observations throughout the subsurface of an LCP, and 2) calibration-constrained numerical experiments examining how microtopography influences the ground thermal regime. The sensitivity analysis indicated that the loss of polygonal rims in high-centered polygons (HCPs), combined with increased snow accumulation in sunken HCP troughs, inhibits cooling in ice wedges, reducing the potential for thermal contraction fissures to open. This finding indicates that the restoration of LCP rims adjacent to thermokarst troughs over the next century is unlikely. Due to the insulation provided by the snow in HCP troughs, the climate would have to become either colder or less snowy than the conditions in which LCPs first developed in order for cracking to resume at its initial pace.

In Chapter 3, the sensitivity analysis was extended to explore positive and negative feedbacks on thermokarst, by examining how surface deformation influences the vulnerability of ice wedges to thaw. The experimental design employed simulations of the ground thermal regime to approximate the depth of trough-bottom soil necessary to buffer an ice wedge from thawing processes in late summer, a variable that was termed potential active layer thickness in the trough ($pALT_{tro}$). Differences in $pALT_{tro}$ between LCPs and HCPs were compared with rates of soil accumulation in thermokarst troughs observed by Jorgenson et al. (2006; 2015) and Kanevskiy et al. (2017), in order to infer the net impact of thermokarst on the stability of the permafrost. The analysis revealed that the intensity of positive feedbacks on ice wedge degradation is highly dependent on trough width. When trough width is confined to one meter, the difference in $pALT_{tro}$ beneath LCPs and HCPs is markedly less than the depths of new organic soil that typically accumulate within 10-15 years of the onset of thermokarst—indicating that the ice wedges surrounding many HCPs are relatively well-buffered against future climate extremes, in comparison with LCPs. When trough width approaches several meters, however, the boost to $pALT_{tro}$ associated with HCP development is nearly equal to the accumulation of new organic material; implying that in some cases thermokarst may continue for decades or longer. Nonetheless, when surface water is drained from the trough, differences in $\mathrm{pALT_{tro}}$ between LCPs and HCPs disappear. Because pools often shrink or disappear at advanced stages of thermokarst, it was concluded that in most cases, soil accumulation provides a robust negative feedback on ice wedge degradation. This finding implies that the stability of the land surface tends to increase after thermokarst.

Whereas the first two investigations in this dissertation employed numerical experiments to gain insights into thermokarst, the latter two were focused on remote sensing. In Chapter 4, a novel, machine-learning based algorithm was developed to delineate and measure the microtopography of ice wedge polygons in high-resolution digital elevation models. This new approach permits high-resolution inventories of ice wedge polygon geomorphology at the landscape scale, and quantifies microtopographic relief along a continuous spectrum, in contrast to previous approaches which divide polygons into nominal classes such as LCP or HCP. In Chapter 5, the algorithm was applied across a ~1,000 km^2 landscape near Prudhoe Bay, Alaska, delineating ~10^6 ice wedge polygons. The analysis revealed significant variation in ice wedge polygon geomorphology between drained thaw lake basins—where the majority of recent investigations into gas fluxes have been conducted—and the tundra at large. Across the landscape, the spatial distribution of ice wedge polygon geomorphology was highly heterogenous, and the transitions between clusters of LCPs and HCPs were at times gradational and at others very sharp—underscoring the non-uniform extent to which thermokarst has affected the terrain, and the challenges of upscaling local observations of gas exchange to regional estimates of carbon fluxes.

Looking forward, the next steps in this research should be focused on 1) validating the findings from the numerical modeling experiments and 2) incorporating geospatial analyses of polygon geomorphology into estimates of present and future carbon fluxes on the tundra. One particularly exciting approach toward addressing both these objectives would involve returning to the field south of Prudhoe Bay to conduct new surveys. The most recent airborne lidar data from the site was now acquired almost five years ago. New topographic data would permit a quantitative analysis of contemporary thermokarst processes among an enormous sample of polygons, representing a diverse set of initial conditions. These data could be acquired either through a new airborne lidar mission, or more cheaply through photogrammetric analysis of visual imagery captured from an unmanned aerial vehicle. Quantification of polygon-level surface deformation across the landscape would test the conclusion from this dissertation that HCPs—particularly those with narrow troughs—are more stable than polygons unaffected by thermokarst. Identification of areas that have experienced ground subsidence since 2014 would also help to determine whether thermokarst increases the overall fraction of the land surface occupied by pools of open water. The rates of landscape evolution inferred from such an analysis would inform predictions of thermokarst-driven changes to landscape-scale carbon cycling over the next several decades, which ultimately can be validated using data products from airborne and spaceborne sensors, such as the OCO-2 satellite.

Outside of this possibility, the research begun in this dissertation offers other opportunities to advance understanding of hydrologic and ecological processes in polygonal tundra. One particularly relevant line of research (which has intensified in the last several years) is the development of a simplified parameterization of ice wedge polygon microtopography and thermokarst processes to incorporate into global Earth system models, which are used to project interactions between climate change and carbon cycling (*e.g.*, Nitzborn et al., 2018; Aas et al., 2019). The conclusions from polygon-level numerical simulations in Chapter 3, that trough width strongly controls the stability of ice wedges, but that ice wedges beneath HCPs tend to be more resilient to climate extremes than those beneath LCPs, may ultimately help to inform such a parameterization. Additionally, the polygon delineation tool introduced in Chapter 4 can accelerate the pace at which spatial heterogeneity in polygon geomorphology is quantified—and field sites for ecological studies can be selected—at field sites around the Arctic. The code for this tool is available for download from a public repository (Abolt et al., 2019). As the availability of high-resolution elevation data increases, high-resolution mapping of polygonal geomorphology will ultimately help to bridge the gap in spatial resolution between local and regional observations of hydrologic and ecological processes.

REFERENCES

Aas KS, Martin L, et al. 2019. Thaw processes in ice-rich permafrost landscapes represented with laterally coupled tiles in a land surface model. *The Cryosphere* **13**: 597-609.

Abolt CJ, Young MH, Atchley AL, Wilson CJ. 2019. CNN-watershed: A machine learning-based tool for delineation and measurement of ice wedge polygons in high-resolution digital elevation models. Zenodo repository. doi:10.5281/zenodo.2554542.

Jorgenson MT, Shur Y, Pullman ER. 2006. Abrupt increase in permafrost degradation in Arctic Alaska. *Geophysical Research Letters* **25**: L02503.

Jorgenson MT, Kanevskiy M, Shur Y, et al. 2015. Role of ground ice dynamics and ecological feedbacks in recent ice wedge degradation and stabilization. *Journal of Geophysical Research: Earth Surface* **120**, 2280-2297.

Nitzborn J, Langer M, et al. 2019. Pathways of ice-wedge degradation in polygonal tundra under difference hydrological conditions. *The Cryosphere* **13**: 1089-1123.

Appendix: Surface and subsurface physics in Amanzi-ATS

The primary mode of subsurface water transport in Amanzi-ATS is conduction in the liquid phase against pressure (or suction) gradients. Heat is both advected with liquid water and conducted against temperature gradients. Equations for the conservation of mass and energy in the subsurface are coupled with corresponding equations for the mass and energy balance at the surface, which are forced using exogenous meteorological data (Figure A.1). The following summary of surface and subsurface physics represented in Amanzi-ATS summarizes more extensive documentation provided by Atchley et al. (2015) and Painter et al. (2016).

Conservation of water mass in the subsurface is solved using a modified form of the Richards equation:

$$\frac{\partial}{\partial t}\left[\phi\left(\omega_g \eta_g s_g + \eta_l s_l + \eta_i s_i\right)\right] = -\nabla \cdot [\eta_l \boldsymbol{V}_l] + Q_w \tag{A1}$$

where, on the left-hand side, ϕ represents porosity; the subscripts *g*, *l*, and *i* refer to the gas, liquid, and ice phases within the pore space; ω is the mole fraction of water in a particular phase (mol mol^{-1}); η is the molar density of a particular phase (mol m^{-3}); and *s* is saturation. The sole term on the left side of the equation thus accounts for the time rate of change of water mass stored in three phases at a point in the subsurface. On the right-hand side, $\boldsymbol{V}_l$ is the three-dimensional Darcy flux in the liquid phase (m s^{-1}), and Q_w captures sources and sinks of water (mol s^{-1}). The first term thus represents the negative divergence of the liquid water flux at a point, while the second term accounts for processes (such as infiltration or evaporation) which influence cells at the top of the soil column.

The flux of liquid water, $\boldsymbol{V}_l$, in Equation A1 is defined using the Buckingham-Darcy law:

$$\boldsymbol{V}_l = -\frac{k_{rl}k}{\mu_l}(\nabla p_l + \rho_l g\hat{z}) \tag{A2}$$

where k is intrinsic permeability (m^2), k_r is relative permeability (a function of liquid- and ice-saturation), μ is dynamic viscosity (Pa s), p is pressure (Pa), ρ is mass density (kg m^{-3}), g is gravitational acceleration (m s^{-2}), and $\hat{z}$ is a unit vector in the vertical direction, or against the force of gravity. Liquid water conduction is therefore the product of a dynamic estimate of hydraulic conductivity and the combined pressure and elevation head gradients in the liquid phase. In unfrozen conditions, relative permeability and liquid pressure are treated as functions of liquid saturation, using the van Genuchten-Mualem parameterization. In sub-freezing conditions, partitioning of the liquid, solid, and gas phases, and estimation of relative permeability and pressure, are accomplished through a novel extension to this parameterization presented in Karra et al. (2014).

Conservation of energy in the subsurface is represented in the equation:

$$\frac{\partial}{\partial t}\left[\phi \sum_{p=l,g,i}\left(\eta_p s_p u_p\right) + (1-\phi)C_{v,soil}T\right] = -\nabla \cdot (\eta_l h_l \boldsymbol{V}_l) + \nabla \cdot (\kappa_e \nabla T) + Q_E \tag{A3}$$

where u is the specific internal energy for mass in a particular phase (J mol^{-1}), $C_{v,soil}$ is the volumetric heat capacity for solid materials in the soil (J m^{-3} K^{-1}), T is temperature (K), h is specific enthalpy (J mol^{-1}), κ_e is the thermal conductivity of the soil (again, a function of liquid- and ice-saturation), and Q_E accounts for sources and sinks of energy. The term on the left thus represents the time change in energy stored both in the pore space and the soil matrix, while the three terms on the right represent the processes of advection, heat conduction, and external introduction or removal of heat, respectively. Amanzi-ATS includes options to represent the dependence of soil thermal conductivity on liquid- and ice-saturation through a number of parameterizations discussed in Atchley et al. (2015).

The surface energy balance is calculated either at the surface of a snow pack or pond (if present), or at ground surface if the tundra is bare. The calculation can be summarized as:

$$0 = (1 - \alpha)Q_{sw}^{in} + Q_{lw}^{in} + Q_{lw}^{out} + Q_h(T_s) + Q_e(T_s) + Q_c(T_s) \tag{A4}$$

where α is surface albedo; Q_{sw}^{in} is incoming shortwave radiation; Q_{lw}^{in} and Q_{lw}^{out} are incoming and outgoing longwave radiation, respectively; Q_h is the sensible heat flux; Q_e is the latent heat flux; Q_c is the conductive heat flux, calculated either through the snow pack or ponded water if present, or through the uppermost soil cell if the surface is bare; and T_s is surface temperature (K). All terms in Equation A4 have units of W m^{-2}. Incoming shortwave and longwave radiation are specified in the meteorological forcing data, while outgoing longwave radiation is the product of the Stefan-Boltzmann constant, emissivity (which varies depending on whether the surface is water, ice, snow, or bare tundra), and surface temperature raised to the fourth power. The albedos of ice, water, and bare tundra used by Amanzi-ATS are constants derived from the literature, but the albedo of snow varies in time, as estimated through an empirical model that tends to result in increased albedo as the season progresses. As the snowpack ages, snow thermal conductivity and density also increase according to empirical models; time-variable estimates of snow density are incorporated into calculations of snow depth, to conserve mass.

Among the remaining fluxes in the surface energy balance, the sensible heat flux is calculated as the product of: 1) the difference between surface and air temperature, and 2) a turbulent conductance coefficient, which is a function of wind speed and surface roughness (which itself varies among snow, water, ice, and bare tundra). The latent heat flux is estimated as the product of: 1) the difference between saturated vapor pressure at the surface and vapor pressure in the air column, 2) another turbulent conductance coefficient, and 3) the latent heat of sublimation (in the case of snow) or evaporation (in the case of ponded water or bare tundra). When snow or water are present, the turbulent conductance coefficient for the latent heat flux becomes a function of windspeed and surface roughness; when the ground is bare, this coefficient is modified to incorporate soil resistance to evaporation, which is a function of liquid saturation and the unsaturated hydraulic parameters at the top of the soil column.

Snow and liquid water are allowed to accumulate at the surface in response to precipitation; snow mass can be lost through sublimation (estimated through calculations of the latent heat flux) or melting (as snowpack temperature approaches 0°C), while ponded water mass can be lost through evaporation or infiltration into the subsurface. Strong coupling between the surface and subsurface is incorporated by ensuring continuity across the surface in liquid pressure and hydrologic flux (for the mass balance) and temperature and heat flux (for the energy balance). Thus, the surface mass and energy balances are used to define Neumann-type boundary conditions for the subsurface equations, and four inter-dependent matrices (representing mass and energy balance at the surface and in the subsurface) are solved iteratively and simultaneously. In two- and three- dimensional simulations, both snow and liquid water can flow across surface topography via a Mannings-type equation, which produces a flat surface over time.

As snow or liquid water accumulate at the top of the spatial domain, depth and state variables (such as temperature) are calculated within a single layer of surface cells. Vertical stratification in snow and water temperature is thus ignored. The top-down freezing of surface water is accounted for by calculating a frozen fraction at each time step; the frozen fraction increases as a sigmoidal function from 0 to 1 as water temperature decreases from 0°C to some fraction of a degree lower, specified by the user. This formulation allows for conservation of energy during freeze and thaw. Once the frozen fraction is greater than zero, snow is allowed to accumulate atop a pond, as the water beneath continues to freeze.

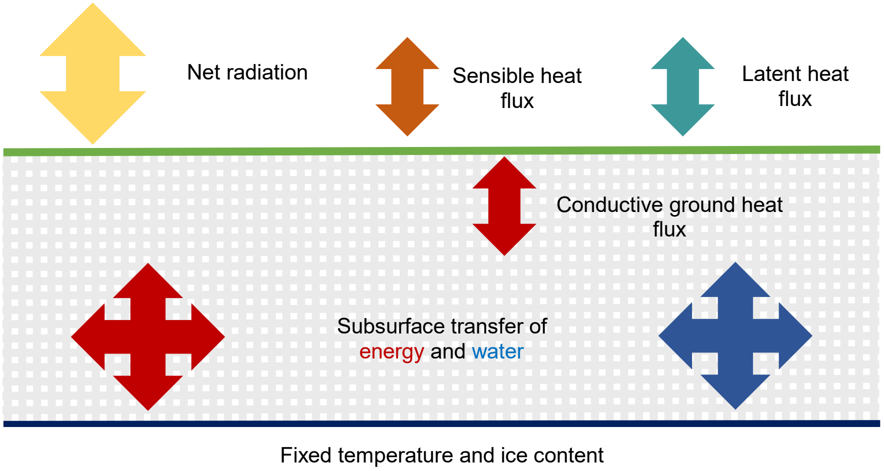

Figure A.1

Conceptual diagram of surface and subsurface physics in Amanzi-ATS simulations.

REFERENCES

Atchley AL, Painter SL, et al. 2015. Using field observations to inform thermal hydrology models of permafrost dynamics with ATS (v0.83). *Geoscientific Model Development* **8**: 2701–2722.

Karra S, Painter SL, Lichtner PC. (2014). Three-phase numerical model for subsurface hydrology in permafrost-affected regions (PFLOTRAN-ICE v1.0). *The Cryosphere* **8**: 1935-1950.

Painter SL, Coon ET. 2016. Integrated surface/subsurface permafrost thermal hydrology: Model formulation and proof-of-concept simulations. *Water Resources Research* **52**: 6062-6077.

Bibliography

Aas KS, Martin L, et al. 2019. Thaw processes in ice-rich permafrost landscapes represented with laterally coupled tiles in a land surface model. *The Cryosphere* **13**: 597-609.

Abolt CJ, Young MH, Caldwell TG. 2017. Numerical modelling of ice-wedge polygon geomorphic transition. *Permafrost and Periglacial Processes* **28**: 347-355.

Abolt CJ, Young MH, Atchley AL, Harp DR. 2018. Microtopographic control on the ground thermal regime in ice wedge polygons. *The Cryosphere* **12**: 1957-1968.

Allard M, Kasper JN. 1998. Temperature conditions for ice-wedge cracking: Field measurements from Salluit, northern Quebec. In: Proceedings of the Seventh International Conference on Permafrost, pp. 5–12, National Research Council of Canada.

Atchley AL, Painter SL, et al. 2015. Using field observations to inform thermal hydrology models of permafrost dynamics with ATS (v0.83). *Geoscientific Model Development* **8**: 2701–2722.

Atchley AL, Coon ET, et al. 2016. Influences and interactions of inundation, peat, and snow on active layer thickness. *Geophysical Research Letters* 43: GL068550.

Burn CR. 2004. A field perspective on modelling 'single-ridge' ice-wedge polygons. *Permafrost and Periglacial Processes* **15**: 59–65.

Burn CR, O'Neill HB. 2015. Subdivision of ice-wedge polygons, western Arctic coast. Canadian Geotechnical Society. Quebec, QC.

Cabot EC. 1947. The northern Alaskan coastal plain interpreted from aerial photographs. *Geographical Review* **37**: 639-648.

Carson CE. 1968. Radiocarbon dating of lacustrine strands in Arctic Alaska. *Arctic* **21**: 12-26.

Christiansen HH. 2005. Thermal regime of ice-wedge cracking in Adventdalen, Svalbard. *Permafrost and Periglacial Processes* **16:** 87-98.

Ciresan D, Giusti A, Gambardella LM, Schmidhuber J. 2012. Deep neural networks segment neuronal membranes in electron microscopy images. In: Pereira F, Burges CJC, Bottou L, Weinberger Q (eds). Advances in Neural Information Processing Systems 25, pp. 2843-2851, Curran Associates, Inc.

Coon ET, Moulton D, Painter SL. 2016. Managing complexity in simulations of land surface and near-surface processes. *Environmental Modelling & Software* **78**: 134–149.

Crisp D, OCO-2 Science Team. 2015. Measuring atmospheric carbon dioxide from space with the Orbiting Carbon Observatory-2 (OCO-2). In: Proceedings of SPIE Meeting 9607, Earth Observing Systems XX.

Domine F, Barrere M, Sarrazin D. 2016. Seasonal evolution of the effective thermal conductivity of the snow and the soil in high Arctic herb tundra at Bylot Island, Canada. *The Cryosphere* **10**: 2573–2588.

Dostovalov BN, Popov AI. 1966. Polygonal systems of ice-wedges and conditions of their development. In: Proceedings of the International Conference on Permafrost, pp. 71–76, National Academy of Sciences-National Research Council.

Everett KR. 1980. Landforms. In: DA Walker, KR Everett, PJ Webber, J Brown (Eds.). *Geobotanical Atlas of the Prudhoe Bay Region, Alaska*, pp. 14-19. Hanover, NH: US Army Cold Regions Research and Engineering Laboratory.

Fortier D, Allard M. 2005. Frost-cracking conditions, Bylot Island, eastern Canadian Arctic archipelago. *Permafrost and Periglacial Processes* **16**: 145–161.

Fortier D, Allard M, Shur Y. 2007. Observation of rapid drainage system development by thermal erosion of ice wedges on Bylot Island, Canadian Arctic Archipelago. *Permafrost and Periglacial Processes* **18**: 229-243.

Gamon JA, Kershaw GP, et al. 2012. Microtopographic patterns in an arctic baydjarakh field: do fine-grain patterns enforce landscape stability? *Environmental Research Letters* **7**: 015502.

Garroway K, Hopkinson C, Jamieson R. 2011. Surface moisture and vegetation influences on lidar intensity data in an agricultural watershed. *Canadian Journal of Remote Sensing* **37**: 275-284.

Goodrich LE. 1982. The influence of snow cover on the ground thermal regime. *Canadian geotechnical journal* **19**: 421–432.

Grosse G, Harden J., et al. 2011. Vulnerability of high-latitude soil organic carbon in North America to disturbance. *Journal of Geophysical Research: Biogeosciences* ***116***: G00K06.

Harp DR, Atchley AL, et al. 2016. Effect of soil property uncertainties on permafrost thaw projections: a calibration-constrained analysis. *The Cryosphere* **10**: 341–358.

He K, Gkioxari G, Dollar P, Girshick R. 2017. Mask R-CNN. In: Proceedings of the 2017 IEEE International Conference on Computer Vision, IEEE.

Henderson JM, Eluszkiewicz J, Mountain ME, et al. 2015. Atmospheric transport simulations in support of the Carbon in Arctic Reservoirs Vulnerability Experiment (CARVE). *Atmospheric Chemistry and Physics* **15**: 4093-4116.

Hugelius G, Strauss J, et al. 2014. Estimated stocks of circumpolar permafrost carbon with quantified uncertainty ranges and identified data gaps. *Biogeosciences* **11**: 6573-6593.

Isarin RFB. 1997. Permafrost distribution and temperatures in Europe during the Younger Dryas. *Permafrost and Periglacial Processes* **8**: 313–333.

Jan A, Coon ET, et al. 2018. An intermediate-scale model for thermal hydrology in low-relief permafrost-affected landscapes. *Computational Geosciences* **22**: 163-177.

Johnson WH. 1990. Ice-wedge casts and relict patterned ground in central Illinois and their environmental significance. *Quaternary Research* **33**: 51–72.

Jorgenson MT, Shur Y, Pullman ER. 2006. Abrupt increase in permafrost degradation in Arctic

Alaska. *Geophysical Research Letters* **25**: L02503.

Jorgenson MT, Shur Y. 2007. Evolution of lakes and basins in northern Alaska and discussion of the thaw lake cycle. *Journal of Geophysical Research* **112**: JF000531.

Jorgenson MT, Romanovsky V., et al. 2010. Resilience and vulnerability of permafrost to climate change. *Canadian Journal of Forest Research* **40**: 1219-1236.

Jorgenson MT, Kanevskiy M, Shur Y, et al. 2015. Role of ground ice dynamics and ecological feedbacks in recent ice wedge degradation and stabilization. *Journal of Geophysical Research: Earth Surface* **120**, 2280-2297.

Kanevskiy M, Shur Y, et al. 2013. Ground ice in the upper permafrost of the Beaufort Sea coast of Alaska. *Cold Regions Science and Technology* **85**: 56-70.

Kanevskiy M, Shur Y, Jorgenson MT, et al. 2017. Degradation and stabilization of ice wedges: Implication for assessing risk of thermokarst in northern Alaska. *Geomorphology* **297**: 20-42.

Karra S, Painter SL, Lichtner PC. (2014). Three-phase numerical model for subsurface hydrology in permafrost-affected regions (PFLOTRAN-ICE v1.0). *The Cryosphere* **8**: 1935-1950.

Kestur R, Farooq S, Abdal R, Mehraj E, Narasipura O, Mudigere M. 2018. UFCN: A fully convolutional neural network for road extraction in RGB imagery acquired by remote sensing from an unmanned aerial vehicle. *Journal of Applied Remote Sensing* **12**: 016020.

Koch JC, Jorgenson MT, et al. (2018). Ice wedge degradation and stabilization impact water budgets and nutrient cycling in Arctic trough ponds. *Journal of Geophysical Research: Biogeosciences* **123**: 2604-2616.

Kokelj SV, Pisaric MFJ, Burn CR. 2007. Cessation of ice wedge development during the 20th century in spruce forests of eastern Mackenzie Delta, Northwest Territories, Canada. *Canadian Journal of Earth Sciences* **44**: 1503–1515.

Kokelj SV, Lantz TC, et al. 2014. Distribution and activity of ice wedges across the forest-tundra transition, western Arctic Canada. *Journal of Geophysical Research: Earth Surface* **119**: 2032-2047.

Lachenbruch AH. 1962. Mechanics of thermal contraction cracks and ice-wedge polygons in permafrost. Geological Society of America Special Paper 70.

Lachenbruch AH. 1966. Contraction theory of ice-wedge polygons: A qualitative discussion. In: Proceedings of the International Conference on Permafrost, pp. 63–70, National Academy of Sciences-National Research Council.

Langer M, Westermann S, et al. 2011a. The surface energy balance of a polygonal tundra site in northern Siberia—Part 1: Spring to fall. *The Cryosphere* **5**: 151-171.

Langer M, Westermann S, et al. 2011b. The surface energy balance of a polygonal tundra site in northern Siberia—Part 2: Winter. *The Cryosphere* **5**: 509-524.

Langer M, Westermann S, et al. 2016. Rapid degradation of permafrost underneath waterbodies in tundra landscapes—Toward a representation of thermokarst in land surface models. *Journal of Geophysical Research: Earth Surface* **121**: 2446-2470.

Lara MJ, McGuire DA, Euskirchen ES, et al. 2015. Polygonal tundra geomorphological change in response to warming alters future CO_2 and CH_4 flux on the Barrow Peninsula. *Global Change Biology* **21**: 1634-1651.

Lara MJ, Nitze I, Grosse G, McGuire AD. 2018. Tundra landform and vegetation trend maps for the Arctic Coastal Plain of northern Alaska. *Scientific Data* **5**: 180058.

Leffingwell EK. 1915. Ground-ice wedges, the dominant form of ground-ice on the north coast of Alaska. *Journal of Geology* **23**: 635-654.

Levy JS, Marchant DR, Head JW. 2010. Thermal contraction crack polygons on Mars: A synthesis from HiRISE, Phoenix, and terrestrial analogue studies. *Icarus* **226**: 229-252.

Liljedahl AK, Hinzman LD, Schulla J. 2012. Ice-wedge polygon type controls low-gradient watershed-scale hydrology. *Tenth International Congerence on Permafrost*: Salekhard, Russia. June 25-29.

Liljedahl AK, Boike J, Daanen RP, et al. 2016. Pan-Arctic ice wedge degradation in warming permafrost and its influence on tundra hydrology. *Nature Geoscience* **9**, 312-318.

Lipson DA, Zona D. 2012. Water-table height and microtopography control biogeochemical cycling in an Arctic coastal tundra ecosystem. *Biogeosciences* **9**: 577-591.

Lousada M, Pina M, Vieira G, Bandeira L, Mora C. 2018. Evaluation of the use of very high resolution aerial imagery for accurate ice-wedge polygon mapping (Adventdalen, Svalbard). *Science of the Total Environment* **615**: 1574-1583.

Mackay JR. 1984. The direction of ice-wedge cracking in permafrost: Downward or upward? *Canadian Journal of Earth Sciences* **21**: 516-524.

Mackay JR. 1990. Some observations on the growth and deformation of epigenetic, syngenetic, and anti-syngenetic ice wedges. *Permafrost and Periglacial Processes* **1**: 15-29.

Mackay JR. 1993. Air temperature, snow cover, creep of frozen ground, and the time of ice-wedge cracking, western Arctic coast. *Canadian Journal of Earth Sciences* **30**: 1720–1729.

Mackay JR. 1995. Ice wedges on hillslopes and landform evolution in the late Quaternary, western Arctic coast, Canada. *Canadian Journal of Earth Science* **32**: 1093-1105.

Mackay JR. 2000. Thermally induced movements in ice-wedge polygons, western Arctic coast: A long-term study. *Géographie Physique et Quarternaire* **54**: 41-68.

Mackay JR, MacKay DK. 1974. Snow cover and ground temperatures, Garry Island, NWT. *Arctic*: 287–296, 1974.

Martin AF, Lantz TC, Humphreys ER. 2018. Ice wedge degradation and CO_2 and CH_4 emissions in the Tuktoyaktuk Coastlands, Northwest Territories. *Arctic Science* **4**, 130-145.

Menne MJ, Durre I., et al. 2012. An overview of the Global Historical Climatology Network-Daily database. *Journal of Atmospheric and Oceanic Technology* **29**: 897-910.

Miller CE, Dinardo SJ. 2012. CARVE: The Carbon in Arctic Reservoirs Vulnerability Experiment. In: Proceedings of IEEE Aerospace Conference 2012.

Morse PD, Burn CR. 2013. Field observations of syngenetic ice wedge polygons, outer Mackenzie Delta, western Arctic coast, Canada. *Journal of Geophysical Research: Earth Surface* **118**: 1320-1332.

Morse PD, Burn CR. 2014. Perennial frost blisters of the outer Mackenzie Delta, western Arctic coast, Canada. *Earth Surface Processes and Landforms* **39**: 200-213.

Moulton D, Buksas M, et al. 2011. High-level design of Amanzi, the multi-process high performance computing simulator. United States Department of Energy.

Murton JB. 2009. Global warming and thermokarst. In: R Margesin (Ed.), *Permafrost Soils,* pp. 185-203. Berlin: Springer.

Nitzborn J, Langer M, et al. 2019. Pathways of ice-wedge degradation in polygonal tundra under difference hydrological conditions. *The Cryosphere* **13**: 1089-1123.

Olivas PC, Oberbauer SF, Tweedie C, Oechel WC, Lin D, Kuchy A. 2011. Effects of fine-scale topography on CO_2 flux components of Alaskan coastal plain tundra: Response to contrasting growing seasons. *Arctic Antarctic and Alpine Research* **43**: 256-266.

O'Neill HB, Christiansen HH. 2018. Detection of ice wedge cracking in permafrost using miniature accelerometers. *Journal of Geophysical Research: Earth Surface* **123**: JF004343.

Osterkamp TE, Romanovsky VE. 1996. Characteristics of changing permafrost temperatures in the Alaskan Arctic, U.S.A. *Arctic and Alpine Research* **28**: 267.

Paine JG, Andrews JR, Saylam K, Tremblay TA. 2015. Airborne LiDAR-based wetland and permafrost-feature mapping on an Arctic Coastal Plain, North Slope, Alaska. In: *Remote Sensing of Wetlands*, Tiner RW, Klemas VV, Lang MW (eds). CRC Press: Boca Raton, FL.

Painter SL, Coon ET. 2016. Integrated surface/subsurface permafrost thermal hydrology: Model formulation and proof-of-concept simulations. *Water Resources Research* **52**: 6062-6077.

Pina P, Saraiva J, Bandeira L, Barata T. 2006. Identification of Martian polygonal patterns using the dynamics of watershed contours. In: Campilho A, Kamel M (eds). Image Analysis on Recognition, pp. 691-699, Springer-Verlag, Berlin-Heidelberg.

Pina P, Saraiva J, Bandeira L, Antunes J. 2008. Polygonal terrains on Mars: A contribution to their geometric and topological characterization. *Planetary and Space Science* **56**: 1919-1924.

Plug L, Werner B. 2002. Nonlinear dynamics of ice-wedge networks and resulting sensitivity to severe cooling events. *Nature* **417**: 929–933.

Raynolds MK, Walker DA, et al. 2014. Cumulative geoecological effects of 62 years of infrastructure and climate change in ice-rich permafrost landscapes, Prudhoe Bay Oilfield, Canada. *Global Change Biology* **20**: 1211-1224.

Riche F, Schneebeli M. 2013. Thermal conductivity of snow measured by three independent methods and anisotropy considerations. *The Cryosphere* **7**: 217–227.

Rodell M, Houser PR, et al. 2004. The Global Land Data Assimilation System. *Bulletin of the American Meteorological Society* **85**: 381–394.

Romanovsky V, Kholodov A, et al. 2009. Network of Permafrost Observatories in North America: Temperature in deep boreholes. Arctic Data Center.

Root JD. 1975. Ice-wedge polygons, Tuktoyaktuk area, N.W.T. Geological Survey of Canada.

Schuh C, Frampton A, Christiansen HH. 2017. Soil moisture redistribution and its effect on inter-annual active layer temperature and thickness variations in a dry loess terrace in Adventdalen, Svalbard. *The Cryosphere* **11**: 635-651.

Schuur EAG, Bockheim J, et al. 2008. Vulnerability of permafrost carbon to climate change: Implications for the global carbon cycle. *BioScience* **58**: 701-714.

Schuur EAG, Vogel JG, et al. 2009. The effect of permafrost thaw on old carbon release and net carbon exchange from tundra. *Nature* **459**: 556-559.

Schuur EAG, McGuire AD, et al. 2015. Climate change and the permafrost carbon feedback. *Nature* **520**: 171-179.

Sjoberg Y, Coon ET, et al. 2016. Thermal effects of groundwater flow through subarctic fens: A case study based on field observations and numerical modeling. *Water Resources Research* **52**: 1591-1606.

Soille P. 2004. Morphological Image Analysis, Springer-Verlag: Berlin Heidelberg.

Sturtevant CS, Oechel WC, Zona D, Kim Y, Emerson CE. 2012. Soil moisture control over autumn season methane flux, Arctic Coastal Plain of Alaska. *Biogeosciences* **9**: 1423-1440.

Sturtevant CS, Oechel WC. 2013. Spatial variation in landscape-level CO_2 and CH_4 fluxes from arctic coastal tundra: Influence from vegetation, wetness, and the thaw lake cycle. *Global Change Biology* **19**: 2853-2866.

Tarnocai C, Canadell JG, et al. Soil organic carbon pools in the northern circumpolar permafrost region. *Global Biogeochemical Cycles* **23**: GB2023.

Ulrich M, Hauber E, Herrzschuh U, Hartel S, Schirrmeister L. 2011. Polygon pattern geomorphometry on Svalbard (Norway) and western Utopia Planitia (Mars) using high resolution stereo remote-sensing data. *Geomorphology* **134**: 197-216.

Wainwright HM, Dafflon B, Smith LJ, et al. 2015. Identifying multiscale zonation and assessing the relative importance of polygon geomorphology on carbon fluxes in an Arctic tundra ecosystem. *Journal of Geophysical Research: Biogeosciences* **120**, 788-808.

Wainwright HM, Liljedahl AK, et al. 2017. Mapping snow depth within a tundra ecosystem using multiscale observations and Bayesian methods. *The Cryosphere* **11**: 857–875.

Wales NA, Gomez-Velez JD, Newman BD, et al. 2019. Understanding the relative importance of vertical and horizontal flow in ice-wedge polygons. *Hydrology and Earth System Sciences Discussions*. doi:10.5194/hess-2019-25.

Walker DA, Webber PJ, et al. 1987. Cumulative impacts of oil fields on northern Alaskan landscapes. *Science* **238**: 757–761.

Walters JC. 1994. Ice-wedge casts and relict patterned-ground in northeast Iowa, USA. *Permafrost and Periglacial Processes* **5**: 269–281.

Watanabe T, Matsuoka N, et al. 2017. Soil physical and environmental conditions controlling patterned ground variability at a continuous permafrost site, Svalbard. *Permafrost and Periglacial Processes* **28**: 433-445.

Wilson C, Gangodagamage C, Rowland J. 2013. Digital elevation model, 0.5 m, Utqiaġvik Environmental Observatory, Alaska, 2012. Next Generation Ecosystem Experiments Arctic Data Collection, Oak Ridge National Laboratory, US Department of Energy, doi:10.5440/1109234.

Wind GP. 1969. Capillary conductivity data estimated by a simple method. In: Water in the unsaturated zone: Proceedings of the Wageningen Symposium, vol. 1, pp. 181–191, International Association of Scientific Hydrology.

Xu YY, Xie Z, Feng YX, Chen ZL. 2018. Road extraction from high-resolution remote sensing imagery using deep learning. *Remote Sensing* **10**: 1461.

Yang D, Goodison BE, et al. 1998. Adjustment of daily precipitation data at 10 climate stations in Alaska: Application of World Meteorological Organization intercomparison results. Water Resources Research **34**: 241–256.

Zhang W, Witharana C, Liljedahl A, Kanevskiy M. 2018. Deep convolutional neural networks for automated characterization of Arctic ice-wedge polygons in very high spatial resolution aerial imagery. *Remote Sensing* **10**: 1487.

Zona D, Lipson DA, Zulueta RC, Oberbauer SF, Oechel WC. 2011. Microtopographic controls on ecosystem functioning in the Arctic Coastal Plain. *Journal of Geophysical Research* **116**: G001241.

Vita

Chuck Abolt was born in Dallas, TX in 1989. He graduated from Duke University in 2011 with a bachelor's degree in Spanish, with minors in English and biology. While at Duke he helped found a beekeeping club and spent a year living on an organic farm. In 2013 he enrolled at The University of Texas at Austin to pursue graduate studies in geological sciences, focusing on soil science and hydrology. In 2015 he earned an M.S. and enrolled in the Ph.D. program.

Permanent email: chuck.abolt@gmail.com.

This dissertation was typed by the author.